ENGINEERING NOVEL NANOMATERIALS FROM ULTRASMALL GOLD CLUSTERS FOR USE IN CANCER THERAPY

Elizabeth Higbee-Dempsey

A DISSERTATION

in

Biochemistry and Molecular Biophysics

Presented to the Faculties of the University of Pennsylvania

in

Partial Fulfillment of the Requirements for the

Degree of Doctor of Philosophy

2019

Supervisor of Dissertation	Graduate Group Chairperson
_____	_____
Andrew Tsourkas, Ph.D.	Kim Sharp, Ph.D.
Professor of Bioengingeering	Professor of Biochemistry and Biophysics

Dissertation Committee

Sergei Vinogradov, Ph.D., Professor of Biochemistry and Biophysics

David Chenoweth, Ph.D., Associate Professor of Chemistry

David Cormode, Ph.D., Associate Professor of Radiology

Zhiliang Cheng, Ph.D., Research Associate Professor of Bioengineering

ABSTRACT

ENGINEERING NOVEL NANOMATERIALS FROM ULTRASMALL GOLD CLUSTERS FOR USE IN CANCER THERAPY

Elizabeth Marie Higbee-Dempsey

Andrew Tsourkas

One of the biggest hurdles in clinical therapy is ensuring that drugs have appropriate pharmacokinetic profiles; they must traffic to sites of interest and accumulate there at relevant concentrations, but must also be eliminated from tissues at a desirable rate. This is especially important in oncology because precise tumor locations may be unknown and therapeutics are often toxic to off-target healthy tissues. Nanoscale drug formulations provide a useful way to modulate and improve the behavior of drugs within biological systems. For example, gold nanoparticles (AuNPs) can be designed with physiochemical properties that allow them to traffic from the bloodstream into tumors. Once there, gold can be utilized for a number of clinical applications in imaging (e.g., photoacoustic, CT) and therapy (e.g., photothermal, radiosensitization). Gold nanoformulations can also provide an excellent platform for delivery of other drugs, thereby allowing targeted multifunctional therapy. However, despite their potential utility, gold particles have been slow to translate into the clinic. One area of concern is the slow biodegradation of gold; AuNPs that are too large for renal excretion (> 5-10 nm) are likely to persist in tissues for months, with unknown long-term health consequences. To address this issue, we have developed novel nanomaterials comprising ultrasmall gold particles (~2-3 nm) that are incorporated within a larger micelle structure (~50-200 nm). The large overall size promotes localization into tumors; however, the use of small individual AuNPs improves long-term excretion. In this work, we first present a polymeric micelle containing ultrasmall AuNPs with a pH-sensitive coating. These nanoassemblies are stable at neutral pH but dissociate in acidic environments (pH 5.0); they demonstrate rapid degradation within cellular lysosomes, which

contribute to their progressive and substantial *in vivo* bioelimination. Next, we describe a multifunctional nanocluster combining ultrasmall AuNPs with a near-infrared dye, indocyanine green, without the need for additional complexing reagents. In an aggressive mouse breast cancer model, intravenously-injected clusters could accumulate within tumors and enable photoacoustic imaging and photothermal ablation, ultimately resulting in significantly improved animal survival. Together, these novel clusters present exciting and useful tools for cancer imaging and therapy.

TABLE OF CONTENTS

LIST OF TABLES

LIST OF ILLUSTRATIONS

CHAPTER 1: INTRODUCTION TO GOLD NANOPARTICLES IN BIOLOGICAL SYSTEMS

1.1 Overview of nanoparticles

Introduction to nanomaterials

Nanoparticles are discrete units of matter that behave as a single entity ("particles") and possess dimensions in the scale of 1 to 1000 nm ("nano"). Nanoparticles demonstrate unique attributes as a material. Like molecules, their small size confers high mobility and high specific surface area[1]; however, like bulk materials, they can possess useful ensemble features[2] including mechanical,[3] magnetic[4], optical,[5] electric, and thermal properties. As a result, nanomaterials have been increasingly explored in both the physical and life sciences. In biological systems, they show great promise for the diagnosis, treatment, and prevention of disease.

Nanomaterials can be broadly classified by a number of intersecting categories, the most common of which are based on component materials (organic vs. inorganic, biologically-derived material vs. synthetic). Other important distinctions include shape (spherical vs. nonspherical); preparation route (chemical vs. physical/mechanical vs. biological, bottom-up vs. top-down); and a range of morphological features (size, structure) and functional applications.[6–8]

Gold nanoparticles

Gold nanoparticles (AuNPs) are among the oldest-known and best-studied nanoformulations.[9] Gold is a highly useful material with unique physiochemical properties: high atomic number, surface plasmon resonance, redox behavior,

conductivity, optoelectronic properties, etc.[10,11] AuNPs can be synthesized in a wide range of sizes (from smaller than 1 nm to larger than 500 nm), as well as a range of shapes (including spheres, rods, stars, triangles, boxes, shells, and cages), and under mild reaction conditions (typically atmospheric oxygen and moderate temperatures). Gold surfaces can also be easily functionalized with self-assembled monolayers of thiols, due to the favorable bond formed between gold and sulfur.[12–14] By this method, a wide range of thiolate materials have been used to coat AuNP surfaces, including: alkanes, polymers, antibodies and other proteins, and oligonucleotides.[11]

1.2 Gold nanoparticle formulations

Synthesis of gold cores

The classical method of AuNP synthesis was described in 1951 by Turkevich et al.[15] In this method, tetrachloroauric acid is reduced by trisodium citrate in boiling water, yielding gold spheres with hydrophilic citrate-stabilized surfaces. This original protocol produced 15-20 nm gold spheres; a later breakthrough by Frens et al in 1973 determined that the gold-to-citrate ratio could be manipulated in order to generate a range of particle sizes, from 16 to 147 nm.[16] Other refinements have included the use of alternate reducing agents (e.g. ascorbate, UV irradiation) that improve the spherical definition of particles.[17]

In 1994, Brust and Schriffin reported a landmark strategy for producing hydrophobic gold spheres.[18] In a two-phase system, using tetraoctylammonium bromide as a phase transfer reagent, gold salt is reduced by sodium borohydride and coated with alkanethiols. Particles produced by this method have the advantage of ultrasmall size (approximately 1-5 nm), as well as high stability conferred by the ligand

coating; these thiols form a monolayer that strongly associates with the gold surface through Au-S bonds and with neighbor thiols through van der Waals interactions.[13,19]

Many other innovative syntheses have been reported that greatly expand the repertoire of gold nanoparticles. Some examples include: using ammonium surfactants to form gold nanorods, which have unique resonant properties and biological interactions;[20–22] the formation of gold nanoshells, which exhibit tunable optical properties based on their size;[23–25] and the creation of ultrasmall (< 2 nm) gold nanoparticles, including those with known atomic structure and molecule-like properties such as photoluminescence.[26,27]

Conjugation and surface coating

The surface composition of AuNPs can be tailored by using one or several general strategies (**Figure 1.1**).

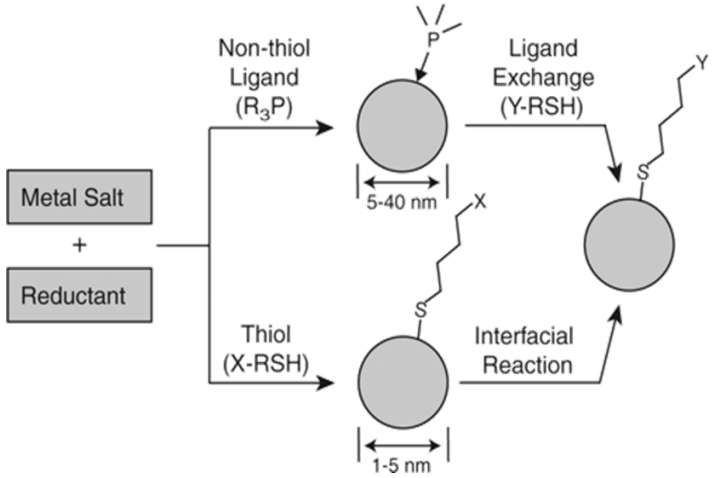

Figure 1.1. Modulation of gold surfaces can follow several different schemes. Adapted by permission from Love et al.[13]

As noted, gold particles complex with surface ligands during their formation; these may be weakly-associated stabilizing agents like citrate, phosphines, and

amines[28–30] or strongly-bound thiols. Many AuNP formulations have been developed with the specific goal of incorporating desired ligands during initial synthesis, often using biologically relevant molecules: glutathione,[31,32] coenzyme A,[33] tiopronin (a pharmaceutical),[33] ethylene glycols,[34–36] and others.[13]

If the desired ligand cannot be directly incorporated, it can sometimes be generated by chemical modification of surface ligands. A very common reaction technique is through peptide coupling.[37–39] Classic organic mechanisms can also be employed, such as alkene metathesis,[40] nucleophilic substitutions,[41] and click chemistry.[42,43]

Alternatively, an existing surface ligand may be displaced by a new ligand. This approach is used to confer long-term stability on citrate AuNPs and other non-thiolated gold particles. Exchange can occur rapidly through simple mixing, though occasionally an intermediary ligand is introduced (e.g., Tween 20, lipoic acid) to minimize potential aggregation of particles).[44,45] Another intermediary ligand, 4-dimethylaminopyridine (DMAP), has been used to transition particles from hydrophobic to hydrophilic in a four-stage process: 1) particles are synthesized by the Brust method in the absence of alkanethiols; 2) the resulting amine-stabilized particles undergo ligand exchange with DMAP; 3) DMAP acquires a positive charge and confers water solubility on the particle; and 4) particles can then undergo additional ligand exchange reactions with hydrophilic thiols in aqueous media.[29] Ligand exchange can also occur on particles that are already coated with thiolates. This exchange occurs by associative substitution – that is, an incoming thiol (or disulfide) displaces a bound thiolate by way of a short-lived intermediate complex, similar to nucleophilic attack reaction/mechanisms.[41,46–48] By equilibrating thiolated particles with an excess of the desired thiol (typically a 10-fold

molar excess), near- to complete-exchange can occur. This method can also be used to decorate particle surfaces with a heterogeneous mix of materials.

Larger assemblies

Gold particles have also been incorporated into a variety of large, complex structures, often involving noncovalent interactions such as electrostatic and protein-substrate (e.g., avidin-biotin).[49,50] One common noncovalent method is to encapsulate hydrophobic AuNPs using amphiphilic materials that thereby confer water solubility without chemical modification. Amphiphilic materials can be natural or synthetic (e.g., lipids, polymers, proteins, small molecules). Based on their properties, and especially their amphiphilic mass ratio, they can form a variety of structures. Common examples of structures include micelles (monolayer of amphiphiles) and vesicles like liposomes and polymersomes (bilayer of amphiphiles). As an advantage, these macrostructures allow the incorporation of multifunctional materials within a single moiety, without the need for complex synthetic conjugation strategies; this has been demonstrated to great effect as a strategy to co-encapsulate therapeutic compounds, allowing delivery of multiple synergistic pharmaceuticals or allowing concomitant imaging and treatment of disease.[51]

1.3 Nanoparticle behavior in biological systems

Introduction to nano-bio interactions

Nanoparticles, including AuNPs, exhibit unique behavior within biological systems. This behavior is often critical to their clinical utility over other materials, and yet it can be difficult to fully understand and control these complex interactions. To achieve their full efficacy, it is often necessary for particles to reach specific tissues, cell types, or

even subcellular compartments, while avoiding off-target locations. There must also be control over dosage and kinetics, as well as considerations of their eventual degradation and/or elimination. Evaluations of nano-bio interactions must include both an accounting of the particle's physiochemical properties – size, shape, composition, etc. – as well as understanding of the biological environments on molecular, cellular, and organismal scales.

1.3.1 Molecular interactions

When nanoparticles enter physiological environments, such as after intravenous injection, they interact with proteins that non-specifically adsorb to their outer surface due to high surface free energy.[52,53] This protein corona forms rapidly[54] and consists of two temporal and spatial phases. Initially, the nanoparticle will be surrounded by a "soft" corona wherein the highest-abundance proteins associate dynamically with the particle surface; after longer exposure, the innermost layer of proteins will be displaced by those with the highest binding affinity, and this "hard" corona may be irreversibly bound to the particle surface.[55,56] It has been proposed that the protein corona is what the cell truly "sees", and therefore studies of the nano-bio interface should consider it as equally or more important than the particle's bare surface composition.[57]

The composition of the protein corona is greatly influenced by the physiochemical makeup of the nanoparticle.[55] Because such a large number of parameters contribute to these interactions, it is often highly difficult to assess their relative contributions; still, some general trends have been reported. For example, a number of studies[58–61] – including several landmark proteomics studies reported by Tenzer et al[54,62] – have demonstrated that protein identity and relative abundance vary with particle size and surface charge. Corona proteins can also undergo conformational

changes, particularly upon association with hydrophobic particles,[63] positively-charged particles,[64] strongly-negatively-charged particles,[65] and rod-shaped particles.[66] Greater quantities of adsorbed proteins (i.e., thicker coronas) have been seen on larger particles[60], hydrophobic particles[67], particles with rough surfaces,[68] and on rod-shaped particles compared to spheres.[69] Biological contributions are also highly important, even within a single medium such as serum. For example, the identities of adsorbed corona proteins can change based on serum concentrations (such as those used for typical *in vitro* experiments vs. *in vivo*),[70] and differences very likely occur between species, disease states, and individuals. Furthermore, variations in the protein corona are likely to have a direct impact on interactions between nanoparticles and cells, including pharmacokinetics, toxicity, and cell selectivity.[54]

1.3.2 Cellular interactions

Particle properties greatly affect interactions with cells, both through coronal variations and more generally. For example, positively charged nanoparticles tend to have faster cellular uptake and higher cytotoxic potential, even after complexing with serum proteins.[65] The enormous impact of surface charge typically arises from the interaction between particles and the phospholipid head groups and protein domains found on the cell membrane; generally, positive nanoparticles have greater associations with the largely negative lipids found on the cell surface, though the impact of this on cell uptake varies between cell lines.[71] Other cell surface elements can contribute to this interplay, including glycans (which may act as a barrier) and specific membrane proteins.

Endocytosis

Nanoparticles typically enter cells through endocytosis.[72–74] In this process, extracellular material is enveloped by cellular membrane; these cavities then pinch off from the outer plasma membrane to form intracellular vesicles that are broadly known as endosomes (**Figure 1.2**). Endosomes transport material throughout the cell and into other specialized vesicular compartments, including other endosomes. A range of different types of endosomes are defined by their unique protein markers and distinct functions. A common target for nanoparticles and other materials is the so-called early endosome.[72,73]

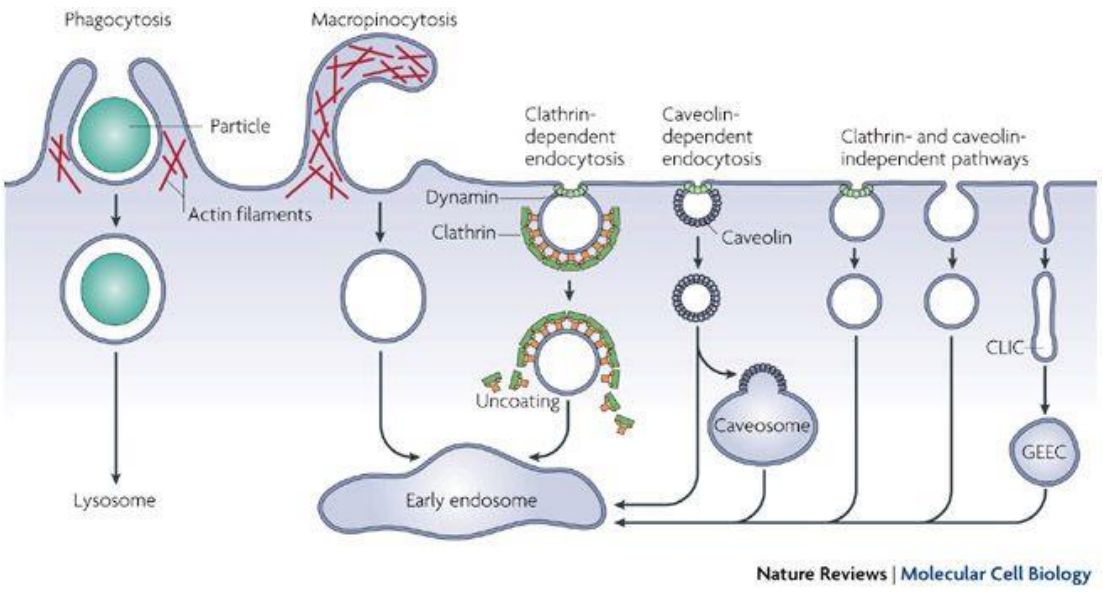

Figure 1.2. Mechanisms of endocytosis and intracellular vesicle trafficking. Reproduced by permission from Springer Nature Customer Service Centre GmbH: Springer Nature, Nature Reviews Molecular Cell Biology, Mayor and Pagano, 2007.[75]

Phagocytosis

Phagocytosis, or cellular “eating”, is typically performed by specialized cell types, termed professional phagocytes, which include macrophages, neutrophils, monocytes, dendritic cells, and mast cells. These cells are responsible for engulfing large cargo

(e.g., pathogenic organisms, cellular debris, and aged cells), performing a critical role in immunity and tissue homeostasis. Phagocytosis can also be performed "nonprofessionally" by several other cell types, including fibroblasts, epithelial cells, and endothelial cells. Their phagocytic functions tend to be more restricted, such as in time (e.g., during development) or by target (e.g., apoptotic bodies only).[76–78]

Cargo is tagged for phagocytosis through affiliation with phagocyte surface receptors. This molecular recognition may occur either by direct recognition of cargo features or through intermediary proteins bound to cargo surface. These latter proteins, known as collectively as opsonins, include proteins from adaptive immunity (immunoglobulins) and innate immunity (complement proteins) as well as other circulating proteins.[79,80] Binding of cargo to the phagocyte surface triggers activation of cytoskeletal actin and extension of cellular pseudopodia, which envelop particles and form phagosomes.[78]

Pinocytosis

Many other forms of endocytic uptake can be classified as pinocytosis, or cellular "drinking". Unlike phagocytosis, these processes are performed by many eukaryotic cell types. In the process known as macropinocytosis,[81,82] actin-driven pseudopodia extend outward from the cell and then fold back towards the cell surface, engulfing pockets of extracellular fluids and their contents. Adsorptive pinocytosis, sometimes called fluid-phase endocytosis, involves the uptake of molecules that interact with the membrane through nonspecific hydrophobic and/or electrostatic interactions. After internalization of these vesicles, intracellular trafficking tends to be relatively slow compared to higher-affinity, receptor mediated endocytosis.[83]

Specific macromolecular cargo can be recognized by specialized cell surface receptors and internalized through receptor-mediated endocytosis. One such pathway uses proteins called clathrins that line the interior of the plasma membrane in localized receptor-rich regions and induce inward curvature.[84] In mammalian cells, clathrin endocytosis is responsible for the uptake of key moieties including cholesterol (via low-density lipoprotein)[85] and transferrin.[86] Although clathrin endocytosis is the canonical pathway of receptor-mediated uptake, clathrin has also been implicated in fluid phase endocytosis.

Another common receptor-mediated pathway involves membrane invaginations called caveolae; these are formed from associations of caveolin and cavin proteins with highly hydrophobic, cholesterol-enriched membrane domains.[87,88] After membrane scission, budded caveolae may fuse with early endosomes or with specialized compartments called caveosomes;[89] these vesicles are distinct from early endosomes in that they are pH neutral and they can bypass the early endosome's downstream cargo degradation pathways.[90] Caveolae have also been implicated in transcytotic trafficking across polarized cells including vascular endothelial cells,[91,92] though other data is mixed.[93,94] Both clathrin- and caveolae-mediated endocytosis canonically utilize the GTPase dynamin for scission of vesicles from the plasma membrane[95–97].

Several other receptor-mediated pathways have been reported that utilize neither clathrin nor caveolae. Though characterization of their mechanisms and specificity is underdeveloped, several of these pathways are identified by their association with particular small GTPases.[75,98] The RhoA-regulated pathway, which also employs dynamin for scission, has been implicated in the uptake of interleukin-2 and several other cytokines. The Cdc42-regulated and ARF6-regulated pathways differ from the

other receptor-mediated pathways described in that they do not use dynamin, and they traffic to distinct types of endosomes – GPI-AP-enriched early endosomal compartments (GEECs)[99,100] or tubular recycling endosomes,[101,102] respectively.

Nanoparticle internalization

All of the described endocytic mechanisms have been associated with nanoparticle uptake, though certain forms predominate. As with the formation of the protein corona, cellular interactions with nanoparticles can vary greatly depending on nanoparticle form and composition. Indeed, the protein corona itself can strongly mediate these interactions, since a number of endocytic mechanisms involve binding specific proteins (e.g., immunoglobulins for phagocytosis, albumin for receptor-mediated endocytosis). Multiple contributions may also be difficult to deconvolute, and can even seem contradictory; for example, large elongated particles may have stronger membrane interactions through higher binding valency, but also require more membrane deformation for internalization.[103] Variations that seem minor can have a large impact; for example, one study found that increasing particle diameter from 100 nm to 200 nm could switch uptake from clathrin- to caveole-mediated mechanisms.[104]

A commonly discussed phenomenon is the discrepancy of nanoparticle size with receptor-mediated endocytosis. A single flask-shaped caveolae has a diameter of 60-80 nm, and the typical size of a clathrin-coated pit is 60-120 nm.[84,90] However, a number of studies have demonstrated strong evidence for these pathways' involvement in uptake of very large nanoparticles. Notably, several bacterial strains appear to use these pathways, despite their micrometer size.[105]

Nanoparticles may be directed towards a specific cell type or cell internalization mechanism through active targeting. For example, placement of folate on particle surfaces has been used to accumulate nanomaterials in cancer cells overexpressing folate receptor, and encourage particle internalization through caveolae.[106,107] Abraxane®, one of the earliest-approved and most successful nanomaterials, contains albumin that is designed to promote transcytosis across the vascular wall via caveolae-mediated mechanisms.[108,109]

Endosomal trafficking

As mentioned, the destination for many pinocytic vesicles is early endosomes, where the engulfed material is separated and sorted.[72,73] For example, membrane receptors can be dissociated from their bound cargo due to the endosome's acidic internal environment (pH 6.0 to 6.2), which is maintained by resident V-ATPase proton pumps.[110,111] The majority of membrane proteins are recycled back to the outer membrane. Material destined for degradation is then packaged into trafficking vesicles, transported along microtubules towards the cell center, and fused with late endosomes. Late endosomes are more acidic (pH 5.5 to 6.0) and contain hydrolytic enzymes; these vesicles fuse with and mature into lysosomes, which have increased acidity (pH 4.5 to 5.0) and a large cohort of lytic enzymes.[112]

Phagosomes undergo a similar maturation process involving progressive acidification and changes in enzymatic content.[78,113] Phagosomes have fusion events with early endosomes, transitioning into late phagosomes while moving along microtubules towards the cell center. Finally, late phagosomes fuse with lysosomes to form phagolysosomes.[113] Phagolysosome composition can vary significantly between different phagocyte types. For example, they are highly acidic (as low as pH 4.5) in M2

macrophages, which are primarily responsible for clearing apoptotic and necrotic material. However, phagocytes involved with elimination of pathogens, such as M1 macrophages and neutrophils, undergo a slower rate and/or lower extent of acidification; this has been attributed to a number of mechanisms[114,115] including delayed fusion with lysosomes, fewer copies of V-ATPase, leakage of protons through increased phagosome membrane permeability, and consumption of protons by superoxide. In these cells, reduced lysosomal acidity is associated with greater production of reactive oxygen species (through the activity of NADPH oxidase) and highly effective antimicrobial activity.[113,115]

Notably, some endocytic vesicles (e.g., caveosomes) – can bypass these pathways; this phenomenon is exploited by a number of pathogens,[89,90,105,116,117] and could be used as a mechanism for delivering therapeutics while avoiding their lysosomal degradation.[109,118]

Cytosolic entry

For many important therapeutic targets, nanoparticles (and other drugs) must reach the cytoplasm. The advantages of this include: delivery of cytosolically active agents, such as proteins and nucleic acids; ability to interact with native cytosolic structures, such as organelles; and avoidance of negative endosomal/lysosomal effects, including quenching of imaging agents[119–121] and degradation of materials. In order to access the cytosol, particles have been designed to traverse the lipid membrane using several strategies.

Particles that are very small (1-4 nm) – or, very small in at least one dimension – may be capable of directly penetrating the plasma membrane.[122,123] To deliver larger

particles, a common strategy is coating particle surfaces with cell penetrating peptides; as their name suggests, these short (5-30 amino acids) and typically net-cationic peptides are capable of passing through cell membranes, often without overt membrane disruption.[124–126] This method has been used to deliver gold nanoparticles[127] and a variety of other nanomaterials like iron oxide nanoparticles,[128] liposomes,[129–132] and polyplexes.[133] Particle surfaces can also be designed to mimic physiochemical features of cell penetrating peptides, such as an ordered arrangement of hydrophobic and ionic groups.[134]

Other techniques for cytosolic delivery involve escape from intracellular endosomes. One such strategy, dubbed the "proton sponge" method,[135–137] involves loading endosomes with nanomaterials that possess high proton buffering capacity (usually titratable polyamines). As these materials sequester endosomal protons, they can swell due to intramolecular electrostatic repulsion; at the same time, the continued activity of V-ATPase pumps will result in progressive accumulation of 1) chloride ions, which passively influx to balance transmembrane voltage, and 2) water, due to the resulting osmotic pressure. These two forces cause endosomes to rupture, allowing leakage of nanoparticle cargo into the cytosol.[136,138] Another endosomal escape strategy employs a different class of peptides known as membrane-destabilizing peptides or endosome-disrupting peptides. These peptides, many of which are derived from viral proteins, trigger membrane disruption in response to endosomal environmental cues such as low pH,[139,137] allowing escape of associated nanoparticles and other cargo.[140,141] Importantly, methods of cytosolic entry may result in cytotoxicity due to disruption of the outer membrane (hole formation and/or membrane thinning).[142]

1.3.3 Organismal interactions

The majority of nanomedicines are designed to be injected as a bolus into peripheral veins.[143] Their initial interactions within the bloodstream will therefore include the vascular endothelial cells that line vessel walls, but will also include circulating cells (erythrocytes, leukocytes, and platelets) and circulating proteins (albumin, globulins, fibrinogens, and regulatory proteins).[60,144,145] Particles may also be marginated to different areas of the vessel cross section (i.e., towards the outer walls) due to fluid tumbling dynamics and interactions with other circulating materials.[146] As particles are carried to the heart, they will first encounter capillary beds within the lungs; this may cause very large particles to become deposited there. Other/smaller particles will enter the arterial system and move into organs (**Figure 1.3**).

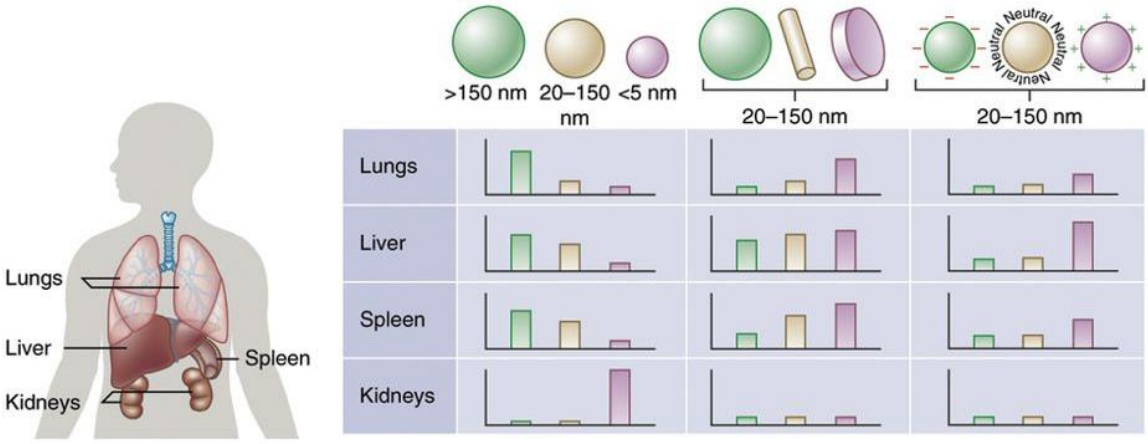

Figure 1.3. Potential trends in nanoparticle distribution based on size, shape, and surface charge. Reproduced by permission from Springer Nature Customer Service Centre GmbH: Springer Nature, Nature Biotechnology, Blanco et al, 2015.[147]

Healthy vasculature

Much of the body's vasculature consists of continuous endothelium, with nonfenestrated endothelial cells connected via tight junctions and adherens junctions.[148]

Due to their size, most nanomaterials are unable to pass between these cells, so can only exit these vessels and enter tissues by endocytic uptake through cells, i.e. transcytosis. However, within some tissues, endothelial cells contain small constitutive holes called fenestrae.[148] In organs such as the kidney, these openings (approximately 60-80 nm) are effectively narrowed to 5-6 nm by filamentous diaphragms; by contrast, the liver and spleen contain larger sinusoidal gaps (approximately 100-250 nm), no diaphragms, and a discontinuous basement membrane.[144,148,149] As blood passes through these vessels, nanoparticles can leak out of pores and accumulate within these organs in a matter of minutes, being effectively filtered by size.[143,147]

Organs compartments

Once particles leave fenestrated vessels and enter an organ, they must perfuse through the extracellular microenvironment and its assortment of matrix proteins and glycans (e.g., laminin, collagen) which have the potential to impede diffusion of nanoparticles.[146,150,151] In the liver and spleen, particles will encounter large populations of resident tissue macrophages that comprise the mononuclear phagocyte system (MPS, formerly known as the reticuloendothelial system, RES).[152,153] These tissue macrophages are often the dominant consumers of intravenously-administered nanoparticles.

Spleen

The spleen plays a major role in filtration and elimination of pathogenic organisms and aged erythrocytes; nanomaterials can be similarly scavenged due to shared characteristics (i.e., nano size, opsonization, and low deformability).[146,154,155] Studies in rodents have found that smaller nanoparticles (15-200 nm) tend to be taken up by a subset of macrophages found in the spleen's marginal zone (the junction

between red and white pulps),[156,157] while larger particles end up in red pulp macrophages.[158] Notably, human spleens have different architecture (e.g., no marginal zone and different macrophage subtypes), so studies performed in rodents and other animals may not accurately reflect nanoparticle behavior in humans.[159,160]

Liver

Like the spleen, the liver sequesters pathogens and aged red blood cells; it also has a special role in elimination of large lipoprotein particles (> 200 nm) called chylomicrons.[144,148,161] The liver's resident macrophages, termed Kupffer cells, form the body's largest reservoir of tissue macrophages (often reported as 50-80%).[162,163] These cells commonly internalize large fractions of nanoparticles, particularly opsonized particles. Notably, particles can also be taken up by hepatic sinusoidal epithelial cells, which tend to have high endocytic activity; it has been proposed that these are a major source of receptor-mediated endocytosis.[148,164,152]

Kidney

In the kidney, blood passes through renal filtration structures called glomeruli (which exclude material larger than 5-6 nm) and flows into tubules; fluid and metabolites are then re-collected by renal veins, while remaining waste material flows through the ureter into the bladder.[165] The kidney thereby collects nanomaterials that are smaller than 5-6 nm (including high-aspect-ratio particles with two small dimensions). Notably, small particles must also have low opsonization, or else they will likely be diverted by the MPS.[146,165–167]

Diseased vasculature

While vascular leakage is fundamental for the healthy filtration functions of the mentioned organs, leaky endothelial beds can also arise in several diseased states. For example, inflammation increases vessel permeability, which facilitates migration of immune cells from blood into diseased tissue[168] and can also be exploited to deliver nanotherapeutics.[169]

Abnormal vascular fenestrations are also famously associated with cancer. As tumors grow beyond 2-3 mm in diameter and surpass limits for nutrient diffusion, they must establish an independent blood supply.[168,170,171] However, this angiogenic process is highly dysregulated, and the resulting vessels are often characterized by tortuous branching, uneven dilation, abnormal deposition of mural cells and basement membranes, and gaps between endothelial cells (most 1-100 nm, up to almost 5 µm).[172–175] Through these gaps, circulating nanomaterials can extravasate from the bloodstream and into tumor tissue.[151] Furthermore, the intratumor environment typically lacks functional lymphatic vessels,[176] so particles may not be able to drain away from tissues quickly. These two phenomena are known collectively as the enhanced permeability and retention (EPR) effect,[177] and are the theoretical basis for the observation that long-circulating nanomaterials can accumulate in tumor tissue on the basis of size alone. The majority of FDA-approved nanoparticles for oncology have been designed based on this principle, without molecular targeting.

However, several challenges are associated with this strategy. It can be difficult for particles to permeate far away from blood vessels – indeed, the lack of lymph drainage within the tumor also causes high interstitial pressure that may prevent inward diffusion of particles[178,179] This is especially important considering many tumors may have large sections that are poorly vascularized, and some cancer types (e.g., prostate)

are prone to low vascular density overall.[179,180] Also, while particle accumulation may be higher than that of small molecular compounds, the overall dose fraction delivered to the tumor is often still quite low. In a landmark meta-analysis performed by Wilhelm et al,[181] it was found that tumors received a median of only 0.7% of the injected dose. Also, though EPR has been observed consistently in animal models, these may not accurately reflect the typical clinical presentation, especially when xenograft models are used for establishing tumors. In humans, the extent of EPR may be highly variable between different tumor types, in different patients, in metastases, and even within a single tumor.[182] Nevertheless, EPR can be an effective tool for delivery of nanomaterials.

1.3.4 Degradation and elimination

By lysosomal pathways, a large portion of ingested material – including nanomaterials – are degraded by the cell.[183] Nanoparticles and their breakdown products can exit the body through renal and/or hepatobiliary excretion pathways.[184] Particles that accumulate in the kidneys and pass through renal filters are then collected in the urine, where they can be eliminated.[165] Within the liver, particles can be endocytosed by hepatocytes; these cells periodically exocytose the contents of their lysosomes into bile, which eventually carries this material into the duodenum and into feces.[185–187] As mentioned, most particles that enter the liver are sequestered in Kupffer cells (at least, preliminarily), and therefore must avoid or escape these cells in order to undergo hepatobiliary excretion. Additionally, while renal clearance generally occurs within minutes, hepatobiliary excretion has a timeline of weeks to months.[186]

Many organic materials are lysosomally digested. For example, dextran can degrade over the course of several weeks, eventually being excreted through the

urine.[188] Degradation of organic materials commonly occurs via lysosomal hydrolytic enzymes, though they can also be degraded by reactive oxygen species; interestingly, this process can take place intracellularly[189,190] or extracellularly.[191,192] Some inorganic materials can be degraded within lysosomes, generally through acidic mechanisms.[193] An excellent example is iron oxide nanoparticles; in vivo studies have demonstrated their breakdown in lysosomes and incorporation into the body's iron store – first in intracellular ferritin, eventually in RBC hemoglobin – potentially without disrupting cellular iron homeostasis.[188,194–196]

However, gold nanoparticles present a great challenge for biodegradation. They have very limited breakdown within the body, and numerous studies have shown persistence of gold for long timeframes in organs such as the liver.[197–200] It does appear that some gold nanoparticle formulations can break down over time.[194] One proposed mechanism is through etching by hydroxyl radicals, which can be produced by macrophages;[201–203] it may also be possible for surface-bound thiols to dissociate from gold cores and pull out individual Au atoms as they migrate.[204,205] Occasionally, the robustness of gold has been utilized purposefully, such as to protect other nanomaterials from degradation.[206] However, it is generally considered a hurdle for clinical translation.[207,208]

1.3.5 Other physiochemical interactions

Stimulus-responsive nanoparticles

The complexity of biological systems presents unique challenges in that materials must often navigate multiple compartments over time; a particle's physiochemical properties may be advantageous at one stage and unfavorable in another. To address this issue, a number of reported nanoformulations have been

designed to respond to environmental changes in order to produce different spatiotemporal effects.

One source of useful triggers is the cohort of different physiochemical conditions present within the body. For example, pH gradients exist between many tissues and subcellular compartments. As previously mentioned, cellular endosomes and lysosomes are typically acidic; solid tumors may also have reduced extracellular pH (as low as 6.5) due to hypoxia, lactate production, and related effects.[209,210] Nanomaterials may respond to these conditions through changes such as protonation or hydrolysis.[211,212] Some examples of triggered effects include, but are not limited to: electrostatic swelling or membrane fusion to rupture endosomes,[138,213] cleavage to release covalently-bound drug cargo or expose surface ligands,[214,215] solubility transitions that allow dispersion of cargo and/or particle degradation;[216,217] and aggregation or dissociation for tumor retention or penetration, respectively.[218] In addition to pH-triggered events, many other endogenous stimuli can be targeted to induce similar changes in particles. Within tumors, stimuli could potentially include enzymes (especially proteolysis),[219–222] redox changes (especially disulfide reduction),[223–225] and temperature (hyperthermia).[226]

Particles have also been designed to react to exogenously-applied triggers. These often have the advantage of additional control over the site, time, and intensity of administration. For example, rather than relying on the minor hyperthermia present in some diseased tissue, temperature can be directly increased through mechanisms such as highly-focused ultrasound.[227,228] Nanomaterials themselves may generate heat in response to triggers like irradiation and ultrasound,[229–235] which can be used for applications such as therapeutic tissue ablation or enhanced release of other cargo.

Toxicity

As described in detail, nanomaterials interact uniquely with biological systems in ways that are distinct from their composite materials' molecular or bulk properties. This principle applies to toxicity as well. Materials can have distinctive safety profiles based on factors that include their physical presentation within a particle structure, their combination with other incorporated substances, or their particle-related degradation profiles. A number of studies have looked at the toxicity of gold nanoparticles, but it is clear that results can vary widely.[200,236–238] General mechanisms of toxicity include oxidative stress,[65,239,240] cytoskeletal changes,[65,239,240] upregulation of proinflammatory cytokines,[241,242] and membrane lysis.[239] Toxicity can also be associated with persistence of AuNPs within lysosomes; their presence may cause alkalization and inhibition of lytic enzymes within lysosomes, and can disrupt autophagosome-lysosome fusion.[243,244]

Unsurprisingly, toxicity appears to depend greatly on the surface coating of particles. Several early studies demonstrating toxicity in gold particles – especially nanorods – were ultimately found to be the result of surface-associated cetyltrimethylammonium (CTAB), which is commonly used in particle synthesis and which can cause mitochondrial damage and apoptosis.[245,246] In animal studies, citrate-coated particles were found to be more biocompatible than particles coated with a common solubilizing peptide, CALNN, which produced anemia and atrophy of the spleen.[199] Notably, surface composition has a large impact on protein corona and on membrane interactions, both of which can contribute to the apparent toxicity of particles. For example, studies showed greater dose-dependent toxicity for cationic particles than for anionic particles, but this may have been the effect of their greater cellular

association and/or uptake.[65,239] An interesting study by Soenen et al[240] also reported that positively-charged particles could induce toxicity, while neutral PEG-coated particles were less toxic; however, when data was normalized by intracellular nanoparticle levels, PEGylated particles were found to have greater induction of ROS. Another property that modulates toxicity is particle size, though these trends are especially variable between studies; particles have been separately described as toxic only in the range of 8-37 nm;[247] only in the range of 1.2-1.4 nm;[248] or only below 6 nm.[241]

However, a large number of studies have found AuNPs to be generally nontoxic.[59,237,249–251] Mouse studies using AuroVist™ (1.9-nm water-soluble AuNPs) have reported an LD_{50} as high as 3.2 g kg^{-1} body weight.[252] Other studies have shown excellent tolerance for chronic high doses of AuNPs (up to 550 μg kg^{-1} per day for up to 28 days).[253,254] One of the most comprehensive studies was performed by Gad et al,[198] who tested PEGylated 155-nm gold shells (AuroLase®) and showed no acute or chronic toxicity in mice or dogs. These data formed the basis for clinical trials involving photothermal ablation of prostate tumors, and the particles' clinical safety in patients was confirmed.[255,256] Overall, it is clear that many AuNPs can exhibit excellent biocompatibility, though new formulations must be rigorously tested.

1.4 Applications for gold nanoparticles in cancer

Cancer

Cancer, which is characterized as the malignant uncontrolled growth of cells, remains one of the world's leading causes of death. Treatment paradigms typically include surgery to remove solid tumors, as well as a combination of chemotherapy and radiation to induce cellular death. All three of these areas have been explored heavily in nanoparticle applications, including image-guided surgery to reveal tumor location and

define margins; delivery of toxic compounds to tumors; and localized radiation dose enhancement.[257,258]

Breast cancer is the most common type of cancer in women, with 1.4 million new cases diagnosed annually worldwide.[259] While the incidence of breast cancer has been steadily increasing globally, it has decreased over the last decade in the United States. This decrease correlates with the introduction of hormone-replacement therapy, which has proven effective in treating estrogen receptor-positive tumors. However, nearly 10-20% of tumors lack the ability to respond to hormone therapy.[260] These tumors tend to be more aggressive, consequently requiring more aggressive regimens of cytotoxic chemotherapy, surgery (where possible), and radiation.[261] The use of targeted nanomedicines could potentially facilitate enhanced treatment of breast cancer without increasing adverse side effects.[262,263]

1.4.1 Imaging applications

Computed tomography

Computed tomography, or CT, is a highly efficient and widely available tool for imaging tumors and other biological tissues.[264] CT imaging involves the three-dimensional reconstruction of images produced by x-rays. Tissues attenuate x-rays to different degrees based on several factors including thickness and mass attenuation coefficient; this value is derived from the photoelectric effect, which proportional to the cube of the material's atomic number (Z^3). Many soft tissues are difficult to differentiate due to their similar degrees of x-ray attenuation, but they can be distinguished by administering contrast agents with variable distribution. Gold nanoparticles have excellent potential as a CT contrast agent due to gold's high atomic number (79) and AuNPs' distinct pharmacokinetics.[238,264,265] Early uses of AuNPs in x-ray imaging were

reported in 2004 and 2006 by Hainfeld et al.[266,252] These studies using 1.9-nm AuNPs produced detailed images of blood vessels (including vascularized tumors), with greater and longer-lived sensitivity compared to the standard-of-care iodine-based contrast agent. Many other AuNP formulations have since demonstrated good tumor accumulation and contrast,[265] including those with[267–270] and without[271,272] molecular targeting. These highly-effective contrast agents could ultimately improve patient safety by allowing lower x-ray radiation doses.

Photoacoustic imaging

In photoacoustic imaging, or PA, a material is irradiated with pulsed light and the absorbed energy is dissipated nonradiatively as heat. While the laser is applied (i.e., "during" the pulses), local temperatures increase and the material undergoes thermoelastic expansion. Between pulses, the temperature drops and the material contracts. These repeated pressure changes generate acoustic waves, which can be detected as wideband ultrasonic emissions and eventually reconstructed into an image of this region.[273,274] This imaging modality is commonly used to image endogenous photoabsorbers, which can be distinguished based on their spectral signals; for example, oxygenated and deoxygenated hemoglobin may be distinctly identified within tissues for comparisons of relative concentration.

Many gold particles can be excellent PA contrast agents due to their strong absorbance of light, though this absorbance depends strongly on particle size and shape.[274,275] When imaging tissues, it is highly desirable to use contrast agents that absorb in the near-infrared (NIR) range (approximately 650-110 nm); light in this window has relatively low tissue absorption and therefore deeper penetration, which allows deeper imaging.[276] This makes PA imaging one of the best and only ways to visualize

deep tissues in real time. Furthermore, it does not require use of ionizing radiation, and its instrumentation is becoming progressively cheaper and more accessible.[277,278] These factors are likely to contribute to its increasing adoption in clinical settings.

Photoluminescence and quenching

Gold nanoparticles can exhibit a property known as surface plasmon resonance (SPR).[11,279,280] A particle's electron cloud (i.e., conduction electrons) can collectively oscillate when excited at a specific frequency of light, resulting in strong absorbance at that wavelength. This SPR absorbance peak is determined by the particle's size, shape, and other properties; for example, it does not occur at all in very small nanoparticles (< 2 nm). In general, when gold particles aggregate (or otherwise closely associate), their absorbance spectrum will shift to reflect the SPR peak associated with the diameter of the larger composite; this has been utilized as a mechanism to detect local changes.[281–283,280]

Gold is capable of strongly quenching the fluorescence of nearby materials.[284,285] This phenomenon can also be utilized as a reporter of molecular conditions. For example, fluorophores can be conjugated onto AuNP surfaces using environmentally-sensitive linkers; the dyes' signals are quenched while bound to AuNPs, but they will emit detectably when they are cleaved from gold.[286–288] When it is desirable to reduce the quenching effects of gold within particles, materials like silica can be installed as a buffer.[289,290] However, gold's quenching ability may also improve its utility in various applications, particularly those that rely on the nonradiative emission of absorbed energy (e.g., photoacoustic imaging and photothermal therapy).

1.4.2 Therapeutic applications

Radiation therapy

Radiation therapy is one of the primary clinical paradigms for cancer treatment, indicated in approximately 50% of all cancer patients.[291] In this process, ionizing radiation deposits energy into biological tissues and causes oxidation and fragmentation of DNA, proteins, and membranes. This can occur directly when macromolecules absorb the applied radiation, but most damage (~70%) derives from their secondary reactions with ionized water or oxygen, i.e. reactive oxygen species.[292,293] DNA damage, especially in the form of double-strand breaks, are difficult for cells to repair and often result in cell cycle arrests and cell death. However, incorrectly repaired DNA lesions might introduce new mutations, making it especially important that radiotherapy delivers effective killing doses to malignant cells while avoiding delivery to healthy tissues.[293]

Radiation is typically applied as convergent beams of photons (gamma or x-rays). Another option, ion beam radiotherapy (e.g., protons), has gained increasing clinical prevalence due to its greater spatial precision; as ions pass through tissue, most of their energy is attenuated and deposited at a specific terminal distance termed the Bragg peak, which can be focused to the tumor's position.[293,294] Nevertheless, both photon and ion therapies risk significant exposure of healthy tissue, particularly along beam paths.

Tumor specificity can be improved by applying radiosensitizers, which increase local energy deposition and/or vulnerability to damage.[295] Gold nanoparticles function as potent radiosensitizers through a number of mechanisms. As mentioned previously, gold's high atomic number is associated with strong x-ray attenuation. Upon photon

absorption, gold can eject secondary electrons, including A) inner-shell photoelectrons, with accompanying Auger electrons, at lower (keV) photon energies; and B) outer-shell Compton electrons at higher (MeV) photon energies (**Figure 1.4**).[295,296] Notably, kilovoltage energies provide the greatest dose enhancement effect for gold over tissue, though megavoltage provides deeper tissue penetration and is the current clinical standard.[297] AuNPs can also absorb energy through intermediary water- and oxygen-derived radicals, and this mechanism likely contributes strongly to the radiosensitization effects observed in higher-energy photon therapy and in proton radiotherapy.[293,297] In addition to emitting electrons, irradiated gold nanoparticles may increase generation of reactive oxygen species through catalytic reactions.[295] Finally, AuNPs help confine the dose delivery area by increasing radiation attenuation within the tumor environment, reducing the fraction delivered to healthy tissues beyond and thereby improving safety margins.[293,296,298]

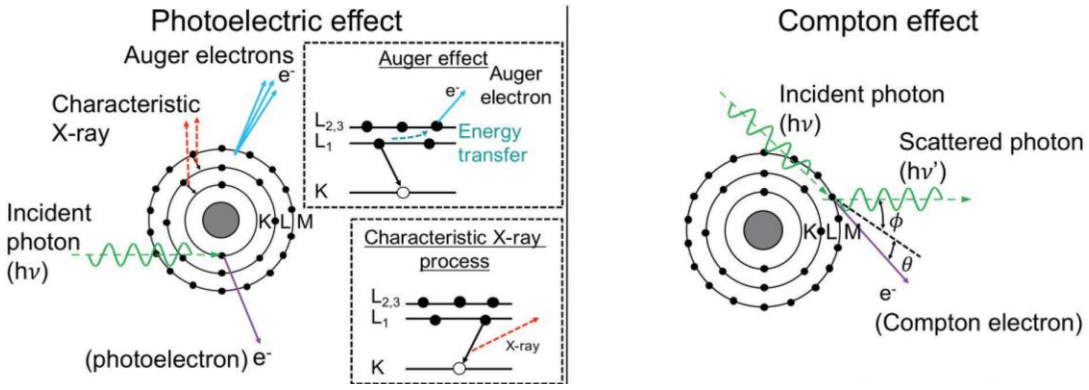

Figure 1.4. Mechanisms of photon attenuation and secondary emission by radiosensitizers. Adapted by permission from Laprise-Pelletier et al.[296]

Thermal therapy

Hyperthermia is useful in several therapeutic applications, particularly in cancer, where localized heat can generate cellular damage and allow partial or complete tissue ablation.[299,300] Cell death typically occurs at temperatures beyond 41-45 °C, through either apoptosis (mild heat) or necrosis (higher heat); high temperatures are typically pursued in bulk tissues to ensure sufficient temperature over spatial gradients.[300] Hyperthermia can also enhance the effectiveness of other therapeutic mechanisms. For example, thermal stress induces protein damage that renders cells more susceptible to damage from radiotherapy and chemotherapy; hyperthermia can also increase tumor blood flow and thereby increase delivery of chemotherapeutic agents and radiosensitizing oxygen.[301–303] Thermal destruction of cancer cells can also generate and disseminate tumor antigens, while local inflammation stimulates immune recruitment and activation, making hyperthermia a potential complement to immunotherapy.[300,304]

Localized deep tissue heating can be induced non-invasively through application of ultrasound or long-wave electromagnetic radiation, which heat tissue directly.[305] However, nanoparticle-mediated heating techniques typically offer greater treatment precision both in uniformity and spatial resolution of tumor heating, thereby reducing damage to off-target tissues.[303,306] As previously described, gold nanoparticles are capable of absorbing optical energy and converting it into heat;[307] photothermal therapy using gold nanoparticles and nanorods have been explored extensively since initial studies in 2003[308] and 2006[230], respectively. Gold nanoparticles can also generate heat by absorbing radiofrequency radiation, though this process is more poorly understood and studied.[306,309]

1.5 References

[1] W. J. Stark, *Angewandte Chemie International Edition* **2011**, *50*, 1242–1258.

[2] B. Zhang, *Physical Fundamentals of Nanomaterials*, Elsevier, **2018**.

[3] D. Guo, G. Xie, J. Luo, *J. Phys. D: Appl. Phys.* **2013**, *47*, 013001.

[4] Q. A. Pankhurst, J. Connolly, S. K. Jones, J. Dobson, *J. Phys. D: Appl. Phys.* **2003**, *36*, R167–R181.

[5] K. L. Kelly, E. Coronado, L. L. Zhao, G. C. Schatz, *J. Phys. Chem. B* **2003**, *107*, 668–677.

[6] I. Khan, K. Saeed, I. Khan, *Arabian Journal of Chemistry* **2017**, DOI 10.1016/j.arabjc.2017.05.011.

[7] S. A. M. Ealia, M. P. Saravanakumar, *IOP Conf. Ser.: Mater. Sci. Eng.* **2017**, *263*, 032019.

[8] C. Kinnear, T. L. Moore, L. Rodriguez-Lorenzo, B. Rothen-Rutishauser, A. Petri-Fink, *Chem. Rev.* **2017**, *117*, 11476–11521.

[9] M. Das, K. H. Shim, S. S. A. An, D. K. Yi, *Toxicol. Environ. Health Sci.* **2011**, *3*, 193–205.

[10] R. Sardar, A. M. Funston, P. Mulvaney, R. W. Murray, *Langmuir* **2009**, *25*, 13840–13851.

[11] Y.-C. Yeh, B. Creran, V. M. Rotello, *Nanoscale* **2012**, *4*, 1871–1880.

[12] C. D. Bain, E. B. Troughton, Y. T. Tao, J. Evall, G. M. Whitesides, R. G. Nuzzo, *J. Am. Chem. Soc.* **1989**, *111*, 321–335.

[13] J. C. Love, L. A. Estroff, J. K. Kriebel, R. G. Nuzzo, G. M. Whitesides, *Chem. Rev.* **2005**, *105*, 1103–1170.

[14] T. Bürgi, *Nanoscale* **2015**, *7*, 15553–15567.

[15] J. Turkevich, P. C. Stevenson, J. Hillier, *Discuss. Faraday Soc.* **1951**, *11*, 55–75.

[16] G. Frens, *Nature Physical Science* **1973**, *241*, 20–22.

[17] J. Kimling, M. Maier, B. Okenve, V. Kotaidis, H. Ballot, A. Plech, *J. Phys. Chem. B* **2006**, *110*, 15700–15707.

[18] M. Brust, M. Walker, D. Bethell, D. J. Schiffrin, R. Whyman, *Journal of the Chemical Society, Chemical Communications* **1994**, *0*, 801–802.

[19] M. J. Hostetler, J. E. Wingate, C.-J. Zhong, J. E. Harris, R. W. Vachet, M. R. Clark, J. D. Londono, S. J. Green, J. J. Stokes, G. D. Wignall, et al., *Langmuir* **1998**, *14*, 17–30.

[20] N. R. Jana, L. Gearheart, C. J. Murphy, *J. Phys. Chem. B* **2001**, *105*, 4065–4067.

[21] B. Nikoobakht, M. A. El-Sayed, *Chem. Mater.* **2003**, *15*, 1957–1962.

[22] Y. Niidome, K. Nishioka, H. Kawasaki, S. Yamada, *Chem. Commun.* **2003**, 2376–2377.

[23] H.-S. Zhou, I. I. Honma, H. Komiyama, J. W. Haus, *Phys Rev B Consens Matter* **1994**, *50*, 12052–12056.

[24] X. Huang, M. A. El-Sayed, *Journal of Advanced Research* **2010**, *1*, 13–28.

[25] Y.-C. Wang, E. Rheaume, F. Lesage, A. Kakkar, *Molecules* **2018**, *23*, 2851.

[26] P. D. Jadzinsky, G. Calero, C. J. Ackerson, D. A. Bushnell, R. D. Kornberg, *Science* **2007**, *318*, 430–433.

[27] L. Shang, S. Dong, G. U. Nienhaus, *Nano Today* **2011**, *6*, 401–418.

[28] W. W. Weare, S. M. Reed, M. G. Warner, J. E. Hutchison, *J. Am. Chem. Soc.* **2000**, *122*, 12890–12891.

[29] D. I. Gittins, F. Caruso, *Angewandte Chemie International Edition* **2001**, *40*, 3001–3004.

[30] P. M. Shem, R. Sardar, J. S. Shumaker-Parry, *Langmuir* **2009**, *25*, 13279–13283.

[31] T. G. Schaaff, G. Knight, M. N. Shafigullin, R. F. Borkman, R. L. Whetten, *J. Phys. Chem. B* **1998**, *102*, 10643–10646.

[32] X. Mao, Z.-P. Li, Z.-Y. Tang, *Front. Mater. Sci.* **2011**, *5*, 322–328.

[33] A. C. Templeton, S. Chen, S. M. Gross, R. W. Murray, *Langmuir* **1999**, *15*, 66–76.

[34] W. P. Wuelfing, S. M. Gross, D. T. Miles, R. W. Murray, *J. Am. Chem. Soc.* **1998**, *120*, 12696–12697.

[35] A. G. Kanaras, F. S. Kamounah, K. Schaumburg, C. J. Kiely, M. Brust, *Chem. Commun.* **2002**, 2294–2295.

[36] E. E. Foos, A. W. Snow, M. E. Twigg, M. G. Ancona, *Chem. Mater.* **2002**, *14*, 2401–2408.

[37] A. C. Templeton, M. J. Hostetler, E. K. Warmoth, S. Chen, C. M. Hartshorn, V. M. Krishnamurthy, M. D. E. Forbes, R. W. Murray, *J. Am. Chem. Soc.* **1998**, *120*, 4845–4849.

[38] J. Fan, S. Chen, Y. Gao, *Colloids and Surfaces B: Biointerfaces* **2003**, *28*, 199–207.

[39] K.-M. Sung, D. W. Mosley, B. R. Peelle, S. Zhang, J. M. Jacobson, *J. Am. Chem. Soc.* **2004**, *126*, 5064–5065.

[40] D. Samanta, N. Faure, F. Rondelez, A. Sarkar, *Chem. Commun.* **2003**, 1186–1187.

[41] A. C. Templeton, M. J. Hostetler, C. T. Kraft, R. W. Murray, *J. Am. Chem. Soc.* **1998**, *120*, 1906–1911.

[42] J. L. Brennan, N. S. Hatzakis, T. R. Tshikhudo, V. Razumas, S. Patkar, J. Vind, A. Svendsen, R. J. M. Nolte, A. E. Rowan, M. Brust, *Bioconjugate Chem.* **2006**, *17*, 1373–1375.

[43] M.-X. Zhang, B.-H. Huang, X.-Y. Sun, D.-W. Pang, *Langmuir* **2010**, *26*, 10171–10176.

[44] K. Aslan, V. H. Pérez-Luna, *Langmuir* **2002**, *18*, 6059–6065.

[45] S.-Y. Lin, Y.-T. Tsai, C.-C. Chen, C.-M. Lin, C. Chen, *J. Phys. Chem. B* **2004**, *108*, 2134–2139.

[46] M. J. Hostetler, A. C. Templeton, R. W. Murray, *Langmuir* **1999**, *15*, 3782–3789.

[47] M. Hasan, D. Bethell, M. Brust, *J. Am. Chem. Soc.* **2002**, *124*, 1132–1133.

[48] R. Hong, J. M. Fernández, H. Nakade, R. Arvizo, T. Emrick, V. M. Rotello, *Chem. Commun.* **2006**, 2347–2349.

[49] M. Zheng, X. Huang, *J. Am. Chem. Soc.* **2004**, *126*, 12047–12054.

[50] X. Jiang, A. Housni, G. Gody, P. Boullanger, M.-T. Charreyre, T. Delair, R. Narain, *Bioconjugate Chem.* **2010**, *21*, 521–530.

[51] S. H. Crayton, A. K. Chen, J. F. Liu, E. M. Higbee-Dempsey, C.-H. Huang, A. Tsourkas, Z. Cheng, in *Comprehensive Biomaterials II* (Ed.: P. Ducheyne), Elsevier, Oxford, **2017**, pp. 424–466.

[52] A. E. Nel, L. Mädler, D. Velegol, T. Xia, E. M. V. Hoek, P. Somasundaran, F. Klaessig, V. Castranova, M. Thompson, *Nature Materials* **2009**, *8*, 543–557.

[53] N. D. Donahue, H. Acar, S. Wilhelm, *Advanced Drug Delivery Reviews* **2019**, DOI 10.1016/j.addr.2019.04.008.

[54] S. Tenzer, D. Docter, J. Kuharev, A. Musyanovych, V. Fetz, R. Hecht, F. Schlenk, D. Fischer, K. Kiouptsi, C. Reinhardt, et al., *Nature Nanotechnology* **2013**, *8*, 772–781.

[55] V. H. Nguyen, B.-J. Lee, *Int J Nanomedicine* **2017**, *12*, 3137–3151.

[56] M. Lundqvist, J. Stigler, T. Cedervall, T. Berggård, M. B. Flanagan, I. Lynch, G. Elia, K. Dawson, *ACS Nano* **2011**, *5*, 7503–7509.

[57] D. Walczyk, F. B. Bombelli, M. P. Monopoli, I. Lynch, K. A. Dawson, *J. Am. Chem. Soc.* **2010**, *132*, 5761–5768.

[58] M. Lundqvist, J. Stigler, G. Elia, I. Lynch, T. Cedervall, K. A. Dawson, *PNAS* **2008**, *105*, 14265–14270.

[59] M. A. Dobrovolskaia, A. K. Patri, J. Zheng, J. D. Clogston, N. Ayub, P. Aggarwal, B. W. Neun, J. B. Hall, S. E. McNeil, *Nanomedicine: Nanotechnology, Biology and Medicine* **2009**, *5*, 106–117.

[60] S. H. D. P. Lacerda, J. J. Park, C. Meuse, D. Pristinski, M. L. Becker, A. Karim, J. F. Douglas, *ACS Nano* **2010**, *4*, 365–379.

[61] C. D. Walkey, J. B. Olsen, H. Guo, A. Emili, W. C. W. Chan, *J. Am. Chem. Soc.* **2012**, *134*, 2139–2147.

[62] S. Tenzer, D. Docter, S. Rosfa, A. Wlodarski, J. Kuharev, A. Rekik, S. K. Knauer, C. Bantz, T. Nawroth, C. Bier, et al., *ACS Nano* **2011**, *5*, 7155–7167.

[63] F. Turci, E. Ghibaudi, M. Colonna, B. Boscolo, I. Fenoglio, B. Fubini, *Langmuir* **2010**, *26*, 8336–8346.

[64] C. C. Fleischer, C. K. Payne, *J Phys Chem B* **2014**, *118*, 14017–14026.

[65] D. Hühn, K. Kantner, C. Geidel, S. Brandholt, I. De Cock, S. J. H. Soenen, P. Rivera_Gil, J.-M. Montenegro, K. Braeckmans, K. Müllen, et al., *ACS Nano* **2013**, *7*, 3253–3263.

[66] S. Chakraborty, P. Joshi, V. Shanker, Z. A. Ansari, S. P. Singh, P. Chakrabarti, *Langmuir* **2011**, *27*, 7722–7731.

[67] T. Cedervall, I. Lynch, S. Lindman, T. Berggård, E. Thulin, H. Nilsson, K. A. Dawson, S. Linse, *Proc. Natl. Acad. Sci. U.S.A.* **2007**, *104*, 2050–2055.

[68] A. Dolatshahi-Pirouz, K. Rechendorff, M. B. Hovgaard, M. Foss, J. Chevallier, F. Besenbacher, *Colloids Surf B Biointerfaces* **2008**, *66*, 53–59.

[69] J. E. Gagner, M. D. Lopez, J. S. Dordick, R. W. Siegel, *Biomaterials* **2011**, *32*, 7241–7252.

[70] M. P. Monopoli, D. Walczyk, A. Campbell, G. Elia, I. Lynch, F. Baldelli Bombelli, K. A. Dawson, *J. Am. Chem. Soc.* **2011**, *133*, 2525–2534.

[71] T. Osaka, T. Nakanishi, S. Shanmugam, S. Takahama, H. Zhang, *Colloids and Surfaces B: Biointerfaces* **2009**, *71*, 325–330.

[72] G. M. Cooper, *The Cell: A Molecular Approach. 2nd edition* **2000**.

[73] S. R. Elkin, A. M. Lakoduk, S. L. Schmid, *Wien Med Wochenschr* **2016**, *166*, 196–204.

[74] S. Behzadi, V. Serpooshan, W. Tao, M. A. Hamaly, M. Y. Alkawareek, E. C. Dreaden, D. Brown, A. M. Alkilany, O. C. Farokhzad, M. Mahmoudi, *Chem. Soc. Rev.* **2017**, *46*, 4218–4244.

[75] S. Mayor, R. E. Pagano, *Nature Reviews Molecular Cell Biology* **2007**, *8*, 603–612.

[76] S. Arandjelovic, K. S. Ravichandran, *Nature Immunology* **2015**, *16*, 907–917.

[77] S. Gordon, *Immunity* **2016**, *44*, 463–475.

[78] C. Rosales, E. Uribe-Querol, *Biomed Res Int* **2017**, *2017*, DOI 10.1155/2017/9042851.

[79] M. L. Litvack, N. Palaniyar, *Innate Immun* **2010**, *16*, 191–200.

[80] A. Doni, C. Garlanda, A. Mantovani, *Semin Immunol* **2016**, *28*, 570–577.

[81] J. P. Lim, P. A. Gleeson, *Immunology & Cell Biology* **2011**, *89*, 836–843.

[82] King Jason S., Kay Robert R., *Philosophical Transactions of the Royal Society B: Biological Sciences* **2019**, *374*, 20180158.

[83] P. E. Strømhaug, T. O. Berg, T. Gjøen, P. O. Seglen, *Eur. J. Cell Biol.* **1997**, *73*, 28–39.

[84] M. Kaksonen, A. Roux, *Nature Reviews Molecular Cell Biology* **2018**, *19*, 313–326.

[85] J. L. Carpentier, P. Gorden, R. G. Anderson, J. L. Goldstein, M. S. Brown, S. Cohen, L. Orci, *J. Cell Biol.* **1982**, *95*, 73–77.

[86] M. R. Neutra, A. Ciechanover, L. S. Owen, H. F. Lodish, *J. Histochem. Cytochem.* **1985**, *33*, 1134–1144.

[87] L. Pelkmans, A. Helenius, *Traffic* **2002**, *3*, 311–320.

[88] R. G. Parton, *Annual Review of Cell and Developmental Biology* **2018**, *34*, 111–136.

[89] L. Pelkmans, J. Kartenbeck, A. Helenius, *Nat Cell Biol* **2001**, *3*, 473–483.

[90] R. G. Parton, K. Simons, *Nature Reviews Molecular Cell Biology* **2007**, *8*, 185–194.

[91] R. D. Minshall, C. Tiruppathi, S. M. Vogel, W. D. Niles, A. Gilchrist, H. E. Hamm, A. B. Malik, *The Journal of Cell Biology* **2000**, *150*, 1057–1070.

[92] W. Schubert, P. G. Frank, B. Razani, D. S. Park, C.-W. Chow, M. P. Lisanti, *J. Biol. Chem.* **2001**, *276*, 48619–48622.

[93] B.-I. Rosengren, A. Rippe, C. Rippe, D. Venturoli, K. Swärd, B. Rippe, *American Journal of Physiology-Heart and Circulatory Physiology* **2006**, *291*, H1371–H1377.

[94] K. Miyawaki-Shimizu, D. Predescu, J. Shimizu, M. Broman, S. Predescu, A. B. Malik, *American Journal of Physiology-Lung Cellular and Molecular Physiology* **2006**, *290*, L405–L413.

[95] K. Takei, P. S. McPherson, S. L. Schmid, P. D. Camilli, *Nature* **1995**, *374*, 186–190.

[96] J. R. Henley, E. W. Krueger, B. J. Oswald, M. A. McNiven, *J. Cell Biol.* **1998**, *141*, 85–99.

[97] S. L. Schmid, V. A. Frolov, *Annual Review of Cell and Developmental Biology* **2011**, *27*, 79–105.

[98] S. Mayor, R. G. Parton, J. G. Donaldson, *Cold Spring Harb Perspect Biol* **2014**, *6*, DOI 10.1101/cshperspect.a016758.

[99] S. Sabharanjak, P. Sharma, R. G. Parton, S. Mayor, *Developmental Cell* **2002**, *2*, 411–423.

[100] M. Kirkham, A. Fujita, R. Chadda, S. J. Nixon, T. V. Kurzchalia, D. K. Sharma, R. E. Pagano, J. F. Hancock, S. Mayor, R. G. Parton, *The Journal of Cell Biology* **2005**, *168*, 465–476.

[101] H. Radhakrishna, J. G. Donaldson, *The Journal of Cell Biology* **1997**, *139*, 49–61.

[102] B. D. Grant, J. G. Donaldson, *Nat Rev Mol Cell Biol* **2009**, *10*, 597–608.

[103] Y. He, K. Park, *Mol. Pharmaceutics* **2016**, *13*, 2164–2171.

[104] J. Rejman, V. Oberle, I. S. Zuhorn, D. Hoekstra, *Biochem J* **2004**, *377*, 159–169.

[105] J.-S. Shin, Z. Gao, S. N. Abraham, *Science* **2000**, *289*, 785–788.

[106] K. G. Rothberg, Y. S. Ying, J. F. Kolhouse, B. A. Kamen, R. G. Anderson, *The Journal of Cell Biology* **1990**, *110*, 637–649.

[107] S. Rijnboutt, G. Jansen, G. Posthuma, J. B. Hynes, J. H. Schornagel, G. J. Strous, *The Journal of Cell Biology* **1996**, *132*, 35–47.

[108] W. J. Gradishar, *Expert Opinion on Pharmacotherapy* **2006**, *7*, 1041–1053.

[109] G. Sahay, D. Y. Alakhova, A. V. Kabanov, *Journal of Controlled Release* **2010**, *145*, 182–195.

[110] I. Mellman, R. Fuchs, A. Helenius, *Annual Review of Biochemistry* **1986**, *55*, 663–700.

[111] V. Marshansky, M. Futai, *Current Opinion in Cell Biology* **2008**, *20*, 415–426.

[112] J. Huotari, A. Helenius, *EMBO J.* **2011**, *30*, 3481–3500.

[113] R. Levin, S. Grinstein, J. Canton, *Immunological Reviews* **2016**, *273*, 156–179.

[114] A. Jankowski, C. C. Scott, S. Grinstein, *J. Biol. Chem.* **2002**, *277*, 6059–6066.

[115] J. Canton, R. Khezri, M. Glogauer, S. Grinstein, *MBoC* **2014**, *25*, 3330–3341.

[116] H. A. Anderson, Y. Chen, L. C. Norkin, *Mol Biol Cell* **1996**, *7*, 1825–1834.

[117] R. Tamai, Y. Asai, T. Ogawa, *Infection and Immunity* **2005**, *73*, 6290–6298.

[118] L. M. Bareford, P. W. Swaan, *Adv Drug Deliv Rev* **2007**, *59*, 748–758.

[119] E. Terreno, S. G. Crich, S. Belfiore, L. Biancone, C. Cabella, G. Esposito, A. D. Manazza, S. Aime, *Magnetic Resonance in Medicine* **2006**, *55*, 491–497.

[120] J. T. Rosenberg, J. M. Kogot, D. D. Lovingood, G. F. Strouse, S. C. Grant, *Magnetic Resonance in Medicine* **2010**, *64*, 871–882.

[121] J. T. Rosenberg, A. Sachi-Kocher, M. W. Davidson, S. C. Grant, *Contrast Media & Molecular Imaging* **2012**, *7*, 121–129.

[122] K. Kostarelos, L. Lacerda, G. Pastorin, W. Wu, S. Wieckowski, J. Luangsivilay, S. Godefroy, D. Pantarotto, J.-P. Briand, S. Muller, et al., *Nature Nanotechnology* **2007**, *2*, 108–113.

[123] T. Wang, J. Bai, X. Jiang, G. U. Nienhaus, *ACS Nano* **2012**, *6*, 1251–1259.

[124] L. N. Patel, J. L. Zaro, W.-C. Shen, *Pharm Res* **2007**, *24*, 1977–1992.

[125] F. Milletti, *Drug Discovery Today* **2012**, *17*, 850–860.

[126] H. Derakhshankhah, S. Jafari, *Biomedicine & Pharmacotherapy* **2018**, *108*, 1090–1096.

[127] J. M. de la Fuente, C. C. Berry, *Bioconjugate Chem.* **2005**, *16*, 1176–1180.

[128] O. A. Garden, P. R. Reynolds, J. Yates, D. J. Larkman, F. M. Marelli-Berg, D. O. Haskard, A. D. Edwards, A. J. T. George, *J. Immunol. Methods* **2006**, *314*, 123–133.

[129] V. P. Torchilin, R. Rammohan, V. Weissig, T. S. Levchenko, *PNAS* **2001**, *98*, 8786–8791.

[130] V. P. Torchilin, T. S. Levchenko, R. Rammohan, N. Volodina, B. Papahadjopoulos-Sternberg, G. G. M. D'Souza, *Proc Natl Acad Sci U S A* **2003**, *100*, 1972–1977.

[131] I. A. Khalil, K. Kogure, S. Futaki, H. Harashima, *J. Biol. Chem.* **2006**, *281*, 3544–3551.

[132] Y. Ding, D. Sun, G.-L. Wang, H.-G. Yang, H.-F. Xu, J.-H. Chen, Y. Xie, Z.-Q. Wang, *Int J Nanomedicine* **2015**, *10*, 6199–6214.

[133] E. Kleemann, M. Neu, N. Jekel, L. Fink, T. Schmehl, T. Gessler, W. Seeger, T. Kissel, *Journal of Controlled Release* **2005**, *109*, 299–316.

[134] A. Verma, O. Uzun, Y. Hu, Y. Hu, H.-S. Han, N. Watson, S. Chen, D. J. Irvine, F. Stellacci, *Nat Mater* **2008**, *7*, 588–595.

[135] J.-P. Behr, "The Proton Sponge: a Trick to Enter Cells the Viruses Did Not Exploit," can be found under https://www.ingentaconnect.com/content/scs/chimia/1997/00000051/F0020001/art00026#, **1997**.

[136] N. D. Sonawane, F. C. Szoka, A. S. Verkman, *J. Biol. Chem.* **2003**, *278*, 44826–44831.

[137] T. F. Martens, K. Remaut, J. Demeester, S. C. De Smedt, K. Braeckmans, *Nano Today* **2014**, *9*, 344–364.

[138] Y. Hu, T. Litwin, A. R. Nagaraja, B. Kwong, J. Katz, N. Watson, D. J. Irvine, *Nano Lett.* **2007**, *7*, 3056–3064.

[139] Y. W. Cho, J.-D. Kim, K. Park, *Journal of Pharmacy and Pharmacology* **2003**, *55*, 721–734.

[140] D. W. Lim, Y. I. Yeom, T. G. Park, *Bioconjugate Chem.* **2000**, *11*, 688–695.

[141] N. M. Moore, C. L. Sheppard, T. R. Barbour, S. E. Sakiyama-Elbert, *The Journal of Gene Medicine* **2008**, *10*, 1134–1149.

[142] S. Hong, P. R. Leroueil, E. K. Janus, J. L. Peters, M.-M. Kober, M. T. Islam, B. G. Orr, J. R. Baker, M. M. Banaszak Holl, *Bioconjugate Chem.* **2006**, *17*, 728–734.

[143] N. Feliu, D. Docter, M. Heine, P. del Pino, S. Ashraf, J. Kolosnjaj-Tabi, P. Macchiarini, P. Nielsen, D. Alloyeau, F. Gazeau, et al., *Chem. Soc. Rev.* **2016**, *45*, 2440–2457.

[144] M. I. Setyawati, C. Y. Tay, D. Docter, R. H. Stauber, D. T. Leong, *Chem. Soc. Rev.* **2015**, *44*, 8174–8199.

[145] J. Lazarovits, Y. Y. Chen, E. A. Sykes, W. C. W. Chan, *Chem. Commun.* **2015**, *51*, 2756–2767.

[146] S. M. Moghimi, A. C. Hunter, T. L. Andresen, *Annual Review of Pharmacology and Toxicology* **2012**, *52*, 481–503.

[147] E. Blanco, H. Shen, M. Ferrari, *Nat Biotechnol* **2015**, *33*, 941–951.

[148] W. C. Aird, *Circulation Research* **2007**, *100*, 158–173.

[149] J. Rostgaard, K. Qvortrup, *Microvascular Research* **1997**, *53*, 1–13.

[150] A. B. Engin, D. Nikitovic, M. Neagu, P. Henrich-Noack, A. O. Docea, M. I. Shtilman, K. Golokhvast, A. M. Tsatsakis, *Part Fibre Toxicol* **2017**, *14*, DOI 10.1186/s12989-017-0199-z.

[151] R. K. Jain, T. Stylianopoulos, *Nature Reviews Clinical Oncology* **2010**, *7*, 653–664.

[152] H. H. Gustafson, D. Holt-Casper, D. W. Grainger, H. Ghandehari, *Nano Today* **2015**, *10*, 487–510.

[153] G. Song, J. S. Petschauer, A. J. M. and W. C. Zamboni, “Nanoparticles and the Mononuclear Phagocyte System: Pharmacokinetics and Applications for Inflammatory Diseases,” can be found under http://www.eurekaselect.com/124549/article, **2014**.

[154] S. M. Moghimi, C. J. H. Porter, I. S. Muir, L. Illum, S. S. Davis, *Biochemical and Biophysical Research Communications* **1991**, *177*, 861–866.

[155] I. V. Pivkin, Z. Peng, G. E. Karniadakis, P. A. Buffet, M. Dao, S. Suresh, *Proc Natl Acad Sci U S A* **2016**, *113*, 7804–7809.

[156] M. Demoy, J.-P. Andreux, C. Weingarten, B. Gouritin, V. Guilloux, P. Couvreur, *Life Sciences* **1999**, *64*, 1329–1337.

[157] M. Cataldi, C. Vigliotti, T. Mosca, M. Cammarota, D. Capone, *Int J Mol Sci* **2017**, *18*, DOI 10.3390/ijms18061249.

[158] S. M. Moghimi, H. Hedeman, I. S. Muir, L. Illum, S. S. Davis, *Biochimica et Biophysica Acta (BBA) - General Subjects* **1993**, *1157*, 233–240.

[159] B. Steiniger, P. Barth, A. Hellinger, *The American Journal of Pathology* **2001**, *159*, 501–512.

[160] B. S. Steiniger, *Immunology* **2015**, *145*, 334–346.

[161] C. S. Thaxton, J. S. Rink, P. C. Naha, D. P. Cormode, *Adv Drug Deliv Rev* **2016**, *106*, 116–131.

[162] M. Naito, G. Hasegawa, Y. Ebe, T. Yamamoto, *Med Electron Microsc* **2004**, *37*, 16–28.

[163] M. Bilzer, F. Roggel, A. L. Gerbes, *Liver International* **2006**, *26*, 1175–1186.

[164] F. Braet, E. Wisse, *Comparative Hepatology* **2002**, *1*, 1.

[165] B. Du, M. Yu, J. Zheng, *Nat Rev Mater* **2018**, *3*, 358–374.

[166] J. Liu, M. Yu, C. Zhou, J. Zheng, *Materials Today* **2013**, *16*, 477–486.

[167] M. Yu, J. Zheng, *ACS Nano* **2015**, *9*, 6655–6674.

[168] I. Cicha, *Journal of Cellular Biotechnology* **2016**, *1*, 191–208.

[169] R. Molinaro, C. Boada, G. M. del Rosal, K. A. Hartman, C. Corbo, E. D. Andrews, N. E. Toledano-Furman, J. P. Cooke, E. Tasciotti, *Methodist Debakey Cardiovasc J* **2016**, *12*, 169–174.

[170] J. Folkman, *New England Journal of Medicine* **1971**, *285*, 1182–1186.

[171] J. D. Byrne, T. Betancourt, L. Brannon-Peppas, *Advanced Drug Delivery Reviews* **2008**, *60*, 1615–1626.

[172] J. A. Nagy, S.-H. Chang, A. M. Dvorak, H. F. Dvorak, *Br J Cancer* **2009**, *100*, 865–869.

[173] A. Raza, M. J. Franklin, A. Z. Dudek, *American Journal of Hematology* **2010**, *85*, 593–598.

[174] P. Baluk, S. Morikawa, A. Haskell, M. Mancuso, D. M. McDonald, *Am J Pathol* **2003**, *163*, 1801–1815.

[175] H. Hashizume, P. Baluk, S. Morikawa, J. W. McLean, G. Thurston, S. Roberge, R. K. Jain, D. M. McDonald, *Am J Pathol* **2000**, *156*, 1363–1380.

[176] T. P. Padera, E. F. J. Meijer, L. L. Munn, *Annu Rev Biomed Eng* **2016**, *18*, 125–158.

[177] Y. Matsumura, H. Maeda, *Cancer Res.* **1986**, *46*, 6387–6392.

[178] Y. Boucher, L. T. Baxter, R. K. Jain, *Cancer Research* **1990**, *50*, 4478–4484.

[179] L. L. Munn, *Drug Discovery Today* **2003**, *8*, 396–403.

[180] A. Eberhard, S. Kahlert, V. Goede, B. Hemmerlein, K. H. Plate, H. G. Augustin, *Cancer Res* **2000**, *60*, 1388–1393.

[181] S. Wilhelm, A. J. Tavares, Q. Dai, S. Ohta, J. Audet, H. F. Dvorak, W. C. W. Chan, *Nature Reviews Materials* **2016**, *1*, 16014.

[182] K. J. Harrington, S. Mohammadtaghi, P. S. Uster, D. Glass, A. M. Peters, R. G. Vile, J. S. W. Stewart, *Clin Cancer Res* **2001**, *7*, 243–254.

[183] J. P. Luzio, P. R. Pryor, N. A. Bright, *Nature Reviews Molecular Cell Biology* **2007**, *8*, 622–632.

[184] B. Li, L. A. Lane, *Wiley Interdisciplinary Reviews: Nanomedicine and Nanobiotechnology* **2019**, *11*, e1542.

[185] G. Renaud, R. L. Hamilton, R. J. Havel, *Hepatology* **1989**, *9*, 380–392.

[186] Y.-N. Zhang, W. Poon, A. J. Tavares, I. D. McGilvray, W. C. W. Chan, *Journal of Controlled Release* **2016**, *240*, 332–348.

[187] H. Wang, C. A. Thorling, X. Liang, K. R. Bridle, J. E. Grice, Y. Zhu, D. H. G. Crawford, Z. P. Xu, X. Liu, M. S. Roberts, *J. Mater. Chem. B* **2015**, *3*, 939–958.

[188] P. Bourrinet, H. Bengele, B. Bonnemain, A. Dencausse, J.-M. Idee, P. Jacobs, J. Lewis, *Investigative Radiology* **2006**, *41*, 313–324.

[189] P. Cherukuri, S. M. Bachilo, S. H. Litovsky, R. B. Weisman, *J. Am. Chem. Soc.* **2004**, *126*, 15638–15639.

[190] D. Elgrabli, W. Dachraoui, C. Ménard-Moyon, X. J. Liu, D. Bégin, S. Bégin-Colin, A. Bianco, F. Gazeau, D. Alloyeau, *ACS Nano* **2015**, *9*, 10113–10124.

[191] C. Farrera, K. Bhattacharya, B. Lazzaretto, F. T. Andón, K. Hultenby, G. P. Kotchey, A. Star, B. Fadeel, *Nanoscale* **2014**, *6*, 6974–6983.

[192] V. E. Kagan, A. A. Kapralov, C. M. St. Croix, S. C. Watkins, E. R. Kisin, G. P. Kotchey, K. Balasubramanian, I. I. Vlasova, J. Yu, K. Kim, et al., *ACS Nano* **2014**, *8*, 5610–5621.

[193] L. Lartigue, D. Alloyeau, J. Kolosnjaj-Tabi, Y. Javed, P. Guardia, A. Riedinger, C. Péchoux, T. Pellegrino, C. Wilhelm, F. Gazeau, *ACS Nano* **2013**, *7*, 3939–3952.

[194] J. Kolosnjaj-Tabi, Y. Javed, L. Lartigue, J. Volatron, D. Elgrabli, I. Marangon, G. Pugliese, B. Caron, A. Figuerola, N. Luciani, et al., *ACS Nano* **2015**, *9*, 7925–7939.

[195] D. Bargheer, A. Giemsa, B. Freund, M. Heine, C. Waurisch, G. M. Stachowski, S. G. Hickey, A. Eychmüller, J. Heeren, P. Nielsen, *Beilstein J. Nanotechnol.* **2015**, *6*, 111–123.

[196] F. Mazuel, A. Espinosa, N. Luciani, M. Reffay, R. Le Borgne, L. Motte, K. Desboeufs, A. Michel, T. Pellegrino, Y. Lalatonne, et al., *ACS Nano* **2016**, *10*, 7627–7638.

[197] E. Sadauskas, G. Danscher, M. Stoltenberg, U. Vogel, A. Larsen, H. Wallin, *Nanomedicine* **2009**, *5*, 162–169.

[198] S. C. Gad, K. L. Sharp, C. Montgomery, J. D. Payne, G. P. Goodrich, *Int J Toxicol* **2012**, *31*, 584–594.

[199] S. Fraga, A. Brandão, M. E. Soares, T. Morais, J. A. Duarte, L. Pereira, L. Soares, C. Neves, E. Pereira, M. de L. Bastos, et al., *Nanomedicine: Nanotechnology, Biology and Medicine* **2014**, *10*, 1757–1766.

[200] J. Kolosnjaj-Tabi, J. Volatron, F. Gazeau, in *Design and Applications of Nanoparticles in Biomedical Imaging* (Eds.: J.W.M. Bulte, M.M.J. Modo), Springer International Publishing, Cham, **2017**, pp. 9–41.

[201] J. R. Hoidal, G. D. Beall, J. E. Repine, *Infect Immun* **1979**, *26*, 1088–1092.

[202] A. M. Nowicka, U. Hasse, M. Hermes, F. Scholz, *Angewandte Chemie International Edition* **2010**, *49*, 1061–1063.

[203] T.-H. Chen, C.-C. Nieh, Y.-C. Shih, C.-Y. Ke, W.-L. Tseng, *RSC Advances* **2015**, *5*, 45158–45164.

[204] D. Krüger, R. Rousseau, H. Fuchs, D. Marx, *Angewandte Chemie International Edition* **2003**, *42*, 2251–2253.

[205] M. Paulsson, C. Krag, T. Frederiksen, M. Brandbyge, *Nano Lett.* **2009**, *9*, 117–121.

[206] Y. Javed, L. Lartigue, P. Hugounenq, Q. L. Vuong, Y. Gossuin, R. Bazzi, C. Wilhelm, C. Ricolleau, F. Gazeau, D. Alloyeau, *Small* **2014**, *10*, 3325–3337.

[207] H. A. Havel, *AAPS J* **2016**, *18*, 1351–1353.

[208] A. Radomska, J. Leszczyszyn, M. W. Radomski, *Adv Clin Exp Med* **2016**, *25*, 151–162.

[209] K. O. Alfarouk, D. Verduzco, C. Rauch, A. K. Muddathir, H. H. B. Adil, G. O. Elhassan, M. E. Ibrahim, J. David Polo Orozco, R. A. Cardone, S. J. Reshkin, et al., *Oncoscience* **2014**, *1*, 777–802.

[210] M. Damaghi, J. W. Wojtkowiak, R. J. Gillies, *Front Physiol* **2013**, *4*, DOI 10.3389/fphys.2013.00370.

[211] N. Deirram, C. Zhang, S. S. Kermaniyan, A. P. R. Johnston, G. K. Such, *Macromolecular Rapid Communications* **2019**, *40*, 1800917.

[212] W. Gao, J. Chan, O. C. Farokhzad, *Mol Pharm* **2010**, *7*, 1913–1920.

[213] M. Dominska, D. M. Dykxhoorn, *J Cell Sci* **2010**, *123*, 1183–1189.

[214] S. Aryal, C.-M. J. Hu, L. Zhang, *ACS Nano* **2010**, *4*, 251–258.

[215] R. M. Sawant, J. P. Hurley, S. Salmaso, A. Kale, E. Tolcheva, T. S. Levchenko, V. P. Torchilin, *Bioconjug Chem* **2006**, *17*, 943–949.

[216] A. P. Griset, J. Walpole, R. Liu, A. Gaffey, Y. L. Colson, M. W. Grinstaff, *J. Am. Chem. Soc.* **2009**, *131*, 2469–2471.

[217] Y. Yao, P. E. Saw, Y. Nie, P.-P. Wong, L. Jiang, X. Ye, J. Chen, T. Ding, L. Xu, H. Yao, et al., *J. Mater. Chem. B* **2019**, *7*, 576–585.

[218] W. Wu, L. Luo, Y. Wang, Q. Wu, H.-B. Dai, J.-S. Li, C. Durkan, N. Wang, G.-X. Wang, *Theranostics* **2018**, *8*, 3038–3058.

[219] J.-H. Kang, D. Asai, J.-H. Kim, T. Mori, R. Toita, T. Tomiyama, Y. Asami, J. Oishi, Y. T. Sato, T. Niidome, et al., *J. Am. Chem. Soc.* **2008**, *130*, 14906–14907.

[220] C. Wong, T. Stylianopoulos, J. Cui, J. Martin, V. P. Chauhan, W. Jiang, Z. Popović, R. K. Jain, M. G. Bawendi, D. Fukumura, *PNAS* **2011**, *108*, 2426–2431.

[221] G. Hu, X. Chun, Y. Wang, Q. He, H. Gao, *Oncotarget* **2015**, *6*, 41258–41274.

[222] Q. Hu, P. S. Katti, Z. Gu, *Nanoscale* **2014**, *6*, 12273–12286.

[223] X. Guo, X. Wei, Y. Jing, S. Zhou, *Advanced Materials* **2015**, *27*, 6450–6456.

[224] X. Meng, Y. Yang, L. Zhou, li Zhang, Y. Lv, S. Li, Y. Wu, M. Zheng, W. Li, G. Gao, et al., *Theranostics* **2017**, *7*, 1781–1794.

[225] X. Guo, Y. Cheng, X. Zhao, Y. Luo, J. Chen, W.-E. Yuan, *Journal of Nanobiotechnology* **2018**, *16*, 74.

[226] S. Khoee, M. R. Karimi, *Polymer* **2018**, *142*, 80–98.

[227] M. de Smet, E. Heijman, S. Langereis, N. M. Hijnen, H. Grüll, *Journal of Controlled Release* **2011**, *150*, 102–110.

[228] A. Ranjan, G. Jacobs, D. L. Woods, A. H. Negussie, A. Partanen, P. S. Yarmolenko, C. E. Gacchina, K. V. Sharma, V. Frenkel, B. J. Wood, et al., *J Control Release* **2012**, *158*, 487–494.

[229] T. Li, L. Lu, Y. Qiao, S. Ravi, F. Salatan, M. P. Melancon, *J Funct Biomater* **2016**, *7*, 19.

[230] X. Huang, I. H. El-Sayed, W. Qian, M. A. El-Sayed, *J. Am. Chem. Soc.* **2006**, *128*, 2115–2120.

[231] H. Kang, A. C. Trondoli, G. Zhu, Y. Chen, Y.-J. Chang, H. Liu, Y.-F. Huang, X. Zhang, W. Tan, *ACS Nano* **2011**, *5*, 5094–5099.

[232] A. R. Guerrero, N. Hassan, C. A. Escobar, F. Albericio, M. J. Kogan, E. Araya, *Nanomedicine* **2014**, *9*, 2023–2039.

[233] A. Raza, U. Hayat, T. Rasheed, M. Bilal, H. M. N. Iqbal, *Journal of Materials Research and Technology* **2019**, *8*, 1497–1509.

[234] G. D. Moon, S.-W. Choi, X. Cai, W. Li, E. C. Cho, U. Jeong, L. V. Wang, Y. Xia, *J Am Chem Soc* **2011**, *133*, 4762–4765.

[235] H. Ju, R. A. Roy, T. W. Murray, *Biomed Opt Express* **2013**, *4*, 66–76.

[236] N. Lewinski, V. Colvin, R. Drezek, *Small* **2008**, *4*, 26–49.

[237] A. M. Alkilany, C. J. Murphy, *J Nanopart Res* **2010**, *12*, 2313–2333.

[238] D. Xi, S. Dong, X. Meng, Q. Lu, L. Meng, J. Ye, *RSC Adv.* **2012**, *2*, 12515–12524.

[239] C. M. Goodman, C. D. McCusker, T. Yilmaz, V. M. Rotello, *Bioconjugate Chem.* **2004**, *15*, 897–900.

[240] S. J. Soenen, B. B. Manshian, A. M. Abdelmonem, J.-M. Montenegro, S. Tan, L. Balcaen, F. Vanhaecke, A. R. Brisson, W. J. Parak, S. C. De Smedt, et al., *Part. Part. Syst. Charact.* **2014**, *31*, 794–800.

[241] H. Yen, S. Hsu, C. Tsai, *Small* **2009**, *5*, 1553–1561.

[242] W.-S. Cho, M. Cho, J. Jeong, M. Choi, H.-Y. Cho, B. S. Han, S. H. Kim, H. O. Kim, Y. T. Lim, B. H. Chung, et al., *Toxicology and Applied Pharmacology* **2009**, *236*, 16–24.

[243] X. Ma, Y. Wu, S. Jin, Y. Tian, X. Zhang, Y. Zhao, L. Yu, X.-J. Liang, *ACS Nano* **2011**, *5*, 8629–8639.

[244] S. T. Stern, P. P. Adiseshaiah, R. M. Crist, *Particle and Fibre Toxicology* **2012**, *9*, 20.

[245] A. M. Alkilany, P. K. Nagaria, C. R. Hexel, T. J. Shaw, C. J. Murphy, M. D. Wyatt, *Small* **2009**, *5*, 701–708.

[246] Y. Qiu, Y. Liu, L. Wang, L. Xu, R. Bai, Y. Ji, X. Wu, Y. Zhao, Y. Li, C. Chen, *Biomaterials* **2010**, *31*, 7606–7619.

[247] Y.-S. Chen, Y.-C. Hung, I. Liau, G. S. Huang, *Nanoscale Res Lett* **2009**, *4*, 858–864.

[248] Y. Pan, S. Neuss, A. Leifert, M. Fischler, F. Wen, U. Simon, G. Schmid, W. Brandau, W. Jahnen-Dechent, *Small* **2007**, *3*, 1941–1949.

[249] E. E. Connor, J. Mwamuka, A. Gole, C. J. Murphy, M. D. Wyatt, *Small* **2005**, *1*, 325–327.

[250] R. Shukla, V. Bansal, M. Chaudhary, A. Basu, R. R. Bhonde, M. Sastry, *Langmuir* **2005**, *21*, 10644–10654.

[251] C. Villiers, H. Freitas, R. Couderc, M.-B. Villiers, P. Marche, *J Nanopart Res* **2010**, *12*, 55–60.

[252] J. F. Hainfeld, D. N. Slatkin, T. M. Focella, H. M. Smilowitz, *BJR* **2006**, *79*, 248–253.

[253] C. Lasagna-Reeves, D. Gonzalez-Romero, M. A. Barria, I. Olmedo, A. Clos, V. M. Sadagopa Ramanujam, A. Urayama, L. Vergara, M. J. Kogan, C. Soto, *Biochemical and Biophysical Research Communications* **2010**, *393*, 649–655.

[254] X.-D. Zhang, H.-Y. Wu, D. Wu, Y.-Y. Wang, J.-H. Chang, Z.-B. Zhai, A.-M. Meng, P.-X. Liu, L.-A. Zhang, F.-Y. Fan, "Toxicologic effects of gold nanoparticles in vivo by different administration routes," DOI 10.2147/IJN.S8428can be found under https://www.dovepress.com/toxicologic-effects-of-gold-nanoparticles-in-vivo-by-different-adminis-peer-reviewed-article-IJN, **2010**.

[255] J. M. Stern, V. V. Kibanov Solomonov, E. Sazykina, J. A. Schwartz, S. C. Gad, G. P. Goodrich, *Int J Toxicol* **2016**, *35*, 38–46.

[256] A. R. Rastinehad, H. Anastos, E. Wajswol, J. S. Winoker, J. P. Sfakianos, S. K. Doppalapudi, M. R. Carrick, C. J. Knauer, B. Taouli, S. C. Lewis, et al., *PNAS* **2019**, 201906929.

[257] S. Jain, D. G. Hirst, J. M. O'Sullivan, *Br J Radiol* **2012**, *85*, 101–113.

[258] P. Singh, S. Pandit, V. R. S. S. Mokkapati, A. Garg, V. Ravikumar, I. Mijakovic, *Int J Mol Sci* **2018**, *19*, DOI 10.3390/ijms19071979.

[259] P. Boyle, *Ann Oncol* **2012**, *23*, vi7–vi12.

[260] C. M. Perou, T. Sørlie, M. B. Eisen, M. van de Rijn, S. S. Jeffrey, C. A. Rees, J. R. Pollack, D. T. Ross, H. Johnsen, L. A. Akslen, et al., *Nature* **2000**, *406*, 747–752.

[261] H. Rochefort, M. Glondu, M. E. Sahla, N. Platet, M. Garcia, *Endocr. Relat. Cancer* **2003**, *10*, 261–266.

[262] M. V. Yezhelyev, X. Gao, Y. Xing, A. Al-Hajj, S. Nie, R. M. O'Regan, *The Lancet Oncology* **2006**, *7*, 657–667.

[263] J. Lee, D. K. Chatterjee, M. H. Lee, S. Krishnan, *Cancer Lett* **2014**, *347*, 46–53.

[264] T. Dreifuss, E. Barnoy, M. Motiei, R. Popovtzer, in *Design and Applications of Nanoparticles in Biomedical Imaging* (Eds.: J.W.M. Bulte, M.M.J. Modo), Springer International Publishing, Cham, **2017**, pp. 403–427.

[265] M. M. Mahan, A. L. Doiron, "Gold Nanoparticles as X-Ray, CT, and Multimodal Imaging Contrast Agents: Formulation, Targeting, and Methodology," DOI 10.1155/2018/5837276can be found under https://www.hindawi.com/journals/jnm/2018/5837276/, **2018**.

[266] J. F. Hainfeld, D. N. Slatkin, H. M. Smilowitz, *Phys. Med. Biol.* **2004**, *49*, N309–N315.

[267] R. Popovtzer, A. Agrawal, N. A. Kotov, A. Popovtzer, J. Balter, Thomas. E. Carey, R. Kopelman, *Nano Lett.* **2008**, *8*, 4593–4596.

[268] J. Li, A. Chaudhary, S. J. Chmura, C. Pelizzari, T. Rajh, C. Wietholt, M. Kurtoglu, B. Aydogan, *Phys. Med. Biol.* **2010**, *55*, 4389–4397.

[269] W. Eck, A. I. Nicholson, H. Zentgraf, W. Semmler, S. Bartling, *Nano Lett.* **2010**, *10*, 2318–2322.

[270] G. Feng, B. Kong, J. Xing, J. Chen, *Clinical Radiology* **2014**, *69*, 1105–1111.

[271] D. Kim, S. Park, J. H. Lee, Y. Y. Jeong, S. Jon, *J. Am. Chem. Soc.* **2007**, *129*, 7661–7665.

[272] A. Al Zaki, D. Joh, Z. Cheng, A. L. B. De Barros, G. Kao, J. Dorsey, A. Tsourkas, *ACS Nano* **2014**, *8*, 104–112.

[273] J. L. Su, B. Wang, K. E. Wilson, C. L. Bayer, Y.-S. Chen, S. Kim, K. A. Homan, S. Y. Emelianov, *Expert Opin Med Diagn* **2010**, *4*, 497–510.

[274] W. Li, X. Chen, *Nanomedicine (Lond)* **2015**, *10*, 299–320.

[275] Q. Fu, R. Zhu, J. Song, H. Yang, X. Chen, *Advanced Materials* **2019**, *31*, 1805875.

[276] R. Weissleder, *Nat. Biotechnol.* **2001**, *19*, 316–317.

[277] C. Moore, J. V. Jokerst, *Theranostics* **2019**, *9*, 1550–1571.

[278] M. Erfanzadeh, Q. Zhu, *Photoacoustics* **2019**, *14*, 1–11.

[279] V. Amendola, R. Pilot, M. Frasconi, O. M. Maragò, M. A. Iatì, *J. Phys.: Condens. Matter* **2017**, *29*, 203002.

[280] Y. Wu, M. R. K. Ali, K. Chen, N. Fang, M. A. El-Sayed, *Nano Today* **2019**, *24*, 120–140.

[281] I. H. El-Sayed, X. Huang, M. A. El-Sayed, *Nano Lett.* **2005**, *5*, 829–834.

[282] G. Rong, H. Wang, L. R. Skewis, B. M. Reinhard, *Nano Lett.* **2008**, *8*, 3386–3393.

[283] L. Zhang, Y. Li, D.-W. Li, C. Jing, X. Chen, M. Lv, Q. Huang, Y.-T. Long, I. Willner, *Angewandte Chemie International Edition* **2011**, *50*, 6789–6792.

[284] B. Dubertret, M. Calame, A. J. Libchaber, *Nature Biotechnology* **2001**, *19*, 365.

[285] E. Dulkeith, M. Ringler, T. A. Klar, J. Feldmann, A. Muñoz Javier, W. J. Parak, *Nano Lett.* **2005**, *5*, 585–589.

[286] I.-C. Sun, D.-K. Eun, H. Koo, C.-Y. Ko, H.-S. Kim, D. K. Yi, K. Choi, I. C. Kwon, K. Kim, C.-H. Ahn, *Angewandte Chemie International Edition* **2011**, *50*, 9348–9351.

[287] S. Y. Park, S. M. Lee, G. B. Kim, Y.-P. Kim, *Gold Bull* **2012**, *45*, 213–219.

[288] C. Xue, Y. Xue, L. Dai, A. Urbas, Q. Li, *Advanced Optical Materials* **2013**, *1*, 581–587.

[289] T. Luo, P. Huang, G. Gao, G. Shen, S. Fu, D. Cui, C. Zhou, Q. Ren, *Opt Express* **2011**, *19*, 17030–17039.

[290] J.-T. Song, X.-Q. Yang, X.-S. Zhang, D.-M. Yan, Z.-Y. Wang, Y.-D. Zhao, *ACS Appl. Mater. Interfaces* **2015**, *7*, 17287–17297.

[291] G. P. Delaney, M. B. Barton, *Clinical Oncology* **2015**, *27*, 70–76.

[292] D. R. Cooper, D. Bekah, J. L. Nadeau, *Front. Chem.* **2014**, *2*.

[293] K. Haume, S. Rosa, S. Grellet, M. A. Śmiałek, K. T. Butterworth, A. V. Solov'yov, K. M. Prise, J. Golding, N. J. Mason, *Cancer Nanotechnol* **2016**, *7*, DOI 10.1186/s12645-016-0021-x.

[294] W. D. Newhauser, R. Zhang, *Phys. Med. Biol.* **2015**, *60*, R155–R209.

[295] H. Wang, X. Mu, H. He, X.-D. Zhang, *Trends in Pharmacological Sciences* **2018**, *39*, 24–48.

[296] M. Laprise-Pelletier, T. Simão, M.-A. Fortin, *Advanced Healthcare Materials* **2018**, *7*, 1701460.

[297] J. F. Dorsey, L. Sun, D. Y. Joh, A. Witztum, A. A. Zaki, G. D. Kao, M. Alonso, S. Avery, A. Tsourkas, S. M. Hahn, *Translational Cancer Research* **2013**, *2*, 12.

[298] S. X. Zhang, J. Gao, T. A. Buchholz, Z. Wang, M. R. Salehpour, R. A. Drezek, T.-K. Yu, *Biomedical Microdevices* **2009**, *11*, 925.

[299] J. C. Peeken, P. Vaupel, S. E. Combs, *Front Oncol* **2017**, *7*, DOI 10.3389/fonc.2017.00132.

[300] A. C. V. Doughty, A. R. Hoover, E. Layton, C. K. Murray, E. W. Howard, W. R. Chen, *Materials* **2019**, *12*, 779.

[301] H. H. Kampinga, *International Journal of Hyperthermia* **2006**, *22*, 191–196.

[302] J. B. Vines, J.-H. Yoon, N.-E. Ryu, D.-J. Lim, H. Park, *Front. Chem.* **2019**, *7*, DOI 10.3389/fchem.2019.00167.

[303] P. Kaur, M. L. Aliru, A. S. Chadha, A. Asea, S. Krishnan, *Int J Hyperthermia* **2016**, *32*, 76–88.

[304] R. S. Riley, E. S. Day, *Wiley Interdisciplinary Reviews: Nanomedicine and Nanobiotechnology* **2017**, *9*, e1449.

[305] A. Y. Cheung, A. Neyzari, *Cancer Res* **1984**, *44*, 4736s–4744s.

[306] N. S. Abadeer, C. J. Murphy, *J. Phys. Chem. C* **2016**, *120*, 4691–4716.

[307] S. Link, M. El-Sayed, *International Reviews in Physical Chemistry* **2000**, *19*, 409–453.

[308] L. R. Hirsch, R. J. Stafford, J. A. Bankson, S. R. Sershen, B. Rivera, R. E. Price, J. D. Hazle, N. J. Halas, J. L. West, *Proceedings of the National Academy of Sciences of the United States of America* **2003**, *100*, 13549.

[309] C. B. Collins, R. S. McCoy, B. J. Ackerson, G. J. Collins, C. J. Ackerson, *Nanoscale* **2014**, *6*, 8459–8472.

CHAPTER 2: BIODEGRADABLE GOLD NANOCLUSTERS FROM PH-SENSITIVE ACETALATED DEXTRAN

2.1 Abstract

Gold is a highly useful nanomaterial for many clinical applications, but its poor biodegradability can impair long-term physiological clearance. Large gold nanoparticles (20-200 nm), such as those required for long blood circulation times and appreciable tumor localization, often exhibit little to no dissolution and excretion. This can be improved by incorporating small gold particles within a larger entity, but elimination may still be protracted due to incomplete dispersion of gold. The present study describes a novel gold nanoparticle formulation capable of environmentally-triggered decomposition. Ultrasmall gold nanoparticles are coated with thiolated dextran, and hydrophobic acetal groups are installed through direct covalent modification of the dextran. This hydrophobic exterior allows gold to be densely packed within ~150-nm polymeric micelles. Upon exposure to an acidic environment, the acetal groups are removed and the gold nanoparticles become highly water-soluble, leading to destabilization of the micelle. Within 24 hours, the ultrasmall water-soluble gold particles are released from the micelle and readily dispersed. Micelle degradation and gold nanoparticle dispersion was imaged in cultured macrophages, and micelle-treated mice displayed progressive physiological clearance of gold, with > 85% elimination from the liver over three months. These particles present a novel nanomaterial formulation and address a critical unresolved barrier for clinical translation of gold nanoparticles.

2.2 Introduction

Gold nanoparticles (AuNPs) are among the most extensively studied nanoformulations, in part due to their easily manipulatable morphology and surface chemistry as well as their potential to be used in a variety of clinical applications.[1–3] Gold has attracted tremendous interest as a therapeutic agent – particularly in oncology – for applications including radiation sensitization[4–6] and photothermal therapy.[7–9] It has also been explored in various biomedical imaging modalities, including computed tomography (CT),[10–12] photoacoustic imaging,[13,14] and surface-enhanced Raman scattering.[15] Additionally, gold has been complexed with a range of other pharmaceuticals and imaging agents, as a scaffold for targeted delivery and multimodal activity.[12,16–18]

The ability of AuNPs and other nanoparticles to target specific biological compartments is dependent on an optimized particle size (among other properties). Formulating AuNPs of approximately 20-200 nm helps confer long serum circulation times by avoiding rapid renal elimination.[19–21] This also allows particles to preferentially localize to tumors via the enhanced permeability and retention effect (EPR), whereby circulating nanoparticles can extravasate through leaky tumor vasculature and persist due to poor lymphatic drainage.[22,23] However, long-circulating AuNPs can exhibit impaired physiological clearance due to gold's poor biodegradability. Gold particles cannot be easily broken down, even within the lysosomal compartment's highly acidic and hydrolytic environment, though a few processes may contribute to the slow degradation of gold over time (e.g., etching by thiols[24–26] or hydroxyl radicals[27,28]). As a result, gold nanoparticles commonly persist in tissue for weeks to months.[29–31] For example, in a landmark study by Sadauskas et al[32] in which 40-nm AuNPs were

administered intravenously to mice, it was found that only 9% of gold was eliminated from the liver over the course of six months. Similarly, preclinical studies of 150-nm gold nanoshells showed no detectable reduction in total gold mass within the body, even at more than one year post-injection.[29] The long-term persistence of gold nanoparticles represents a significant concern for clinical applications and regulatory approval.[33,34]

In order to improve the clearance of AuNPs while maintaining favorable pharmacokinetics, one strategy is to package clusters of small AuNP cores within a larger biodegradable construct. Such nanomaterials may be fabricated at an overall size that preserves favorable biodistribution, but the use of small gold particles can accelerate degradation and excretion. This is because small hydrophilic AuNPs have the potential to be renally excreted[35–38] and retained particles may have improved deterioration due to their high surface-to-volume ratio.[30,39] Several such AuNP clusters have been reported, using a variety of complexing materials (e.g., polyphosphazene,[40,41] polylysine and silica,[42] amphiphilic block copolymers containing poly(ethylene glycol) and polylactic acid[43,44] or polycaprolactone,[45] liposomes,[46,47] and oligonucleotides[48]).

Recently, our group reported gold-loaded polymeric micelles consisting of 1.9-nm dodecanethiol-capped AuNPs encapsulated by poly(ethylene glycol)-*block*-poly(ε-caprolactone) (PEG-PCL), with tunable micelle diameters of 30-150 nm.[49,50] The use of hydrophobic AuNPs allowed facile particle synthesis through micelle self-assembly, and dense packing of substantial gold mass within the particle core. These particles showed excellent tumor accumulation, biocompatibility, CT contrast, and radiosensitization. The use of small AuNPs conferred significant improvements in bioelimination compared to large solid cores, with ~30% reduction in the liver from day 2 to day 7 post-injection. In

later studies using 0.9-nm AuNPs, this was further improved to ~40% reduction in the first week, and up to 65% over three months.[51] It was suspected that the residual biopersistence of gold resulted from incomplete dispersion of the hydrophobic particles.

To that end, we have developed a novel gold nanomaterial that transitions from hydrophobic to hydrophilic under acidic conditions (**Figure 2.1**). In particular, ultrasmall gold nanoparticles are coated with the pH-sensitive polymer, acetalated dextran.[52] The resulting particles can be encapsulated within the hydrophobic core of an amphiphilic diblock copolymer, forming a tightly-packed polymeric micelle. Upon exposure to low pH environments (e.g., the cellular lysosomal compartment), the pendent acetal groups on the acetated dextran undergo hydrolysis, leading to disruption of the micelle and an increase in AuNP hydrophilicity. These small, dispersed AuNPs have a greater capacity for degradation and excretion, allowing for faster and more extensive bioelimination.

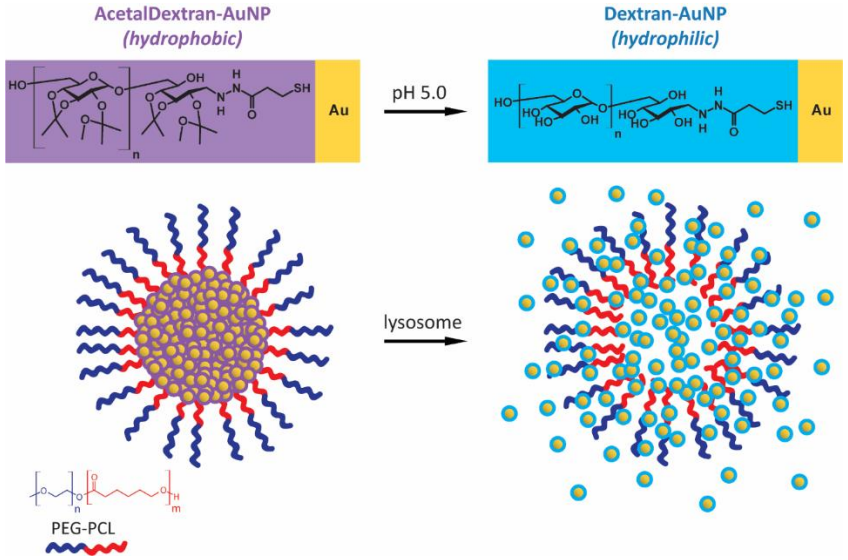

Figure 2.1. Schematic of AcetalDextran-AuNPs and AcetalDextran-AuNP-Micelles. Ultrasmall gold particles are coated with a hydrophobic pH-sensitive polymer, acetalated dextran; upon exposure to low pH environments, this hydrophobic coating becomes hydrophilic. Polymeric micelles encapsulating these

materials will be stable at standard physiological pH but will dissociate within the lysosome, allowing dispersion of soluble AuNPs.

2.3 Results and Discussion

A goal of this study was to produce dextran-coated gold nanoparticles that were smaller than the cutoff for renal clearance (estimated at 5-10 nm), which necessitated the production of even smaller AuNP cores (~2nm in diameter). To produce these AuNPs, a protocol was adapted from Jadzinsky et al[53] using *p*-mercaptobenzoic acid as the capping ligand; this reaction could be scaled to produce monodisperse 1.7-nm gold particles at yields of several hundred milligrams ("*p*MBA-AuNPs"; **Figure 2.2B**). These AuNPs were subsequently coated with a low-molecular-weight dextran (5 kDa) with a single terminal thiol group (**Figure 2.2A**).

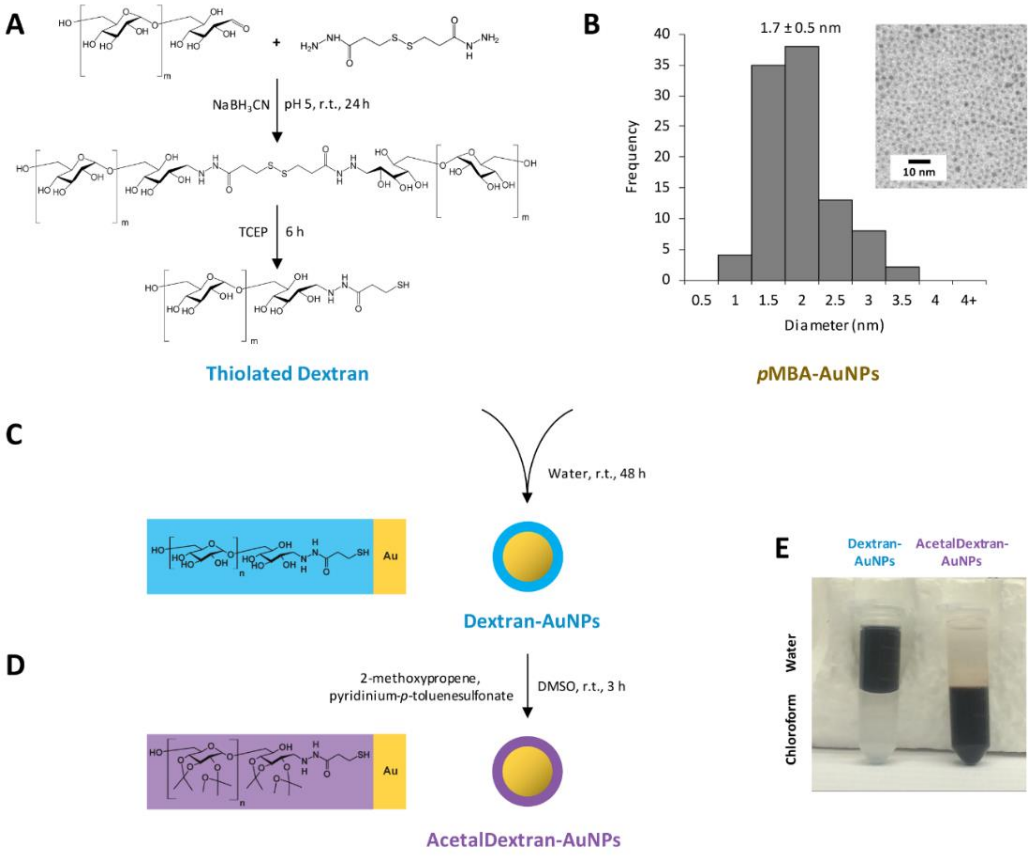

Figure 2.2. Synthesis of AcetalDextran-AuNPs. (A) Dextran (5 kDa) was combined with 3,3'-dithiobis(propanoic dihydrazide) to install a terminal thiol group. (B) Ultrasmall hydrophilic gold nanoparticles (AuNPs) were synthesized using *p*-mercaptobenzoic acid (*p*MBA) as a capping ligand; particles had a mean diameter of 1.7 ± 0.5 nm (SEM). Inset shows TEM image of dried particles. (C) *p*MBA-AuNPs were coated with thiolated dextran via ligand exchange, yielding Dextran-AuNPs. (D) Dextran-AuNPs were covalently modified with acetal groups, yielding AcetalDextran-AuNPs. (E) Demonstration of water-soluble Dextran-AuNPs vs. chloroform-soluble AcetalDextran-AuNPs.

Thiolated dextran was prepared by reductive amination of the terminal glucose moiety, which possesses a single transient aldehyde, with 3,3'-dithiobis(propanoic dihydrazide). 3,3'-dithiobis(propanoic dihydrazide) contains two terminal hydrazide groups and an internal disulfide. Hydrazide was chosen as the aldehyde linking group, as opposed to a primary amine, because it is generally resistant to acidic hydrolysis, especially when it is further stabilized by reduction with cyanoborohydride.[54,55] After conjugation of the dihydrazide with two dextran molecules, the disulfide was reduced with tris(2-carboxyethyl)phosphine (TCEP) to yield dextran-thiol, which was isolated by washing in 90% methanol. Notably, disulfides are generally capable of binding gold surfaces without prior reduction;[56,57] however, we found that the dextran disulfide dimer could not be efficiently conjugated with gold, presumably due to steric occlusion.

AuNPs were coated with dextran-thiol through simple ligand exchange in aqueous solution ("Dextran-AuNPs"; **Figure 2.2C,E**). The successful addition of dextran was confirmed by analyzing the mass percentage of gold in purified particles: *p*MBA-coated AuNPs were approximately 80% gold, but this dropped to 31% gold after the ligand exchange reaction, due to the larger size of dextran (**Table 2.1**). Dextran-AuNPs were also examined by dynamic light scattering, and their average peak hydrodynamic diameter was 7.3 nm, suggesting the possibility of renal filtration.

	% Au [w/w][a]	Core diameter[b]	Hydrodynamic diameter[c]	Solubility[d]	pH sensitivity[e]
***p*MBA-AuNPs**	79.3%	1.7 ± 0.5 nm	5.0 nm PDI: 0.251	Water	No
Dextran-AuNPs	31.0%	2.1 ± 0.5 nm	7.3 nm PDI: 0.246	Water, DMSO	No
AcetalDextran-AuNPs	13.8%	2.1 ± 0.6 nm	n/a	Acetone, Toluene, Chloroform	Yes
AcetalDectran-AuNP-Micelles	11.4%	111.1 ± 38 nm	146.0 nm PDI: 0.156	Water	Yes

Table 2.1. Physiochemical parameters for AcetalDextran-AuNP-Micelles and precursor gold nanoparticles. [a]Percent gold mass measured by ICP-OES. [b]Core diameters measured by transition electron microscopy, expressed as the average of 40-100 particle measurements, ± standard deviation. [c]Hydrodynamic diameters measured by dynamic light scattering, expressed as the mean intensity and polydispersity index averaged for three measurements (*p*MBA-AuNPs and Dextran-AuNPs, one batch; AcetalDextran-AuNP-Micelles, six batches). [d]Solubility is not comprehensive. [e]pH sensitivity refers to observed changes in particle solubility and sedimentation behavior after incubation at pH 5.0.

After conjugation of AuNPs with dextran, the hydroxyl groups on the dextran were covalently modified with pendant acetal groups (**Figure 2.2D,E**) to increase the hydrophobicity of the particles and enable their encapsulation within micelles. To append the acetal groups, Dextran-AuNPs were dissolved in dimethyl sulfoxide and then directly chemically reacted with 2-methoxypropene in the presence of the catalyst pyridinium-*p*-toluenesulfonate. The resulting particles, "AcetalDextran-AuNPs" (or "ADAs"), were no longer soluble in water; instead, they could be dissolved in nonpolar organic solvents such as chloroform and toluene. This, along with an additional decrease in particle gold mass percentage (**Table 2.1**), was indicative of a distinct compositional change from Dextran-AuNPs and strongly suggests the successful application of acetal groups.

The behavior of ADAs was characterized under acidic conditions to evaluate their ability to transition back to hydrophilic Dextran-AuNPs. A range of aqueous buffers representing various physiological compartments were tested: PBS, pH 7.4, for blood; PBS, pH 6.8, for hypoxic tumors; and 0.3 M acetate buffer, pH 5.0, for lysosomes. First, hydrophobic ADAs were suspended in each of these buffers, which initially formed a turbid suspension due to the insolubility of these particles (**Figure 2.3A,B**). After several hours of mixing at 37 °C, particles at pH 7.4 and 6.8 appeared to remain unchanged. However, at pH 5.0, particles became fully water-soluble over the course of 12 hours, as evidenced by a dramatic increase in solution transmittance from cloudy (7.4 %T) to clear (60.7 %T). To further confirm this behavior, we suspended AcetalDextran-AuNPs in serum at either pH 7.4 or pH 5.0 (**Figure 2.3C**). Initially, particles could be precipitated by centrifugation, which indicated insolubility due to their hydrophobic acetal coating. At later timepoints, particles at pH 5 lost this property and remained in solution even after high-speed centrifugation (16,000 x *g*, 10 min). This shift in solubility is consistent with the expected hydrolysis of the acetal groups at low pH.

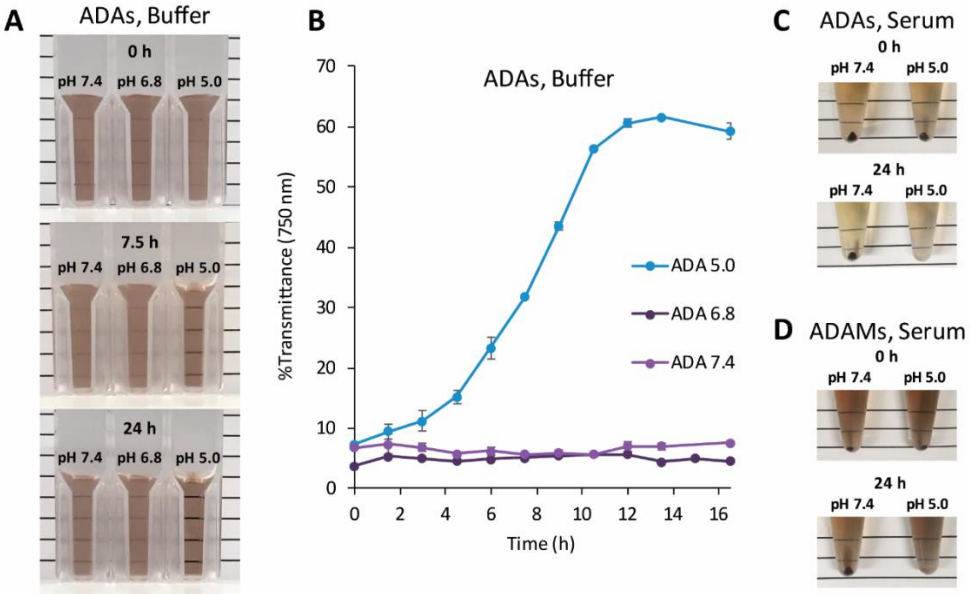

Figure 2.3. pH-dependent solubility of particles incubated at pH 7.4 (PBS), pH 6.8 (PBS), or pH 5.0 (0.3M acetate). (A) AcetalDextran-AuNPs (ADAs) were suspended in buffers (1.5 mg mL^{-1} by dry particle weight) and incubated at 37 °C under constant agitation for a total of 24 hours. Representative images shown. (B) Aliquots of AcetalDextran-AuNPs were removed and measured for absorbance at 750 nm; results expressed as percent transmittance, average of three measurements ± standard deviation. (C,D) AcetalDextran-AuNPs or AcetalDextran-AuNP-Micelles (ADAMs) were suspended in serum (0.04 mg mL^{-1} by Au, 1 mL) and incubated at 37 °C under constant agitation for a total of 24 hours. Particles were centrifuged at 16,000 x *g* for 10 minutes; separate tubes were prepared for each timepoint.

Next, the ADAs were encapsulated within polymeric micelles. As noted, we have previously reported encapsulation of hydrophobic AuNPs using the biodegradable amphiphilic block copolymer PEG-PCL.[49–51] Following a similar approach, "AcetalDextran-AuNP-Micelles" (or "ADAMs") were formed by simple mixing of PEG-PCL and gold particles in toluene, followed by emulsion in water and evaporation of toluene to drive micelle self-assembly (**Figure 2.4A**). Micelles were isolated by centrifugal sedimentation to yield 146-nm water-soluble particles (**Figure 2.4B**). Particle structure and size were confirmed by transition electron microscopy imaging (both standard- and Cryo-TEM) (**Figure 2.4C**). Micelles were observed to be stable in phosphate-buffered saline (PBS) at 4 °C for at least one week, as evidenced by consistent hydrodynamic diameter and EM structure (**Figure 2.4D**).

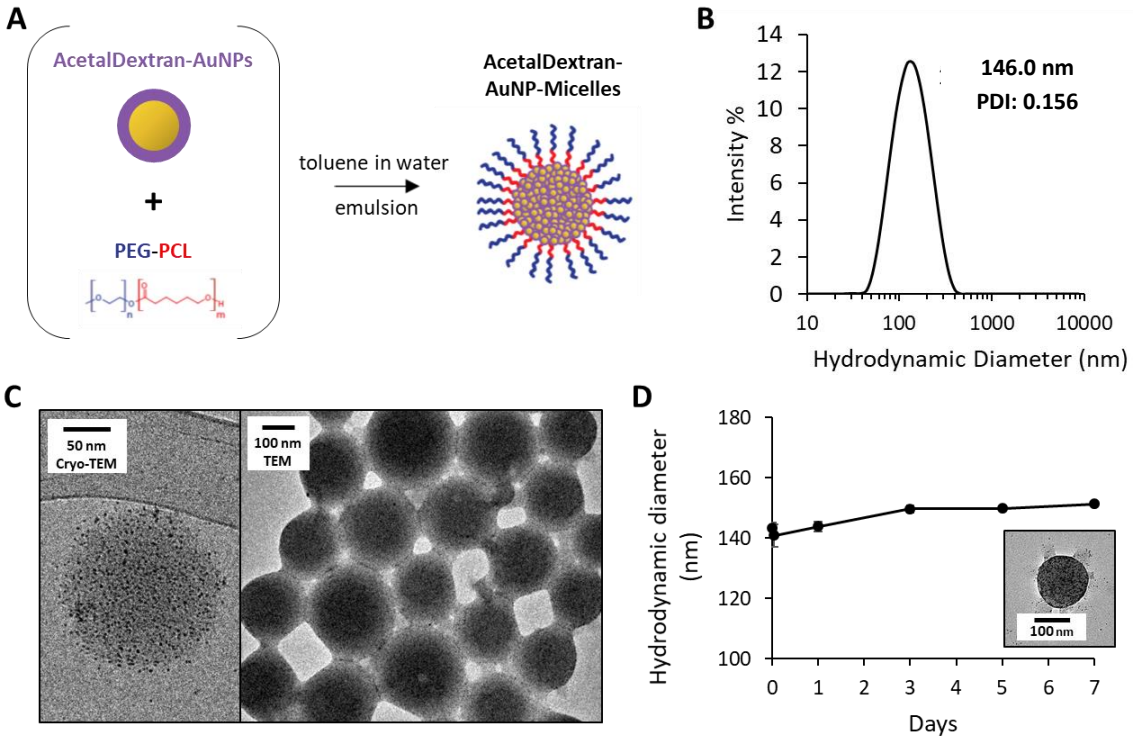

Figure 2.4. Formation of AcetalDextran-AuNP-Micelles. (A) AcetalDextran-AuNPs and PEG-PCL were dissolved in toluene and then suspended in water to form an emulsion, driving self-assembly of AcetalDextran-AuNP-Micelles. (B) Hydrodynamic diameter of micelles determined via dynamic light scattering. The average peak hydrodynamic diameter was 146 nm (average of six batches). (C) Electron microscopy imaging of micelles in water via Cryo-TEM and standard TEM. (D) Hydrodynamic diameter of micelles in PBS at 4 °C, recorded immediately after dissolution and at 1 hour, 1 day, 3 days, 5 days, and 7 days (average of three measurements, ± SEM). At 7 days, the sample was diluted 10-fold in water to reduce salt concentration and then imaged by TEM (inset).

To determine whether the ADAs could undergo a similar transition at pH 5 (i.e., going from hydrophobic to hydrophilic) after being encapsulated in micelles, ADAMs were dissolved in serum at either pH 7.4 or pH 5.0 (**Figure 2.3D**). Although the micelles were fully soluble due to their outermost layer of PEG, their heavy gold cores meant they could be pelleted out of solution by high-speed centrifugation (16,000 x *g*, 10 min). When the micelles were mixed at 37 °C for 24 hours, those kept at pH 7.4 continued to

display the same behavior, and could be pelleted. In contrast, those exposed to acidic conditions could no longer be sedimented at these centrifugation speeds. This suggests that the AuNPs no longer form a heavy gold core within the micelle and is consistent with our proposed model: the acidic environment leads to hydrolysis of the acetal groups, destabilization of the micelle core, and release of the Dextran-AuNPs. Importantly, this phenomenon can apparently occur without the need for degradation of the PEG-PCL, which is not expected to occur quickly under these conditions.[58]

We next examined the behavior of ADAMs in biological systems. Acetalated dextran has previously been proven to have toxicity comparable to that of poly(lactic-*co*-glycolic acid), an FDA-approved material; safety was confirmed in particle form and for the isolated breakdown products of acetal hydrolysis (i.e., acetone and methanol).[52] To confirm this behavior in the present formulation, ADAMs were incubated with an immortalized human liver cell line, HepG2, and a standard MTT assay was performed after 24 hours (**Figure 2.5A**). Cell viability of ~95% was seen up to at least 10 μg mL^{-1} gold, with no statistically significant decrease. Even at very high concentrations (80 μg mL^{-1} Au), cells preserved more than 80% viability compared to media-only controls, suggesting good biocompatibility.

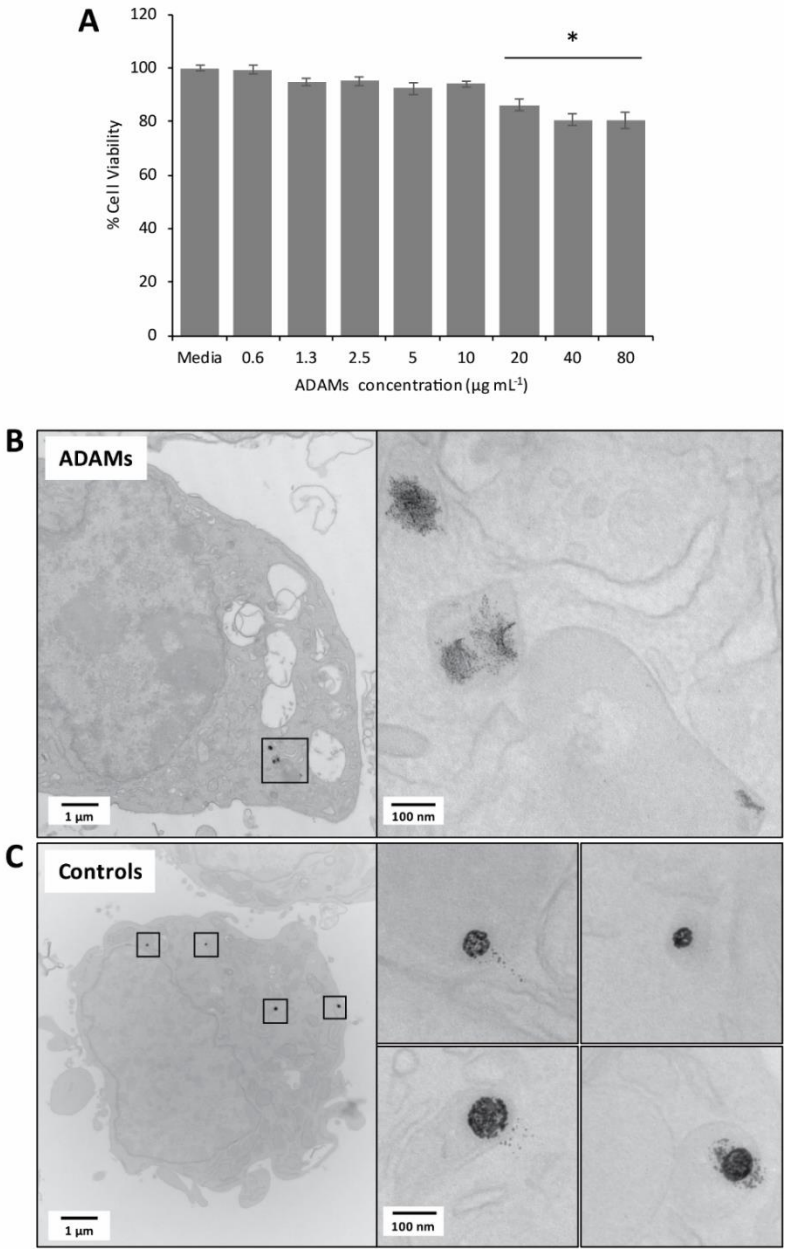

Figure 2.5. AcetalDextran-AuNP-Micelles (ADAMs) in cell culture. (A) ADAMs were incubated with HepG2 human liver cells at various concentrations (expressed as μg mL^{-1} Au) for 24 hours, and cytotoxicity was assessed by MTT assay. % Cell viability was calculated in relation to media-only controls; statistical comparison was performed using one-way ANOVA with post-hoc Tukey HSD test; *$p < 0.05$ relative to media controls. (B,C) ADAMs or control micelles (C_{12}-AuNP-Micelles) were incubated with RAW 264.7 murine macrophages at 10 μg mL^{-1}Au for 24 hours. Cells were fixed and imaged by electron microscopy. Single cell shown for each condition, with expanded images on left.

The biodegradation of ADAMS was also assessed in cell culture. As a control for these experiments, we prepared equivalent AuNP-loaded polymeric micelles that lacked pH sensitivity: 2-nm dodecanethiol-coated AuNPs ("C_{12}-AuNPs") formed into micelles using PEG-PCL ("C_{12}-AuNP-Micelles").[49] Each micelle formulation was incubated with RAW 264.7 murine macrophages for 24 hours at 10 µg mL^{-1} gold; cells were then fixed, embedded, and sectioned for TEM analysis (**Figure 2.5B,C**). AuNPs could be clearly visualized within unstained cells and were localized to vesicular compartments. The pH-sensitive ADAMs showed considerable breakdown of the spherical micelle structure and dispersion of individual AuNPs. In contrast, control C_{12}-AuNP-Micelles retained a distinctly spherical shape; although some separated AuNPs could be observed, the clear unidirectional distribution pattern strongly suggested that this was an artefact of the TEM tissue-sectioning process. At this 24-hour timepoint, both micelle formulations had equivalent accumulation of gold within (or associated with) cells (ADAMs: 10.7 $x10^{-9}$ µg per cell; C_{12}-AuNP-Micelles: 9.84 $x10^{-9}$ µg per cell).

Finally, the pharmacokinetics of ADAMs was evaluated. C57 black mice were injected intravenously with AcetalDex-AuNP-Micelles at a dose of 100 mg Au per kg body weight. To determine the circulation time of micelles in the bloodstream, blood samples were drawn at various timepoints post-injection and analyzed for gold content. Micelles displayed long circulation, with a half-life of approximately 3.5 hours (**Figure 2.6A**).

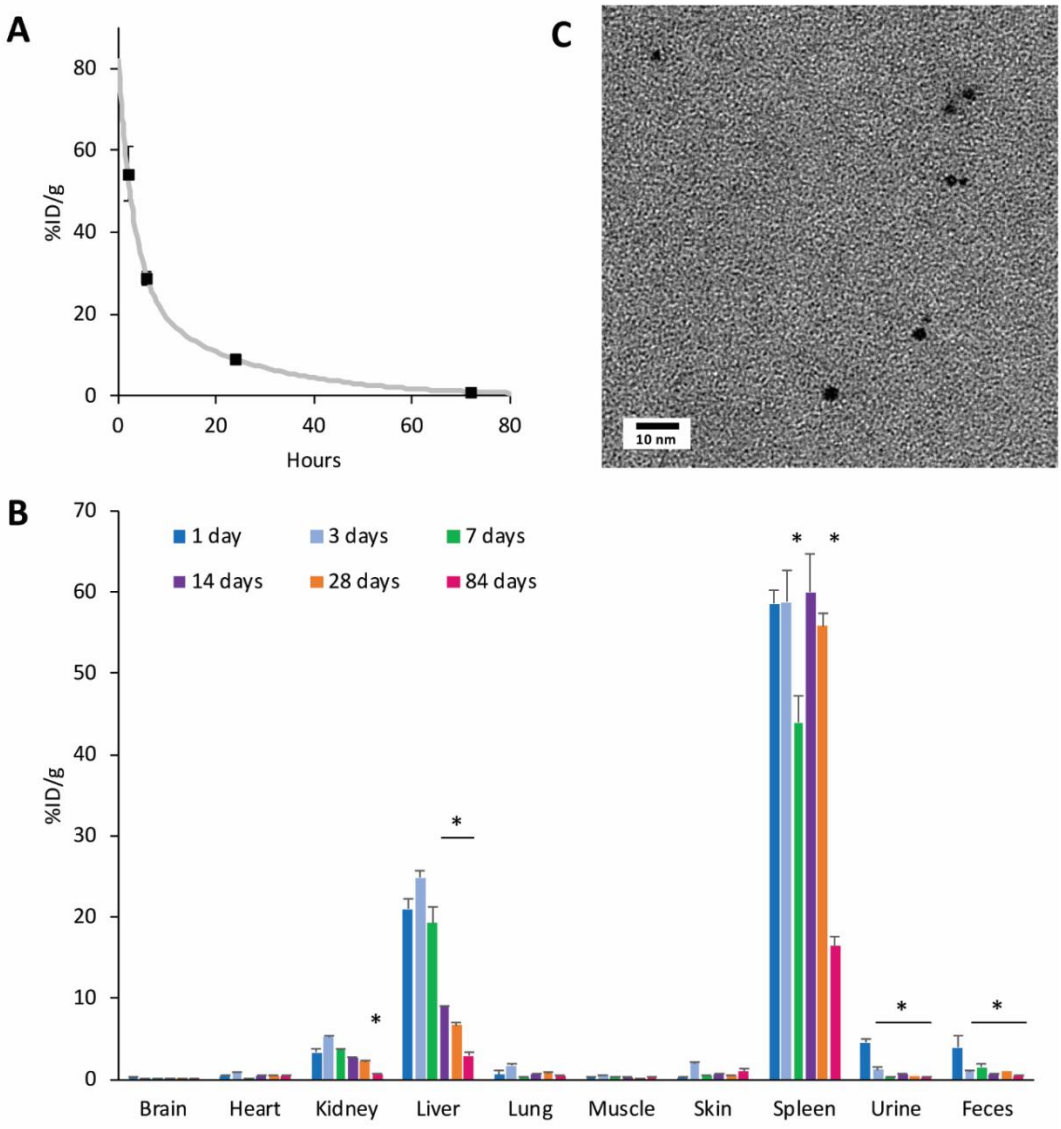

Figure 2.6. In vivo pharmacokinetics and biodistribution of AcetalDextran-AuNP-Micelles. Mice were injected intravenously with 100 mg Au per kg body weight, and samples were collected at various timepoints post-injection (n = 3 mice per timepoint, expressed as average ± SEM). (A) Blood samples were analyzed by ICP-OES to determine gold content; curve-fitting performed using MATLAB software. (B) Tissue and fluid samples were analyzed by ICP-OES to determine gold content (n = 3 mice per timepoint, expressed as average ± SEM.) Statistical comparison was performed using one-way ANOVA with post-hoc Tukey HSD test; *$p < 0.05$ relative to measurement at 1 day. (C) Urine was collected at 24 hours post-injection, diluted 1:1 in pure water, and imaged by electron microscopy. Electron-dense 2-nm particles are consistent with the appearance of Dextran-AuNPs.

A biodistribution analysis was performed by collecting organ samples at various timepoints for a total of twelve weeks and assessing tissue gold content using inductively-coupled plasma optical emission spectroscopy (ICP-OES) (**Figure 2.6B**). ADAMs displayed a tissue biodistribution pattern that is typical for nanoparticles of this size, with the majority of particles initially accumulating in the liver and spleen. However, we observed a substantial drop in gold levels in these organs over time. On average, liver gold decreased 86.1% over twelve weeks, while in the spleen it dropped 72% over that period. Liver clearance was also more rapid; levels began to decrease appreciably after the first week, while spleen levels remained high for the first four weeks. The mechanisms of micelle elimination were not examined in detail, but they likely involve endocytic uptake into cells, trafficking to lysosomes and other endosomal compartments, and exocytosis. In the liver, hepatocytes periodically exocytose their lysosomal contents into bile, where it is carried to the digestive tract and excreted in feces.[59–61] An appreciable amount of gold was detected in the feces, particularly at 1 day post-injection. This hepatobiliary excretion route may contribute to the faster elimination of gold from the liver vs. the spleen, where no equivalent system exists.

Notably, by ICP-OES analysis, elemental gold could also be detected in the urine at 24 hours post-injection (%ID/g tissue: 4.5 ± 0.5). We further explored this phenomenon by TEM imaging of urine samples (**Figure 2.6C**). We observed electron-dense 2-nm particles that were well-dispersed and consistent in appearance to *p*MBA-AuNPs and Dextran-AuNPs. These data confirm that intravenously injected AcetalDextran-AuNP-Micelles are capable of breaking down into renally excretable particles.

Throughout these studies, we examined mice for signs of drug-induced toxicity. Animals remained energetic and without visible signs of poor health (lethargy, noticeable changes in food intake, poor grooming, etc.). Injected animals displayed an initial transient drop in body weight (10%), which may have been caused in part by the stress-inducing effects of intravenous injection, repeated blood collection, and other handling procedures; this weight loss was resolved by day 4, and generally increased throughout the twelve-week study (**Figure 2.7A**). Knowing the potential for high liver accumulation of particles, serum was collected from mice at 1, 3, and 7 days post-injection and analyzed for elevated liver enzymes: alanine transaminase (ALT), aspartate transaminase (AST), and alkaline phosphatase (ALP) (**Figure 2.7B-D**). These levels were widely recorded to be within normal limits, with the single exception of increased AST at 1 day. Notably, these assays involve colorimetric detection of enzymes;[62] at the 1 day timepoint, serum contained a substantial volume of gold particles that imparted a noticeable brown hue, which may have impacted analysis. Finally, tissue samples were harvested from the kidney, liver, spleen, and lung at various timepoints post-injection (**Figure 2.7E**). Tissues were embedded with paraffin, stained with hematoxylin and eosin (H&E), and imaged by light microscopy. Liver glycogen depletion was observed at Day 1, consistent with transient animal fasting; this correlates with the weight loss seen at Day 1, and as noted, may arise partially from general animal handling stress. Histological examination revealed no signs of acute or chronic pathology (apoptosis, immune cell infiltration, damage to tissue architecture, etc.), with the exception of mild spleen inflammation at Day 1, which diminished at 1 week and resolved by 3 months.[63]

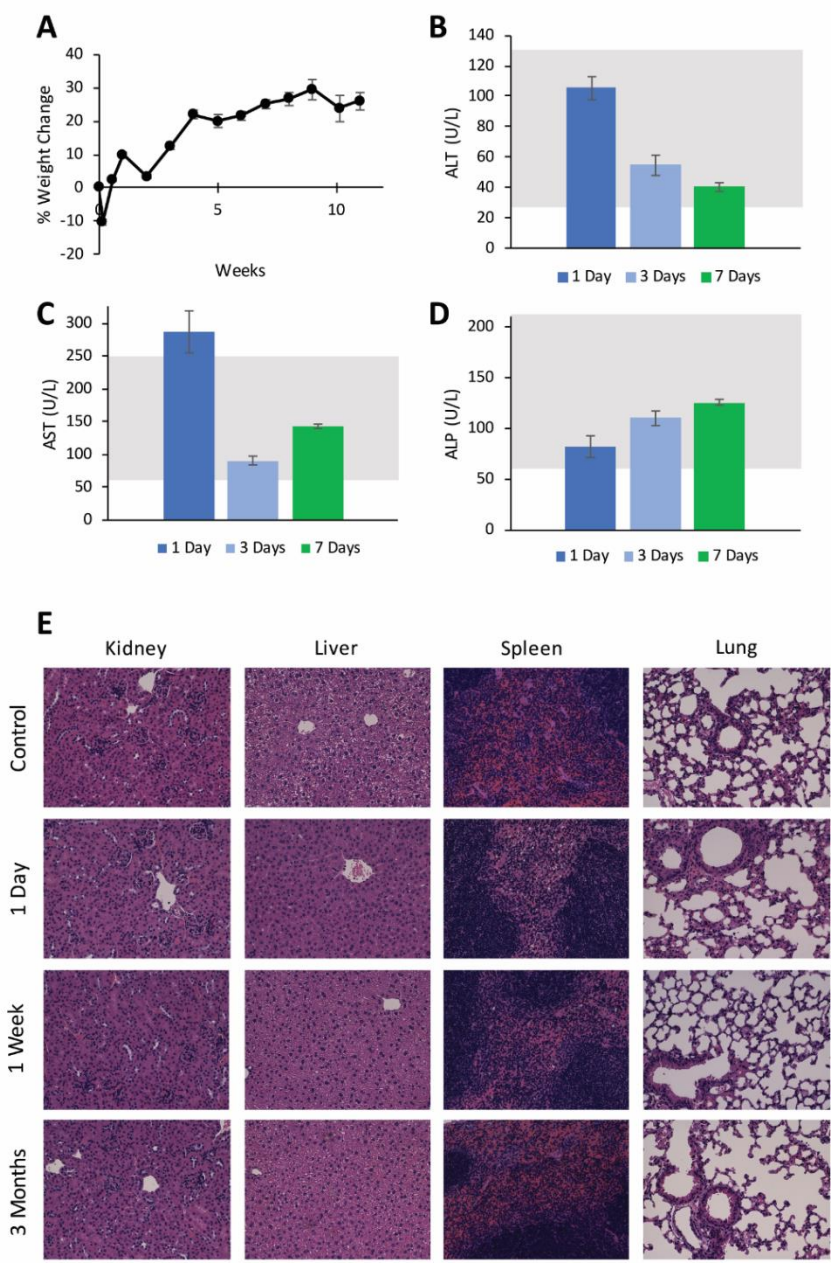

Figure 2.7. Safety profile of AcetalDextran-AuNP-Micelles after injection of 100 mg kg^{-1} Au. A) Percent change in mouse body weight over time, normalized to pre-injection weight. B-D) Serum measurements of alanine aminotransferase, aspartate aminotransferase, and alkaline phosphatase at various times post-injection. Gray shading represents standard clinical range for healthy mice. *n* = 3 mice per group, ± SEM. E) Representative histological images of mouse organ tissues at various timepoints post-injection. Tissues were paraffin-embedded and stained with H&E.

2.4 Conclusion

Considering the extent of global research interest in gold nanoparticles and their therapeutic potential, it is important to address the lingering question of their physiological persistence. The reported strategy seeks to improve clearance while still maintaining favorable aspects of gold particle design. This has been achieved by utilizing a pH-sensitive polymer, acetalated dextran, which transitions from hydrophobic to hydrophilic in acidic conditions. Acetalated dextran containing a single terminal thiol group has been installed onto ultrasmall AuNPs using newly-described synthetic strategies. Clusters of these particles could then be encapsulated within polymeric micelles of favorable size, with high stability at pH 7.4. However, both the hydrophobic AuNPs and their larger polymeric assemblies showed rapid degradation in acidic buffers (pH 5.0) and in macrophage cell culture. Micelles were found to have good biocompatibility and serum pharmacokinetics; furthermore, they displayed progressive long-term clearance from accumulated tissues, including the liver and spleen. Collectively, these environmentally-responsive materials present an intriguing and effective strategy for the biodegradation of gold nanostructures.

2.5 Experimental Section

Materials: Dextran (5 kDa, T5) was purchased from Phamacosmos. 3,3'-dithiobis(propanoic dihydrazide) was purchased from Frontier Scientific. Tris(2-carboxyethyl(phosphine) (TCEP), gold(III) chloride trihydrate, tetraoctylammonium bromide, 1-dodecanethiol, sodium borohydride, pyridinium-p-toluenesulfonate, and 2-methoxypropene were purchased from Sigma Aldrich. *p*-mercaptobenzoic acid (*p*MBA) was purchased from TCI America. Sodium cyanoborohydride, triethylamine, fetal bovine serum (FBS), Dulbecco's Modified Eagle Medium (DMEM), Trypsin-EDTA, and

penicillin–streptomycin solution were purchased from Thermo Fisher Scientific. Poly(ethylene glycol)$_{4000}$-*b*-poly(ε-caprolactone)$_{3000}$ (PEG-PCL) was purchased from Polymer Source. PBS (1X, pH 7.4) was purchased from Quality Biological. MTT assay kit was purchased from Roche Diagnostics GmbH. Isoflurane was purchased from Akorn Animal Health.

Synthesis of pMBA-AuNPs: Hydrophilic gold nanoparticles coated in *p*-mercaptobenzoic acid (*p*MBA) were prepared using a protocol modified from Jadzinsky et al.[53] Briefly, a stock solution of gold(III) chloride trihydrate (1 g mL^{-1}) was first centrifuged for 30 minutes at 16,000 x *g* to remove gold crystals, and then 400 µL was added to an acid-washed flask and diluted in water (158 mL). 184 mL methanol was then added under vigorous stirring. In parallel, *p*MBA was prepared as a 95 mM stock solution (726 mg in 50 mL) containing 300 mM sodium hydroxide (595 mg), and then combined with the primary gold solution. The resulting solution was allowed to equilibrate for 3-5 hours, until the color had changed from pale orange to nearly colorless. Next, a freshly-prepared 150 mM solution of sodium borohydride (159 mg in 28 mL water) was added to the reaction dropwise over the course of 15 minutes, resulting in a gradual color change to brown and then black over the course of 2 hours. The solution continued stirring overnight. Particles were then precipitated by adding methanol (467 mL) and an aqueous solution of sodium chloride (6.825 g in 47 mL) to the reaction mixture, then centrifuging at 3000 x *g* for 5 minutes. To wash particles, pellets were first suspended in 70% methanol (v/v) and centrifuged again; next, pellets were dissolved in water and rinsed repeatedly using centrifugal filters (10,000 MWCO, Amicon). Finally, particles were added to pre-weighed microcentrifuge tubes and then dried under centrifugal evaporation (Labconco).

Synthesis of thiolated dextran: Thiolated dextran was prepared by reductive amination.[55] Dextran (5 kDa; 14.163 g) and 3,3'-dithiobis(propanoic dihydrazide) (270 mg) were dissolved in 300 mL acetate buffer (0.3 M, pH 5). Sodium cyanoborohydride (approximately 2.6 g) was then added, and the reaction was allowed to stir for 24 hours. Next, a solution of TCEP (460 mg in 7 mL water) was brought to pH 5 using sodium hydroxide, then added to the primary reaction solution. After 6 hours stirring, thiolated dextran was purified as follows. First, the solvent was removed by lyophilization (Labconco) and the solid product was ground to a fine powder. Next, solids were washed four times by suspension in 90% methanol (v/v) followed by centrifugation; between washes, pellets were mechanically disturbed either by agitating with a spatula (after first two washes) or by drying the pellet under vacuum and re-pulverized (after the third wash). Finally, the product was dried under vacuum.

Synthesis of Dextran-AuNPs: *p*MBA-AuNPs were dissolved in aqueous solution at a concentration of approximately 2 mg mL^{-1} (by dry nanoparticle weight). Thiolated dextran was added at approximately 10x molar equivalents relative to the *p*MBA ligand (1 part *p*MBA AuNPs : 85 parts Dext-SH, w:w; calculated by approximating AuNP mass percentage at 25% *p*MBA, and approximating molecular weight of thiolated dextran at 5239 Da). The reaction was stirred for 48 hours, and then purified by repeated washing using centrifugal filters (30,000 MWCO). Finally, the resulting dextran-coated AuNPs were lyophilized.

Synthesis of AcetalDextran-AuNPs: Dextran-AuNPs were acetalated using a protocol adapted from Bachelder et al.[52] A 20-mL long-necked air-free flask was flame-dried

under vacuum and then charged with nitrogen. Meanwhile, Dextran-AuNPs (up to 500 mg) were dissolved in 10 mL anhydrous DMSO, then combined with 16 mg pyridinium-*p*-toluenesulfonate; this was transferred anaerobically to the reaction flask. 3.4 mL of 2-methoxypropene was then injected into the same flask, which was allowed to stir for 3 hours at room temperature under oxygen-free conditions. The reaction was quenched by addition of 1 mL triethylamine. To purify, the solution was diluted into 100 mL water, and approximately 10% volume was removed by rotary evaporation to ensure elimination of excess triethylamine. The solution was then centrifuged at 3000 x *g* to collect precipitates. Any solids that remained in the original reaction vessel or in the flask used for rotary evaporation were washed with water. Finally, all precipitates were dissolved in acetone, combined, transferred into pre-weighed microcentrifuge tubes, then dried under centrifugal evaporation.

Synthesis of AcetalDextran-AuNP-Micelles: A solution was prepared containing 80 mg mL^{-1} of Acetal-Dextran-AuNPs (by dry particle weight) and 40 mg mL^{-1} of poly(ethylene glycol)-*block*-poly(ε-caprolactone) (PEG_{4000}-PCL_{3000}). After thorough sonication, 100 µL of this solution was injected slowly into a glass scintillation vial containing 4 mL water under constant sonication (Branson, bath sonicator); sonication continued until a homogenous emulsion was formed. Vials were lightly capped and placed under vacuum overnight to remove toluene, allowing formation of stable micelles. Micelles were purified by centrifugation, first at 400 x *g* (10 minutes) to eliminate large precipitating aggregates and then at 16,000 x *g* (30 minutes) to sediment micelles. This precipitate was then collected and further concentrated using centrifugal filters (100,000 MWCO). Particles were then stored at 4°C, typically after suspending in PBS (by adding 10x concentrate).

Synthesis of C_{12}-AuNPs and C_{12}-AuNP-Micelles: Gold nanoparticles and gold-loaded polymeric micelles were synthesized as non-pH-sensitive experimental controls. Dodecanethiol-coated AuNPs (C_{12}-AuNPs) were synthesized using the Brust method,[64] as adapted by Higbee-Dempsey et al.[65] Dodecanethiol-coated AuNPs were then loaded into polymeric micelles using a protocol modified from by Al Zaki et al.[49,51] PEG-PCL (17 mg mL^{-1}) and dodecanethiol AuNPs (17.5 mg mL^{-1} by dry particle weight) were dissolved in a total of 200 µL toluene. This solution was sonicated and then injected into 4 mL water to form a homogenous emulsion. Purification then proceeded as described for AcetalDextran-AuNP-Micelles.

Particle characterization: Gold nanoparticles were characterized using a variety of physiochemical methods. Particles were imaged by electron microscopy using a Tecnai T12 microscope to determine gold diameter and overall particle morphology; size analysis was performed using ImageJ software. Hydrodynamic diameter and zeta potential were measured using a Zetasizer Nano ZS (Malvern Panalytical); data are generally expressed as the average of triplicate measurements of one synthetic batch; while data for AcetalDextran-AuNP-Micelles represent an average of six batches. Gold concentration was determined using inductively-coupled plasma optical emission spectroscopy (ICP-OES) on a Spectro Genesis. To prepare samples for ICP-OES, solutions were placed in borosilicate glass tubes containing up to 1 mL of freshly-prepared aqua regia (a 1:3 mixture of nitric acid and hydrochloric acid; e.g., 250 µL HNO_3 and 750 µL HCl); tubes were lightly sealed with PFTE-lined caps, allowed to stand for at least 20 minutes to ensure complete dissolution of gold, and then diluted in water up to a known volume.

Evaluation of acid-responsiveness: AcetalDextran-AuNPs were first dissolved in acetone and then diluted into buffered solutions at one of three pHs: pH 7.4 (PBS); pH 6.4 (PBS, titrated to 6.8 using 1 M sodium hydroxide); or pH 5.0 (acetate buffer, 0.3 M). All solutions consisted of 1.5 mg mL^{-1} AuNPs (by dry particle weight) and 2% acetone (v/v). Solutions were placed at 37 °C and agitated vigorously using an orbital shaker. Every 1.5 hours, triplicate aliquots were removed and analyzed. Absorbance was measured at 750 nm (Tecan) to determine solution turbidity, as calculated using the following equation:

$$\%\,\text{Transmittance} = \text{antilog}\,(2 - \text{absorbance}) \quad (1)$$

Samples were then diluted to a concentration of 1 mg mL^{-1} and photographed.

In separate experiments, AcetalDextran-AuNPs and AcetalDextran-AuNP-Micelles were examined in serum. First, fetal bovine serum was sterilely titrated to pH 5.0 using hydrochloric acid; this serum and unmodified serum were equilibrated at 4 °C overnight, and then centrifuged at 3000 x *g* for 30 minutes to remove any aggregated proteins. Gold particles were then sterilely dissolved in both serums at a concentration of 0.04 mg mL^{-1} by Au, and divided into two 1.5-mL sterile microfuge tubes per experimental group (1 mL each). One set of tubes were immediately centrifuged at 16,000 x *g* for 10 minutes, and pellets were photographed; the other set of tubes were incubated at 37°C for 24 hours under constant agitation, then similarly centrifuged and photographed.

Cell culture: RAW 264.7 and HepG2 cells were acquired from ATCC. Cells were grown at 37°C with 5% CO_2 in Dulbecco's Modified Eagle Medium (DMEM) supplemented with 10% fetal bovine serum and 1% pen strep. Cell passage numbers were kept low (< 10) to prevent genetic drift; during passage, RAW 264.7 cells were dissociated using cell scrapers, while HepG2 cells were dissociated with trypsin-EDTA.

Determination of cell viability: HepG2 human liver cancer cells were examined by MTT assay to determine cell viability. Cells were first seeded in a 96-well plate (1×10^5 cells per well). The following day, media was carefully removed by pipette and replaced with 100 µL fresh media containing AcetalDextran-AuNP-Micelles at concentrations ranging from 0 to 80 µg mL^{-1} (by Au concentration). Cells were incubated for 24 hours, after which the media was removed and wells were washed with 200 µL PBS. Finally, cells were given fresh media containing 3-(4,5-dimethylthiazol-2-yl)-2,5-diphenyltetrazolium bromide (MTT). The MTT assay then proceeded according to the manufacturer's instructions. Cell viability was normalized to untreated control cells, and all conditions were performed in triplicate wells.

Imaging cell uptake: To examine cellular uptake of AcetalDextran-AuNP-micelles, particles were incubated with RAW 264.7 mouse macrophages. Cells were first seeded in 6-well plates (2×10^6 cells per well, quadruplicate conditions). The following day, media was carefully removed by pipette and replaced with 1 mL fresh media containing micelles at a concentration of 10 µg Au per mL. In parallel control experiments, cells were treated with 10 µg/mL C_{12}-AuNP-Micelles. After 24-hours incubation, media was carefully collected by pipette and set aside; cells were then gently washed with 1 mL

PBS, which was also collected. An additional 1 mL PBS was then added, and adherent cells were gently harvested using cell scrapers.

Cells were then examined using several techniques. In one set of experiments, cells (3 wells each) were counted using a hemocytometer, transferred into pre-weighed centrifuge tubes, weighed again, and lyophilized until dry. Dry tubes were weighed a final time, and then solids were dissolved in 1 mL aqua regia and processed for ICP-OES analysis as described. Tube weights were used to calculate exact number and mass of cells.

In another set of experiments, washed cells (1 well each) were centrifuged at 500 x *g* for 5 minutes, and cell pellets were gently resuspended in 100 µL of fixative solution containing 2% glutaraldehyde and 2% paraformaldehyde (w/v). Cells were then prepared for EM imaging by the University of Pennsylvania Electron Microscopy Resource Lab, and imaged on a JEOL 1010 microscope.

Animal welfare statement: Female C57BL/6 mice (6-8 weeks old) were obtained from Charles River. All animals were housed and maintained according to procedures approved by the University of Pennsylvania Institutional Animal Care and Use Committee. Mice were fed nutritionally standard chow containing fenbendazole, with free access to food and water.

Biodistribution and safety of AcetalDextran-AuNP-Micelles: Mice were intravenously injected with AcetalDextran-AuN-Micelles at a concentration of 100 mg Au per kg body weight (*n* = 18 mice total). Blood samples were then collected from the opposite tail vein at the following timepoints: 2 hours, 6 hours, 24 hours, and 72 hours. At each timepoint, approximately 10-25 µL were removed from each of three mice, which were randomized

such that every mouse underwent no more than 3 blood draws in total. Whole blood samples were then analyzed by ICP-OES as described, by digestion in 1 mL aqua regia for a minimum of one hour. Half-life of gold in blood samples was determined by fitting a double exponential decay curve to the data using MATLAB software (Mathworks).

Mice were then sacrificed at various timepoints post-injection: 1 day, 3 days, 1 week, 2 weeks, 4 weeks, and 12 weeks (n = 3 mice per group). Prior to sacrifice, urine and feces samples (12-130 µL and 18-75 mg, respectively) were collected from lightly-scruffed mice. Mice were then anesthetized with isoflurane (3%, 1.5 L min^{-1} O_2), and a minimum of 500 µL blood was collected via cardiac puncture. Mice were euthanized by cervical dislocation, and the following organs were harvested: brain, heart, kidney, liver, lung, muscle, skin, and spleen. Organs were lightly rinsed in PBS immediately following extraction.

At days 1, 3, and 7, cardiac blood was centrifuged to collect serum and then analyzed for liver enzymes by the Penn Vet Clinical Pathology Diagnostic Lab. At day 1, urine (n = 1 mouse) was examined by TEM imaging; 5 µL of urine was diluted 1:1 with water and placed onto a TEM grid for 3 minutes, then grids were lightly blotted, allowed to air-dry, and imaged using a Tecnai T12 microscope.

Feces, urine, and organ samples were analyzed by ICP-OES as described, by digestion in 1 mL aqua regia for a minimum of 12 hours. Several tissue samples were reserved for histological evaluation at 1 day, 1 week, and 3 months: kidney (n = 3 per timepoint), liver (n = 3), spleen (n = 3), and lung (n = 1). Sections of these tissues were fixed in formalin; paraffin embedding was performed by the Penn Center for Musculoskeletal Disorders Histology Core, while sectioning and staining was performed by the Penn Vet Comparative Histology Core. All samples were then imaged using an EVOS light microscope and were examined for signs of pathology. At day 1, separate

liver tissue sections were also preserved for examination of ultrastructure by electron microscopy. These were suspended in 100 µL of fixative solution containing 2% glutaraldehyde and 2% paraformaldehyde (w/v), and prepared for EM imaging by the University of Pennsylvania Electron Microscopy Resource Lab; imaging was performed on a JEOL 1010 microscope.

Statistical analysis: Statistical analysis was performed using one-way ANOVA with post-hoc Tukey HSD test, using Astatsa online software (http://astatsa.com).

2.6 References

[1] Y.-C. Yeh, B. Creran, V. M. Rotello, *Nanoscale* **2012**, *4*, 1871–1880.

[2] S. Jain, D. G. Hirst, J. M. O'Sullivan, *Br J Radiol* **2012**, *85*, 101–113.

[3] N. Elahi, M. Kamali, M. H. Baghersad, *Talanta* **2018**, *184*, 537–556.

[4] D. R. Cooper, D. Bekah, J. L. Nadeau, *Front. Chem.* **2014**, *2*.

[5] K. Haume, S. Rosa, S. Grellet, M. A. Śmiałek, K. T. Butterworth, A. V. Solov'yov, K. M. Prise, J. Golding, N. J. Mason, *Cancer Nanotechnol* **2016**, *7*, DOI 10.1186/s12645-016-0021-x.

[6] M. Laprise-Pelletier, T. Simão, M.-A. Fortin, *Advanced Healthcare Materials* **2018**, *7*, 1701460.

[7] N. S. Abadeer, C. J. Murphy, *J. Phys. Chem. C* **2016**, *120*, 4691–4716.

[8] R. S. Riley, E. S. Day, *Wiley Interdisciplinary Reviews: Nanomedicine and Nanobiotechnology* **2017**, *9*, e1449.

[9] J. B. Vines, J.-H. Yoon, N.-E. Ryu, D.-J. Lim, H. Park, *Front. Chem.* **2019**, *7*, DOI 10.3389/fchem.2019.00167.

[10] D. Xi, S. Dong, X. Meng, Q. Lu, L. Meng, J. Ye, *RSC Adv.* **2012**, *2*, 12515–12524.

[11] T. Dreifuss, E. Barnoy, M. Motiei, R. Popovtzer, in *Design and Applications of Nanoparticles in Biomedical Imaging* (Eds.: J.W.M. Bulte, M.M.J. Modo), Springer International Publishing, Cham, **2017**, pp. 403–427.

[12] M. M. Mahan, A. L. Doiron, *J. Nanomater.* **2018**, *2018*, 5837276.

[13] W. Li, X. Chen, *Nanomedicine* **2015**, *10*, 299–320.

[14] Q. Fu, R. Zhu, J. Song, H. Yang, X. Chen, *Advanced Materials* **2019**, *31*, 1805875.

[15] Y. Li, Q. Wei, F. Ma, X. Li, F. Liu, M. Zhou, *Acta Pharmaceutica Sinica B* **2018**, *8*, 349–359.

[16] I. Fratoddi, I. Venditti, C. Cametti, M. V. Russo, *J. Mater. Chem. B* **2014**, *2*, 4204–4220.

[17] P. R. Chandran, R. T. Thomas, in *Nanotechnology Applications for Tissue Engineering* (Eds.: S. Thomas, Y. Grohens, N. Ninan), William Andrew Publishing, Oxford, **2015**, pp. 221–237.

[18] F.Y. Kong, J.W. Zhang, R.F. Li, Z.X. Wang, W.J. Wang, W. Wang, *Molecules* **2017**, *22*, 1445.

[19] J. Liu, M. Yu, C. Zhou, J. Zheng, *Materials Today* **2013**, *16*, 477–486.

[20] H. H. Gustafson, D. Holt-Casper, D. W. Grainger, H. Ghandehari, *Nano Today* **2015**, *10*, 487–510.

[21] A. Albanese, P. S. Tang, W. C. W. Chan, *Annu. Rev. Biomed. Eng.* **2012**, *14*, 1–16.

[22] Y. Matsumura, H. Maeda, *Cancer Res.* **1986**, *46*, 6387–6392.

[23] R. K. Jain, T. Stylianopoulos, *Nature Reviews Clinical Oncology* **2010**, *7*, 653–664.

[24] T. G. Schaaff, R. L. Whetten, *J. Phys. Chem. B* **1999**, *103*, 9394–9396.

[25] J. P. Wilcoxon, P. Provencio, *J. Phys. Chem. B* **2003**, *107*, 12949–12957.

[26] Y. Shichibu, Y. Negishi, H. Tsunoyama, M. Kanehara, T. Teranishi, T. Tsukuda, *Small* **2007**, *3*, 835–839.

[27] A. M. Nowicka, U. Hasse, M. Hermes, F. Scholz, *Angewandte Chemie International Edition* **2010**, *49*, 1061–1063.

[28] T.-H. Chen, C.-C. Nieh, Y.-C. Shih, C.-Y. Ke, W.-L. Tseng, *RSC Advances* **2015**, *5*, 45158–45164.

[29] S. C. Gad, K. L. Sharp, C. Montgomery, J. D. Payne, G. P. Goodrich, *Int J Toxicol* **2012**, *31*, 584–594.

[30] J. Kolosnjaj-Tabi, Y. Javed, L. Lartigue, J. Volatron, D. Elgrabli, I. Marangon, G. Pugliese, B. Caron, A. Figuerola, N. Luciani, et al., *ACS Nano* **2015**, *9*, 7925–7939.

[31] J. Kolosnjaj-Tabi, J. Volatron, F. Gazeau, in *Design and Applications of Nanoparticles in Biomedical Imaging* (Eds.: J.W.M. Bulte, M.M.J. Modo), Springer International Publishing, Cham, **2017**, pp. 9–41.

[32] E. Sadauskas, G. Danscher, M. Stoltenberg, U. Vogel, A. Larsen, H. Wallin, *Nanomedicine* **2009**, *5*, 162–169.

[33] H. A. Havel, *AAPS J* **2016**, *18*, 1351–1353.

[34] A. Radomska, J. Leszczyszyn, M. W. Radomski, *Adv Clin Exp Med* **2016**, *25*, 151–162.

[35] J. F. Hainfeld, D. N. Slatkin, T. M. Focella, H. M. Smilowitz, *BJR* **2006**, *79*, 248–253.

[36] W.-S. Cho, M. Cho, J. Jeong, M. Choi, B. S. Han, H.-S. Shin, J. Hong, B. H. Chung, J. Jeong, M.-H. Cho, *Toxicology and Applied Pharmacology* **2010**, *245*, 116–123.

[37] C. Zhou, M. Long, Y. Qin, X. Sun, J. Zheng, *Angewandte Chemie International Edition* **2011**, *50*, 3168–3172.

[38] F. Naz, V. Koul, A. Srivastava, Y. K. Gupta, A. K. Dinda, *Journal of Drug Targeting* **2016**, *24*, 720–729.

[39] U. Carlander, K. Midander, Y. S. Hedberg, G. Johanson, M. Bottai, H. L. Karlsson, *ACS Appl. Bio Mater.* **2019**, *2*, 1006–1016.

[40] R. Cheheltani, R. M. Ezzibdeh, P. Chhour, K. Pulaparthi, J. Kim, M. Jurcova, J. C. Hsu, C. Blundell, H. I. Litt, V. A. Ferrari, et al., *Biomaterials* **2016**, *102*, 87–97.

[41] M. Bouché, M. Pühringer, A. Iturmendi, A. Amirshaghaghi, A. Tsourkas, I. Teasdale, D. P. Cormode, *ACS Appl. Mater. Interfaces* **2019**, *11*, 28648–28656.

[42] D. Cassano, M. Summa, S. Pocoví-Martínez, A.-K. Mapanao, T. Catelani, R. Bertorelli, V. Voliani, *Particle & Particle Systems Characterization* **2019**, *36*, 1800464.

[43] J. M. Tam, J. O. Tam, A. Murthy, D. R. Ingram, L. L. Ma, K. Travis, K. P. Johnston, K. V. Sokolov, *ACS Nano* **2010**, *4*, 2178–2184.

[44] J. M. Tam, A. K. Murthy, D. R. Ingram, R. Nguyen, K. V. Sokolov, K. P. Johnston, *Langmuir* **2010**, *26*, 8988-99.

[45] P. Huang, J. Lin, W. Li, P. Rong, Z. Wang, S. Wang, X. Wang, X. Sun, M. Aronova, G. Niu, et al., *Angew Chem Int Ed Engl* **2013**, *52*, 13958–13964.

[46] T. S. Troutman, J. K. Barton, M. Romanowski, *Advanced Materials* **2008**, *20*, 2604–2608.

[47] A. K. Rengan, A. B. Bukhari, A. Pradhan, R. Malhotra, R. Banerjee, R. Srivastava, A. De, *Nano Lett.* **2015**, *15*, 842–848.

[48] L. Y. T. Chou, K. Zagorovsky, W. C. W. Chan, *Nature Nanotechnology* **2014**, *9*, 148–155.

[49] A. Al Zaki, D. Joh, Z. Cheng, A. L. B. De Barros, G. Kao, J. Dorsey, A. Tsourkas, *ACS Nano* **2014**, *8*, 104–112.

[50] C. McQuade, A. A. Zaki, Y. Desai, M. Vido, T. Sakhuja, Z. Cheng, R. J. Hickey, D. Joh, S.-J. Park, G. Kao, et al., *Small* **2015**, *11*, 834–843.

[51] A. A. Zaki, J. Z. Hui, E. Higbee, A. Tsourkas, *J Biomed Nanotechnol* **2015**, *11*, 1836–1846.

[52] E. M. Bachelder, T. T. Beaudette, K. E. Broaders, J. Dashe, J. M. J. Fréchet, *J. Am. Chem. Soc.* **2008**, *130*, 10494–10495.

[53] P. D. Jadzinsky, G. Calero, C. J. Ackerson, D. A. Bushnell, R. D. Kornberg, *Science* **2007**, *318*, 430–433.

[54] J. P. O'Donnell, *Drug Metabolism Reviews* **1982**, *13*, 123-59.

[55] G. Hermanson, *Bioconjugate Techniques*, Elsevier, **1996**.

[56] H. Grönbeck, A. Curioni, W. Andreoni, *J. Am. Chem. Soc.* **2000**, *122*, 3839–3842.

[57] J. C. Love, L. A. Estroff, J. K. Kriebel, R. G. Nuzzo, G. M. Whitesides, *Chem. Rev.* **2005**, *105*, 1103–1170.

[58] A. R. Hernández, O. C. Contreras, J. C. Acevedo, L. G. N. Moreno, *American Journal of Polymer Science* **2013**, *3*, 70–75.

[59] G. Renaud, R. L. Hamilton, R. J. Havel, *Hepatology* **1989**, *9*, 380–392.

[60] Y.-N. Zhang, W. Poon, A. J. Tavares, I. D. McGilvray, W. C. W. Chan, *Journal of Controlled Release* **2016**, *240*, 332–348.

[61] H. Wang, C. A. Thorling, X. Liang, K. R. Bridle, J. E. Grice, Y. Zhu, D. H. G. Crawford, Z. P. Xu, X. Liu, M. S. Roberts, *J. Mater. Chem. B* **2015**, *3*, 939–958.

[62] X.J. Huang, Y.-K. Choi, H.-S. Im, O. Yarimaga, E. Yoon, H.-S. Kim, *Sensors (Basel)* **2006**, *6*, 756–782.

[63] K. E. Ibrahim, M. G. Al-Mutary, A. O. Bakhiet, H. A. Khan, *Molecules* **2018**, *23*, E1848.

[64] M. Brust, M. Walker, D. Bethell, D. J. Schiffrin, R. Whyman, *Journal of the Chemical Society, Chemical Communications* **1994**, *0*, 801–802.

[65] E. Higbee-Dempsey, A. Amirshaghaghi, M. J. Case, J. Miller, T. M. Busch, A. Tsourkas, *Advanced Therapeutics* **2019**, *0*, 1900088.

CHAPTER 3: INDOCYANINE GREEN-COATED GOLD NANOCLUSTERS FOR PHOTOACOUSTIC IMAGING AND PHOTOTHERMAL THERAPY

3.1 Abstract

Traditional oncology treatment modalities are often associated with a poor therapeutic index. This has driven the development of new targeted treatment modalities, including several based on the conversion of optical light into heat energy (photothermal therapy, PTT) and sound waves (photoacoustic imaging, PA) that can be applied locally. These approaches are especially effective when combined with photoactive nanoparticles that preferentially accumulate in tissues of interest and thereby further increase spatiotemporal resolution. In this study, two clinically-used materials that have proven effective in both PTT and PA – indocyanine green and gold nanoparticles – were combined into a single nanoformulation. These particles, "ICG-AuNP clusters", incorporated high concentrations of both moieties without the need for additional stabilizing or solubilizing reagents. The clusters demonstrated high theranostic efficacy both in vitro and in vivo, compared with ICG alone. Specifically, in an orthotopic mouse model of triple-negative breast cancer, ICG-AuNP clusters could be injected intravenously, imaged in the tumor by PA, and then combined with near-infrared laser irradiation to successfully thermally ablate tumors and prolong animal survival. Altogether, this novel nanomaterial demonstrates excellent therapeutic potential for integrated treatment and imaging.

3.2 Introduction

Radiation therapy has long represented a paradigm in the treatment of cancer, with multiple advantages including efficacy against many tumor types and localized delivery.[1–3] Traditional radiation therapy involves the use of high-energy ionizing radiation – typically photons or charged particles – that relies on the inherent absorptive properties of that tissue to deposit energy. However, this broad cytotoxicity may contribute to inadvertent damage of adjacent healthy cells, particularly tissue in the path of radiation. Ionizing radiation is also a critical component of computed tomography (CT) and other imaging modalities used to clinically visualize malignant tissue; though dosage is usually low, these procedures may themselves pose risks to normal biological tissue.[4]

A new class of therapies and diagnostics have emerged that harness lower-energy forms of radiation, including infrared and visible light.[5–9] While less harmful to tissues on their own, these can be applied in combination with localized exogenous agents that mediate and enhance tissue interactions, thereby achieving site-specific efficacy with reduced damage to off-target tissues. In particular, near infrared light (NIR, 650 – 1350 nm) is a highly attractive radiation source primarily due to its relatively deep tissue penetration – up to several centimeters – compared to lower-wavelength light.[10,11] NIR photomedicine has been broadly applied in cancer treatment and imaging through numerous modalities,[8] including: photodynamic therapy, or PDT (light excites a photoactive agent to a triplet excited state, which then directly or indirectly generates free radicals and/or reactive oxygen species); photothermal therapy, or PTT (absorbed energy is emitted as vibrational energy – i.e., heat); fluorescence imaging (energy is emitted radiatively as a photon); and photoacoustic imaging (energy is emitted as heat, which generates a detectable acoustic wave). Photoacoustic imaging has become

increasingly popular due to its deep signal penetration (≤ 5-6 cm), high resolution (≥ 5μm), and decreasing instrument costs.[12–16] Furthermore, because the molecular contrast agents for photoacoustic imaging are optimized for non-radiative emission, many of these same materials can be utilized for photothermal therapy, allowing dual clinical functionality.[9] PTT has a potential advantage over photodynamic therapy, in that it does not require the presence of oxygen, the concentration of which may be limited in large solid tumors.[17]

To take advantage of photomedicine's increased safety margin, it is necessary for a photoactive moiety to be localized to the tumor tissue; however, this can be difficult to achieve for many traditional small molecule agents. Nanoscale formulations may be particularly useful for overcoming these targeting limitations. Due to their unique physical, chemical, and biological properties, nanoparticles can: 1) deliver high volumes of cargo to regions of interest, 2) maintain cargo in a desired site at an optimal time period for clinical intervention, and 3) reduce cargo accumulation in off-target sites.[18] An excellent candidate for nanoformulation – with great potential in both PTT and photoacoustic imaging – is indocyanine green (ICG), which at present is the only FDA-approved near-infrared dye.[19,20] As a small molecule, ICG's utility is limited because of its instability in aqueous solution – especially when combined with light, heat, or salts – as well as its rapid clearance from the bloodstream, which can prevent the high, localized concentrations desirable for intervention in tumors. While these shortcomings would likely improve in a nanoformulation, ICG can be difficult to load in large quantities due to its amphiphilicity and lack of easily-modifiable chemical groups.

Recently, we reported several novel fluorophore-based nanoparticle structures wherein a dye – ICG, protoporphyrin IX, or chlorin e6 – was combined with only one

other common component: superparamagnetic iron oxide nanoparticles (SPIOs).[21–23] In these three structures, the amphiphilic dye molecules were utilized as an outer coating to stabilize clusters of hydrophobic SPIO particles, thereby thermodynamically driving ICG to remain bound in large concentrations. The ICG-SPIO nanoclusters were successfully employed in image-guided surgery based on photoacoustic imaging (of ICG) and pre-surgical MR imaging (of SPIOs). However, in all of these studies, SPIOs were utilized for MR imaging and as a scaffold for the amphiphilic dye, but were not designed to contribute directly to tumor therapy.

With this in mind, we sought to further expand the utility of ICG clusters by creating an inherently theranostic nanoformulation for combined photoacoustic imaging and photothermal therapy, whereby both materials were capable of contributing to each modality. For this, we selected another material that has been proven dually efficacious in both photothermal therapy and photoacoustic imaging: gold nanoparticles (AuNPs).[5,13,16,24,25] Several groups have reported physiological studies of particles combining ICG and gold, but these particles have several key drawbacks. For example, they incorporated significant quantities of inert binding materials (serum albumin,[26,27] silica,[28–31] poly(styrene-*alt*-maleic anhydride),[32] polyethyleneimine,[32,33] chitosan[27,34], and poly(lactic-*co*-glycolic acid[27]), thereby reducing the per-particle loading of functionally active ICG and Au. Also, almost all of these studies used large gold particles (15 - 150 nm), which are well-known to display protracted physiological elimination.[35,36] We have previously demonstrated the utility of using 2-nm dodecanethiol-coated AuNPs in micellar nanoformulations: they can be densely packed to provide high Au payloads with extremely low non-gold mass, while their small individual size facilitates long-term physiological clearance.[37,38] In the current study,

ICG was successfully formulated at high concentrations into a stable nanoformulation with ultrasmall hydrophobic AuNPs. These dual-component nanoclusters show favorable long-term biological clearance, as well as great promise for both photoacoustic imaging and photothermal therapy.

3.3 Results and Discussion

Preparation and Characterization of ICG-AuNP Clusters

ICG and gold were formulated into a stable, water-soluble nanomaterial using a rapid and facile nanoemulsion methodology (**Figure 3.1A**). We first synthesized ultrasmall hydrophobic gold nanoparticles (AuNPs) consisting of 2-nm gold cores coated with dodecanethiol (**Figure 3.2A,B**).[39] Small clusters of AuNPs were then solubilized by using ICG as an amphiphilic coating. To prepare these clusters, ICG was combined with AuNPs in organic solvent and then emulsified into water, driving self-assembly of the two materials into discrete spheroids (**Figure 3.1B,C**). TEM images confirmed the expected clusters of ultrasmall AuNPs. ICG is not visible in such images, preventing observation of ICG location; however, we consistently observed that clusters in close proximity display a thick “halo” that could be indicative of ICG presence on the surface (**Figure 3.1B**, inset). Clusters exhibited a favorable hydrodynamic size and narrow size distribution (61.22 ± 2.63 nm); this diameter stayed constant over time, suggesting that clusters remain stable in water without detectable aggregation (**Figure 3.1D**). Due to the inclusion of ICG, clusters were found to be highly negatively-charged, with a zeta potential of –26.1 ± 12.6.

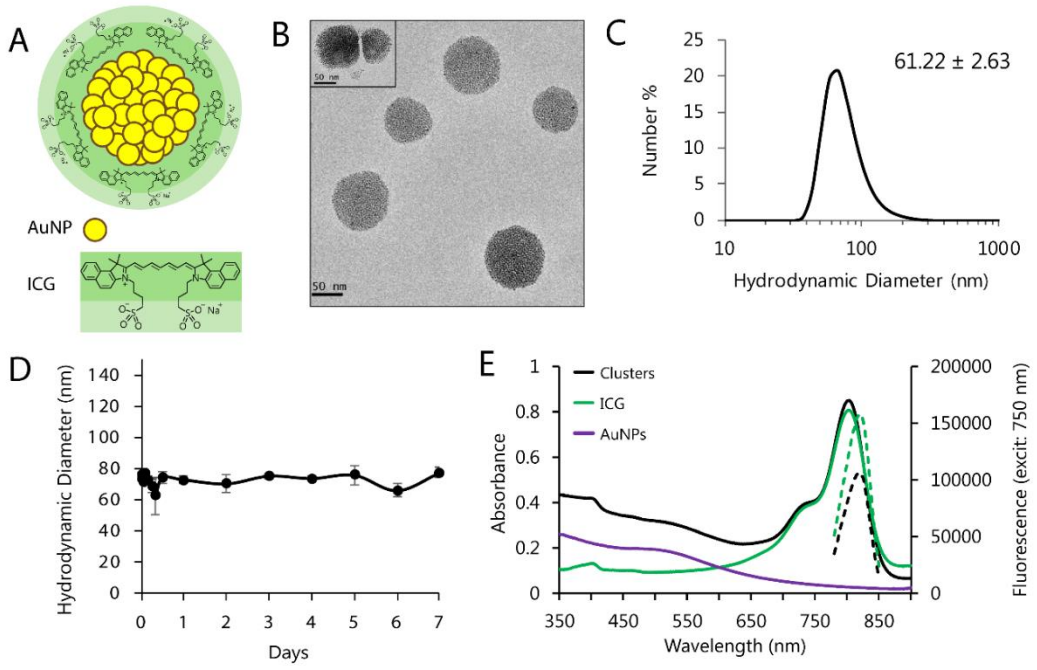

Figure 3.1. (A) Schematic of ICG-AuNP clusters, consisting of 2-nm dodecanethiol-coated gold nanoparticles (AuNP) packed within the core and coated with a dense outer layer of indocyanine green (ICG). (B) TEM images of clusters. (C) DLS of clusters in water showing hydrodynamic diameter; the average hydrodynamic diameter was 61.22 ± 2.63 nm (standard deviation, *n* = 2 particle batches). (D) Peak hydrodynamic diameter of clusters in solution (water, 4°C, dark) over the course of one week. *n* = 3 measurements, ± SEM. (E) Absorbance (solid lines) and fluorescence (dashed lines) of clusters dissolved in serum vs. equivalent concentrations of free ICG (3 μg mL^{-1} ICG) or dodecanethiol AuNPs (20 μg mL^{-1} Au). Cluster absorbance maximum = 803 nm; fluorescence maximum = 820 nm.

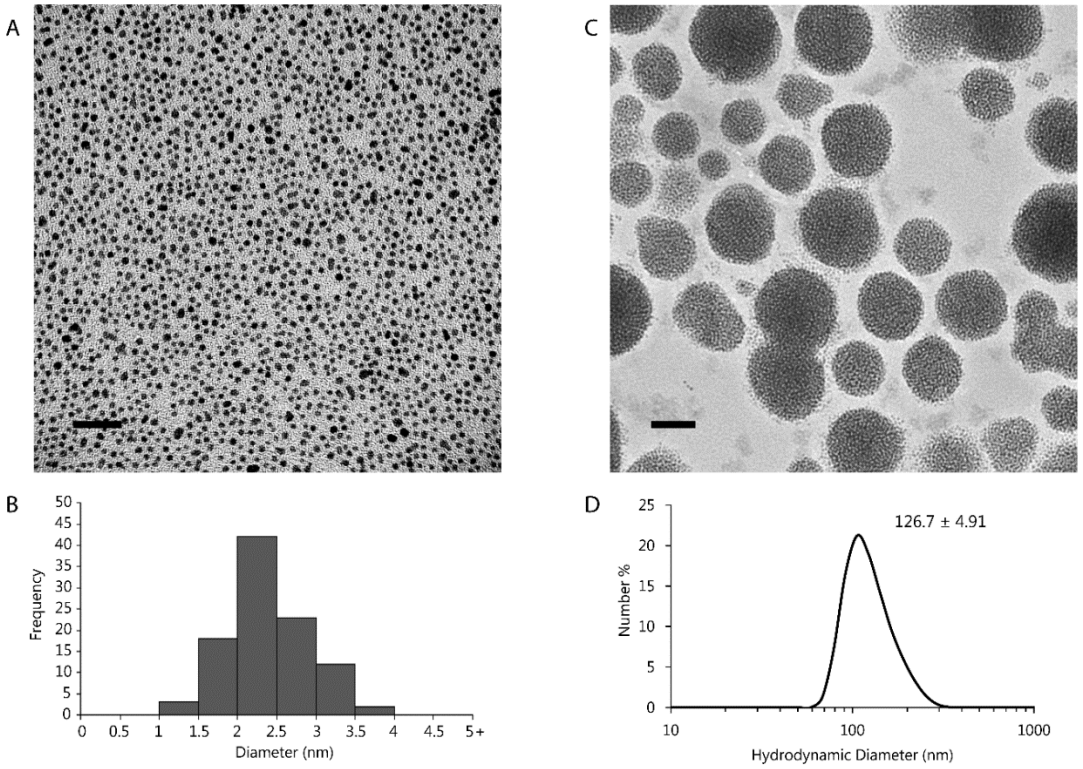

Figure 3.2. Dodecanethiol-coated gold nanoparticles (AuNPs). (A) Electron micrograph of AuNPs (scale bar = 20 nm). (B) Size distribution of AuNPs, determined by measuring the diameter of 100 individual particles. The average diameter was 2.42 ± 0.5 nm (standard deviation). (C) Electron micrograph of polymer-AuNP clusters (scale bar = 50 nm). (D) Size distribution of polymer-AuNP clusters, measured by dynamic light scattering (± standard deviation, *n* = 3 measurements).

We then sought to further understand the interaction between ICG and AuNPs within the cluster, and assess whether ICG might displace dodecanethiol on the AuNP surface. Knowing that ICG, but not dodecanethiol, is soluble in dimethylformamide, we dissolved ICG-AuNP clusters in this medium and centrifuged to separate out any insoluble material. The precipitate was found to be soluble only in highly nonpolar solvents such as toluene and the absorbance spectra matched that of AuNPs, but not ICG. In contrast, the absorbance spectra of the supernatant matched that of ICG, but

not AuNPs. There was no mixing of spectral signals (**Figure 3.3C**). This suggests that ICG is not covalently associated with the AuNP surface, and cluster assembly is likely the result of noncovalent interactions such as hydrophobic self-assembly. We also examined the clusters' optical properties in aqueous solutions (**Figure 3.1E; Figure 3.3A,B**). Interestingly, the peak associated with clustered AuNPs demonstrated only a very modest red-shift compared to the dispersed 2-nm AuNPs, despite the well-studied impact of AuNP aggregation on surface plasmon resonance.[40] To confirm this effect, we synthesized control AuNP clusters that are encapsulated with an amphiphilic polymer, poly(ethylene glycol)-b-poly(ε-caprolactone) (PEG-PCL), instead of ICG.[37] These polymer-AuNP clusters, which shared a similar size and structure as ICG-AuNP clusters (**Figure 3.2C,D**), displayed an equivalent absorbance peak, suggesting this is a shared feature of these nanostructures. When examining cluster absorbance peaks, we also found that ICG demonstrated strong quenching when incorporated into this cluster formulation, as observed by a reduction in fluorescence compared to equivalent concentrations of free ICG. This likely results from a combination of mechanisms, including self-quenching of ICG as a result of its tight packing on the surface of the clusters, and quenching due to the close proximity of ICG to the AuNPs, as gold is known to be an extremely effective quencher.[41,42]

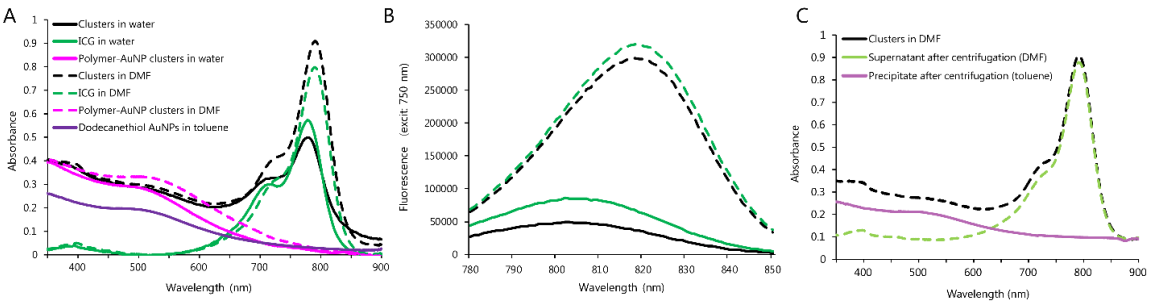

Figure 3.3. (A) and (B) Absorbance and fluorescence spectra, respectively, of ICG-AuNP clusters (3 μg mL^{-1} ICG, 20 μg mL^{-1} Au) and equivalent concentrations of free ICG, dodecanethiol AuNPs, and polymer-AuNP clusters. Separate spectra were collected in water, dimethylformamide (DMF), and toluene. (C) ICG-AuNP clusters (3.4 μg mL^{-1}, 23 μg mL^{-1} Au), dissolved in DMF and then centrifuged; the precipitate was then dissolved in an equivalent volume of toluene.

In order to optimize cluster composition and yield, we synthesized a number of different formulations of clusters by varying the relative amounts of ICG and AuNPs (**Figure 3.4; Table 3.1**). As expected, increasing the concentration of AuNPs relative to ICG resulted in more of the reagent ICG being successfully incorporated within clusters, maxing out at approximately 70% ICG encapsulation efficiency. Within the column-purified clusters, the ratio of ICG to Au was quite consistent across all nanoformulations tested, with ICG mass approximately 5-10% compared to gold mass. We also observed that using a larger initial ratio of AuNPs caused a moderate increase in cluster size, despite the consistent proportions of ICG and Au. Ultimately, we determined that the optimal cluster composition consisted of 2:16 ICG:AuNP (w/w) loading; this yielded efficient incorporation of ICG relative to starting material, high loading of ICG relative to Au, and favorable hydrodynamic diameter.

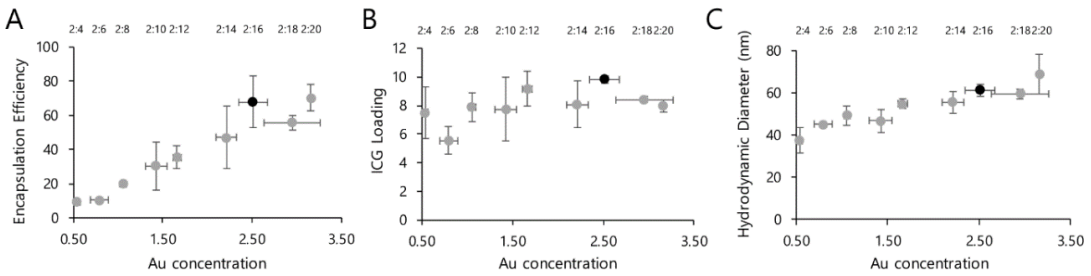

Figure 3.4. Multiple cluster formulations were synthesized by varying the ratio of ICG to AuNPs. ICG concentration was determined by absorbance, following dissolution in organic solvent; Au concentration was determined by ICP-OES. Black marker indicates the formulation selected for all other experiments. (A) Encapsulation efficiency of ICG into particles, which was calculated by dividing the ICG:Au ratios of the reaction solutions after vs. before column purification (expressed as percentage). (B) Loading efficiency of ICG within the purified particles, as calculated by the ICG concentration divided by Au concentration (expressed as percentage). (C) Hydrodynamic diameter of the particles. *n* = 2 particle batches, ± SEM.

mg ICG: mg AuNPs	Encapsulation Efficiency (%)	ICG Loading (%)	Hydrodynamic Diameter	PDI [a]
2:4	9.24 ± 1.19	7.52 ± 1.78	37.42 ± *5.98*	0.138
2:6	10.61 ± *0.36*	5.56 ± 1.00	45.02 ± *0.04*	0.116
2:8	19.92 ± *1.30*	7.91 ± 1.00	49.31 ± *4.36*	0.133
2:10	30.49 ± 14.16	7.74 ± 2.20	46.69 ± *5.54*	0.138
2:12	35.53 ± *6.45*	9.16 ± 1.21	54.81 ± *2.25*	0.148
2:14	47.18 ± 18.11	8.09 ± 1.61	55.65 ± *5.09*	0.144
2:16	**67.83 ± 15.21**	**9.82 ± 0.28**	**61.22 ± *2.63***	**0.138**
2:18	55.70 ± *4.08*	8.41 ± 0.24	59.98 ± *2.33*	0.124
2:20	70.19 ± *7.72*	7.97 ± 0.44	68.92 ± *9.29*	0.149

Table 3.1. Summary of **Figure 2**. Multiple cluster formulations were synthesized by varying the ratio of ICG to AuNPs. Encapsulation efficiency of ICG was calculated by dividing the ICG:Au ratios of the reaction solutions before vs. after column purification (expressed as percentage). ICG loading was calculated by the ICG concentration divided by Au concentration (expressed as percentage). Hydrodynamic diameter is

expressed in nanometers. Bolded text indicates the formulation selected for all subsequent experiments (2:16). *n* = 2 particle batches, ± SEM.

In Vitro Imaging of ICG-AuNP Clusters

Aqueous solutions of clusters and free ICG were prepared in a range of concentrations that were loaded simultaneously into imaging phantoms. We found that clusters displayed intensity-dependent signal for both fluorescence imaging and photoacoustic imaging (**Figure 3.5**). Notably, clusters demonstrated strong quenching of fluorescence signal compared to free ICG; in contrast, photoacoustic signal intensity was amplified in the nanoformulation, particularly at lower concentrations. These complimentary phenomena can likely be explained by the tight packing of ICG and Au within the cluster structure: close molecular proximity promotes collisional/self-quenching, decreasing the proportion of energy emitted radiatively (as fluorescence) and increasing nonradiative emission (heat, read as ultrasonic emissions).[42–44] We also collected photoacoustic spectra for polymer-AuNP clusters, knowing that many Au nanoformulations generate photoacoustic signals.[5,13,16,24] These spectra suggest that the polymer-AuNP cluster is only able to generate a modest photoacoustic signal intensity within the NIR range, with decreasing intensity at longer wavelengths. This corresponds with our data showing that ICG-AuNP clusters have similar PA spectra compared to free ICG, with only a slight increase in signal due to the presence of the AuNPs.

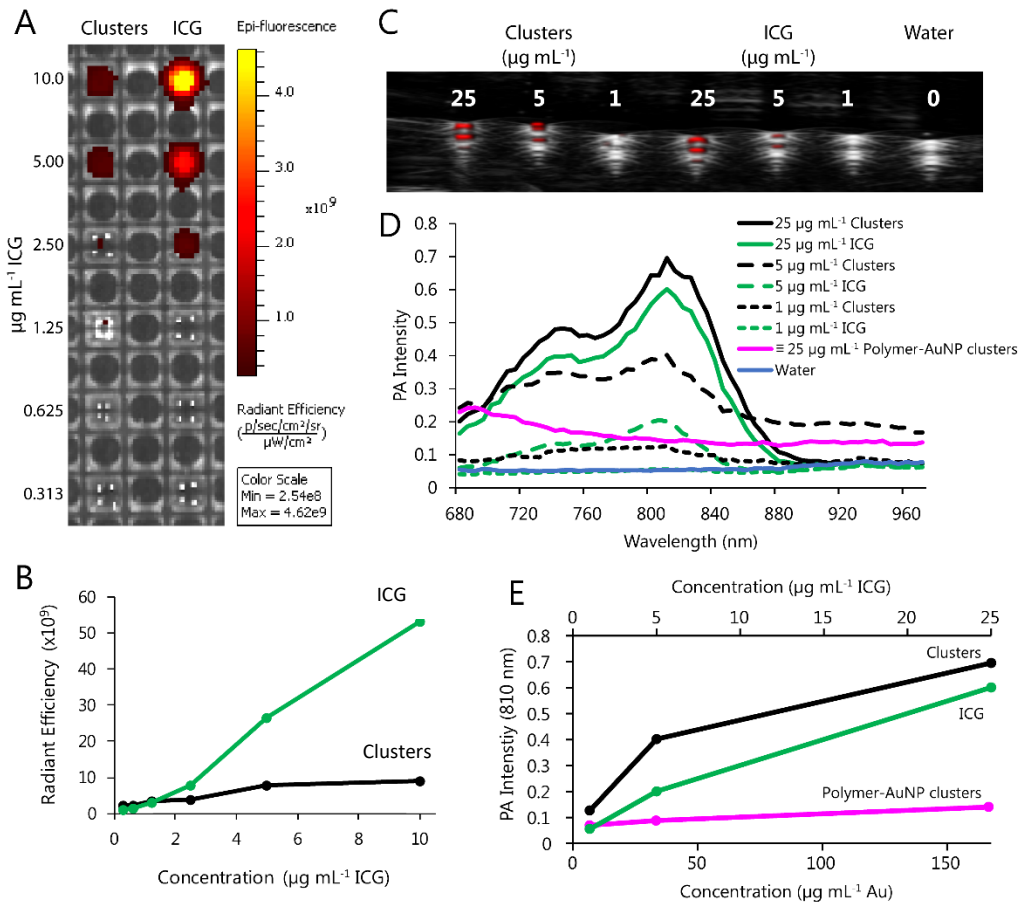

Figure 3.5. Phantom imaging of ICG-AuNP clusters in water vs. equivalent concentrations of free ICG and polymer-AuNP clusters. (A) Fluorescence imaging (ex = 745, em = 820). (B) Quantification of fluorescence signal intensity (radiant efficiency) as a function of ICG concentration. (C) Photoacoustic imaging (PA gain 30-40 dB, priority 95%, distance 12 mm from the transducer; transducer axial resolution, 75 μm; broadband frequency, 13-24 MHz). (D) Complete PA spectra at varying concentrations. ICG-AuNP clusters and free ICG are expressed as μg mL^{-1} ICG; polymer-AuNP clusters are shown at a gold dosage equivalent to that of the 25 μg mL^{-1} ICG-Au clusters (167 μg mL^{-1} Au). (E) Quantification of PA signal intensity (810 nm) as a function of concentration, compared to cluster concentration of ICG (shown) or Au (equivalent).

In Vitro Heating and ROS Generation of ICG-AuNP Clusters

Next, we examined the ability of clusters to generate heat upon irradiation. Solutions of clusters in water and control solutions were treated with 808nm laser light

(1.2 W power, 0.1 cm^2 area), and temperature was recorded over time. Clusters were found to generate significant temperature increases, higher than that of free ICG at every concentration tested (**Figure 3.6A**). When solutions were irradiated in multiple successive rounds, free ICG showed rapid degradation of its heating capacity, while clusters showed repeated heating ability through multiple laser administrations (**Figure 3.6C**). Clusters were also dissolved in serum containing biologically-relevant concentrations of hemoglobin, to compare their heating capacity relative to biological chromophores (**Figure 3.6B**). Even at low cluster concentrations, clusters showed significant and additive heating compared to hemoglobin alone, suggesting an appropriate safety window could be attained in vivo.

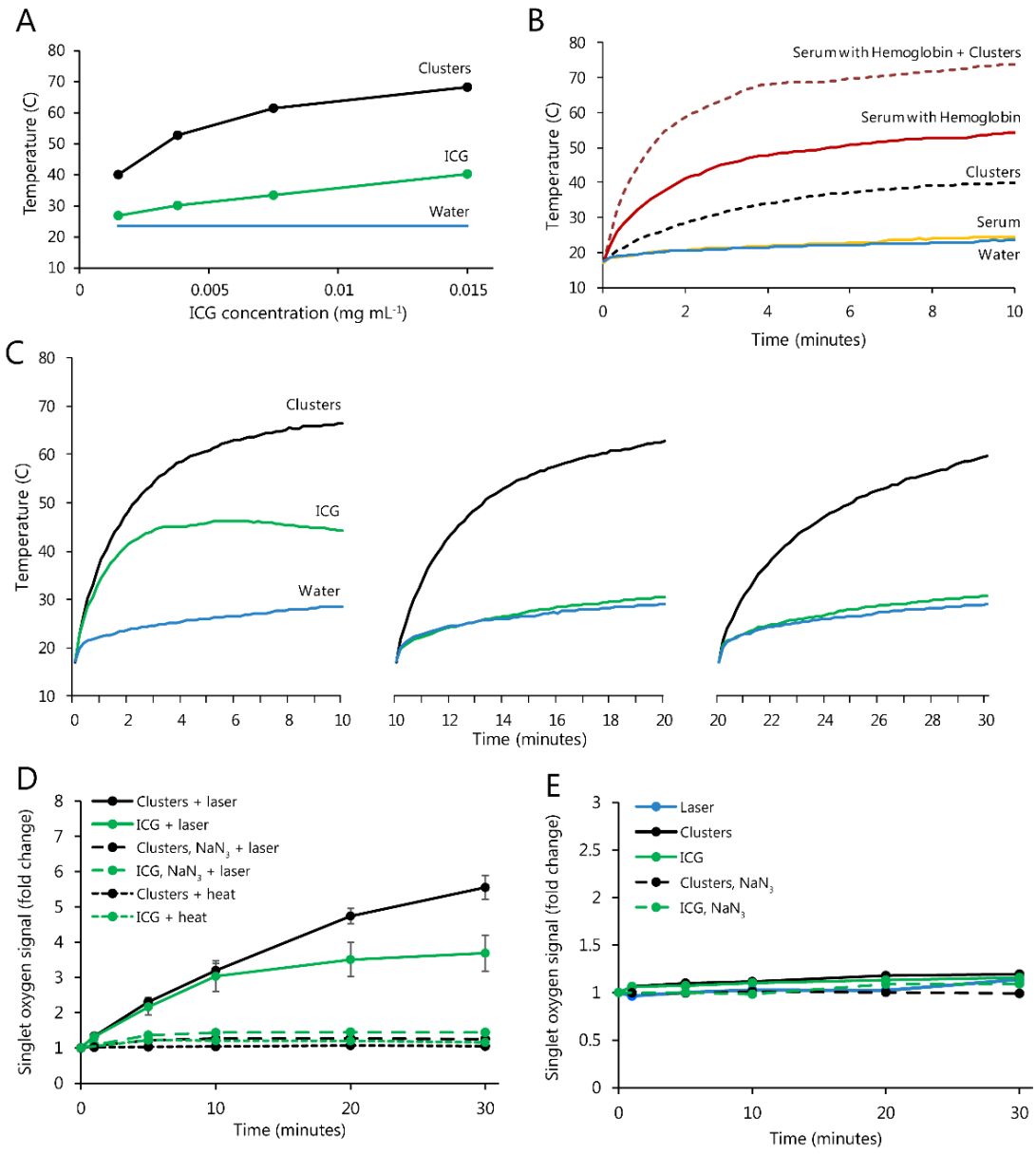

Figure 3.6. Solutions of ICG-AuNP clusters, free ICG, and various controls were prepared at room temperature and then irradiated at 808nm (1.2 W power, 0.1 cm^2 area) continuously for 10-30 minutes. (A) Solutions in water; final solution temperature is plotted. (B) The temperature of water; fetal bovine serum; clusters (0.0015 mg mL^{-1} ICG) in water; hemoglobin (155 mg mL^{-1}) in fetal bovine serum; and clusters and hemoglobin dissolved in serum at noted concentrations and heated for the indicated times. (C) Solutions in water (0.015 mg mL^{-1} ICG), heated in multiple 10-minute increments and allowed to cool to room temperature between successive rounds. (D) and (E) Clusters and free ICG (0.015 mg mL^{-1}) were irradiated

in the presence of Singlet Oxygen Sensor Green, which detects formation of reactive oxygen species. Controls included the following: samples containing sodium azide (10 mM), a known scavenger of singlet oxygen; and non-irradiated samples heated to equivalent temperatures by external heat application.

ICG nanoformulations have been well studied both in photothermal therapy and in photodynamic therapy, with many reports of dual activity for a single particle.[26,27,32,34] To this end, ICG-AuNP clusters were also examined for their ability to produce reactive oxygen species (ROS), which was monitored using the fluorescent reporter dye Singlet Oxygen Sensor Green (SOSG) **(Figure 3.6D,E**). Irradiated clusters demonstrated a strong time-dependent increase in SOSG signal. As observed in thermal studies, clusters and free ICG showed similar activity during the initial moments of irradiation, but free ICG appeared to exhaust its capacity more quickly. Further experiments confirmed that the SOSG fluorescence signal was unchanged in the absence of irradiation, even when equivalent levels of heat were applied directly to the solution. Moreover, we found that the SOSG signal was strongly reduced in the presence of sodium azide (10 mM), which is a known scavenger of singlet oxygen. Altogether, this provides strong evidence that ICG-AuNP clusters can generate ROS and provide a combination of photodynamic and photothermal therapy.

Cell Cytotoxicity of ICG-AuNP Clusters

After thorough physiochemical characterization of ICG-AuNP clusters in nonbiological conditions, clusters were next examined for cytotoxicity in cell culture. For these studies, we selected mouse 4T1 mammary carcinoma cells as a clinically relevant model of highly-aggressive, triple negative breast cancer.[45] Cells were incubated with increasing concentrations of clusters and free ICG, after which cellular viability was quantified by MTT assay (**Figure 3.7**). No toxicity was observed under standard dark

conditions, as evidenced by > 95% cell viability compared to media-only controls, even up to the highest concentration tested (10 µg mL^{-1} ICG). However, in parallel experiments, cluster treatment was combined with laser irradiation (0.2 W cm^{-2}, 7 minutes); under these conditions, cytotoxicity dropped sharply at a cluster concentration of 10 µg mL^{-1}, resulting in nearly complete loss of cell viability (reduced to 5%). Furthermore, this effect did not extend to free ICG, which showed only a moderate decrease in viability (down to 69%). These results suggest that ICG-AuNP clusters would be both well-tolerated systemically and highly effective at killing laser-targeted tissues.

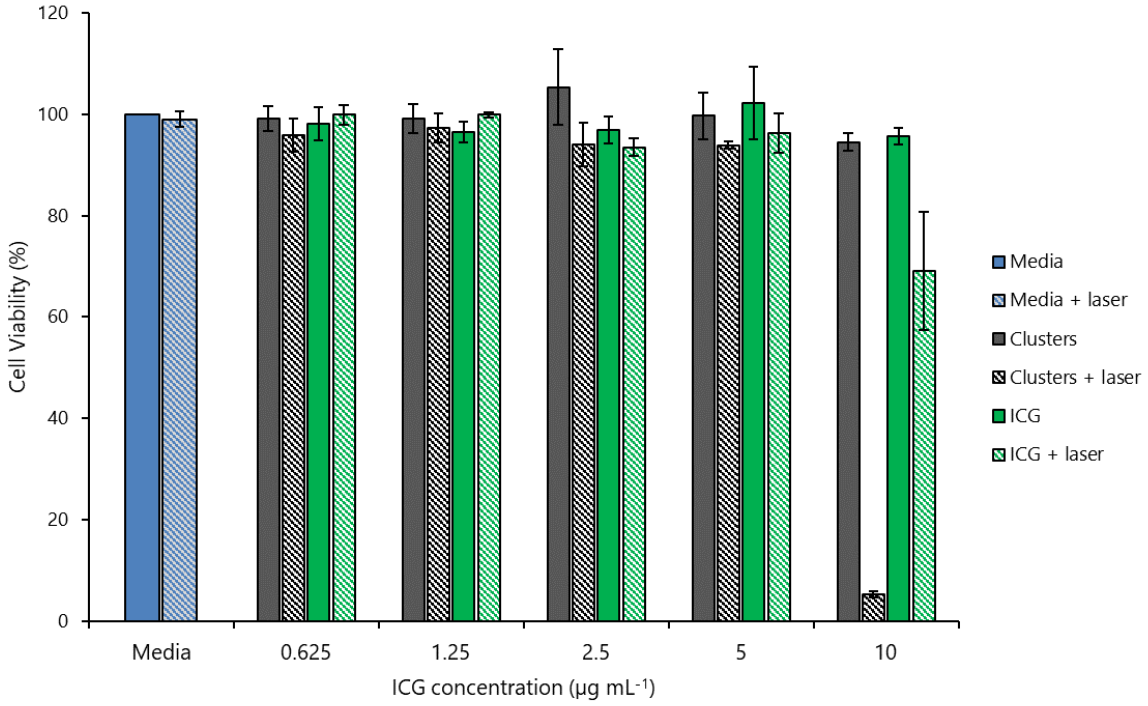

Figure 3.7. MTT assay of 4T1 cells incubated with ICG-AuNP clusters, free ICG, or standard media for 24 hours. A subset of cells was irradiated at 808 nm (0.2 W cm^{-2}) for the first 7 minutes. *n* = 3 wells, ± SEM.

In Vivo Biodistribution and Toxicity of ICG-AuNP Clusters

We next sought to understand how ICG-AuNP clusters would behave in vivo under non-treatment conditions. First, we administered clusters to healthy mice (30 mg kg^{-1} Au, 4.5 mg kg^{-1} ICG, I.V.) and measured gold content in the blood beginning at 5 minutes post-injection and lasting through the first 24 hours (**Figure 3.8A**). Clusters showed an approximate blood half-life of 61 minutes; for comparison, non-nanoparticle ICG has been previously reported to have a blood half-life of approximately 3 min.[46]

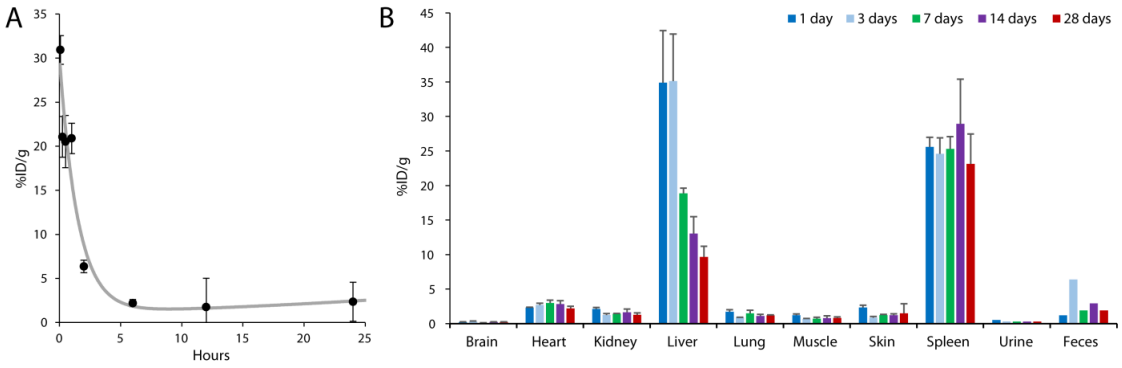

Figure 3.8. ICG-AuNP clusters (30 mg kg^{-1} Au, 4.5 mg kg^{-1} ICG, I.V.) were administered to naïve C57BL/6 mice and biodistribution was determined in key tissue compartments by ICP-OES analysis of gold. Results expressed as percent injected dose per gram tissue. (A) Blood pharmacokinetics for the first 24 hours post-injection. (B) Tissue biodistribution for the first 28 days post-injection. *n* = 3 mice per timepoint, ± SEM; urine and feces represent one sample each, pooled from three mice.

Next, we examined long-term biodistribution by measuring gold content in tissues (**Figure 3.8B**). Clusters displayed a tissue biodistribution pattern that is typical for gold nanoformulations, with high accumulation in the liver (34.8 ± 13 %ID g^{-1}, day 1) and spleen (25.6 ± 2.4 %ID g^{-1}, day 1). Gold accumulation was low (< 3 %ID g^{-1}) in all other analyzed tissues, including brain, heart, kidney, and lung, and remained low over the

course of the four-week study. Although elimination from the spleen remained protracted, we found that the levels of gold in the liver decreased steadily, dropping over 3.5-fold over time. These results can likely be attributed to the particle design -- specifically, that the incorporated gold comprises clusters of discrete ultrasmall AuNPs rather than a large, solid core. Notably, during this time period, gold could be detected in the feces, suggesting that elimination occurred through the hepatobiliary system.

Throughout this study, we examined several broad markers of toxicity. Animals displayed no signs of illness, distress, or other behavioral alterations. Animal body weight showed a small, insignificant decrease in the first several days, likely due to the effects of injection and blood collection, but recovered fully over the course of four weeks (**Figure 3.9A**). We also evaluated histology of key organs – liver, spleen, and kidney – but found no evidence of pathology (**Figure 3.9B**).

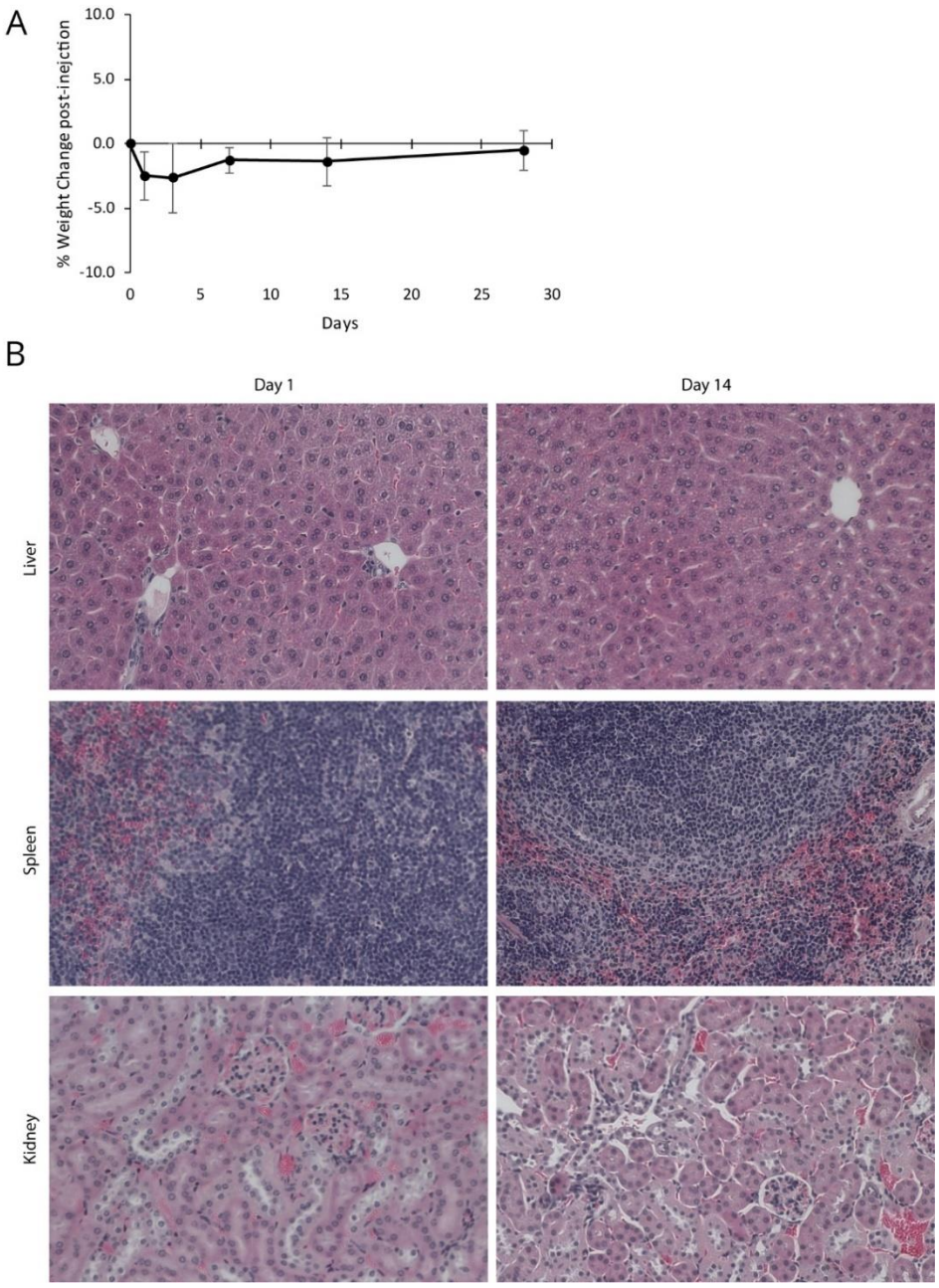

Figure 3.9. ICG-AuNP clusters (30 mg kg^{-1} Au, 4.5 mg kg^{-1} ICG, I.V.) were administered to naïve C57BL/6 mice. (A) Mouse body weights were recorded serially for three mice. Results expressed as ± SEM. (B) Organ samples (liver, spleen, and kidney) were collected from mice at 1 day, 3 days, 7 days, and 14 days post-injection; tissues were fixed in formaldehyde, embedded in paraffin, stained with H&E, and examined for histology. Representative images from days 1 and 14 are shown.

Finally, we assessed the short-term accumulation of clusters in murine orthotopic tumors. For these and subsequent studies, 4T1 mammary tumors were implanted orthotopically in immune-competent mice. When tumors surpassed 50 mm^3, mice were injected with ICG-AuNP clusters (20 mg kg^{-1} ICG, 133 mg kg^{-1} Au, I.V.). Eighteen hours later, we found 1.95 ± 0.4 %ID g^{-1} had accumulated in the tumor. This is consistent with previously reported results for nanoparticle tumor accumulation.[47]

In vivo Imaging of ICG-AuNP Clusters

Having established in vivo tolerability of ICG-AuNP clusters, we next prepared to evaluate their diagnostic and therapeutic potential in a mouse orthotopic breast cancer model. We first sought to visualize tumors by photoacoustic imaging using accumulated ICG-AuNP clusters as a contrast agent. Tumor-bearing mice were imaged both at baseline and 18 hours after receiving either clusters or free ICG (20 mg kg^{-1} ICG, 133 mg kg^{-1} Au, I.V.) (**Figure 3.10**; **Figure 3.11**). Cluster-treated mice demonstrated high signal intensity localized to the tumor; this signal was spectrally distinguishable from background photoacoustic signal contributed by oxygenated and deoxygenated hemoglobin. In contrast, mice who received free ICG showed very little overall signal. These data correlate well with previous reports showing rapid clearance of ICG from the body,[46] and emphasize that nanoformulations of ICG broaden its tissue imaging applications.

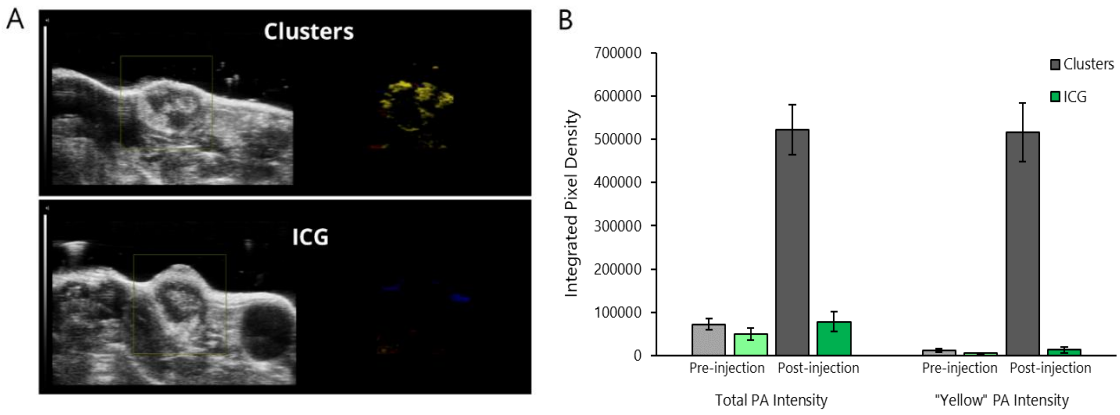

Figure 3.10. Photoacoustic imaging of 4T1 orthotopic mammary tumors in mice receiving either free ICG or ICG-AuNP clusters (20 mg kg^{-1} ICG, 133 mg kg^{-1} Au, I.V.). (A) Representative images of mouse tumors at 18 hours post-injection. Left, ultrasound image; right, spectrally unmixed photoacoustic (color) image of ICG/cluster distribution (yellow) as well as oxygenated (red) and deoxygenated (blue) hemoglobin signal. (B) Quantification of PA signal intensity before injection and 18 hours after injection; left bars show total PA intensity, right bars show intensity associated with spectrally unmixed ICG/cluster signal. *n* = 3 mice per group, ± SEM.

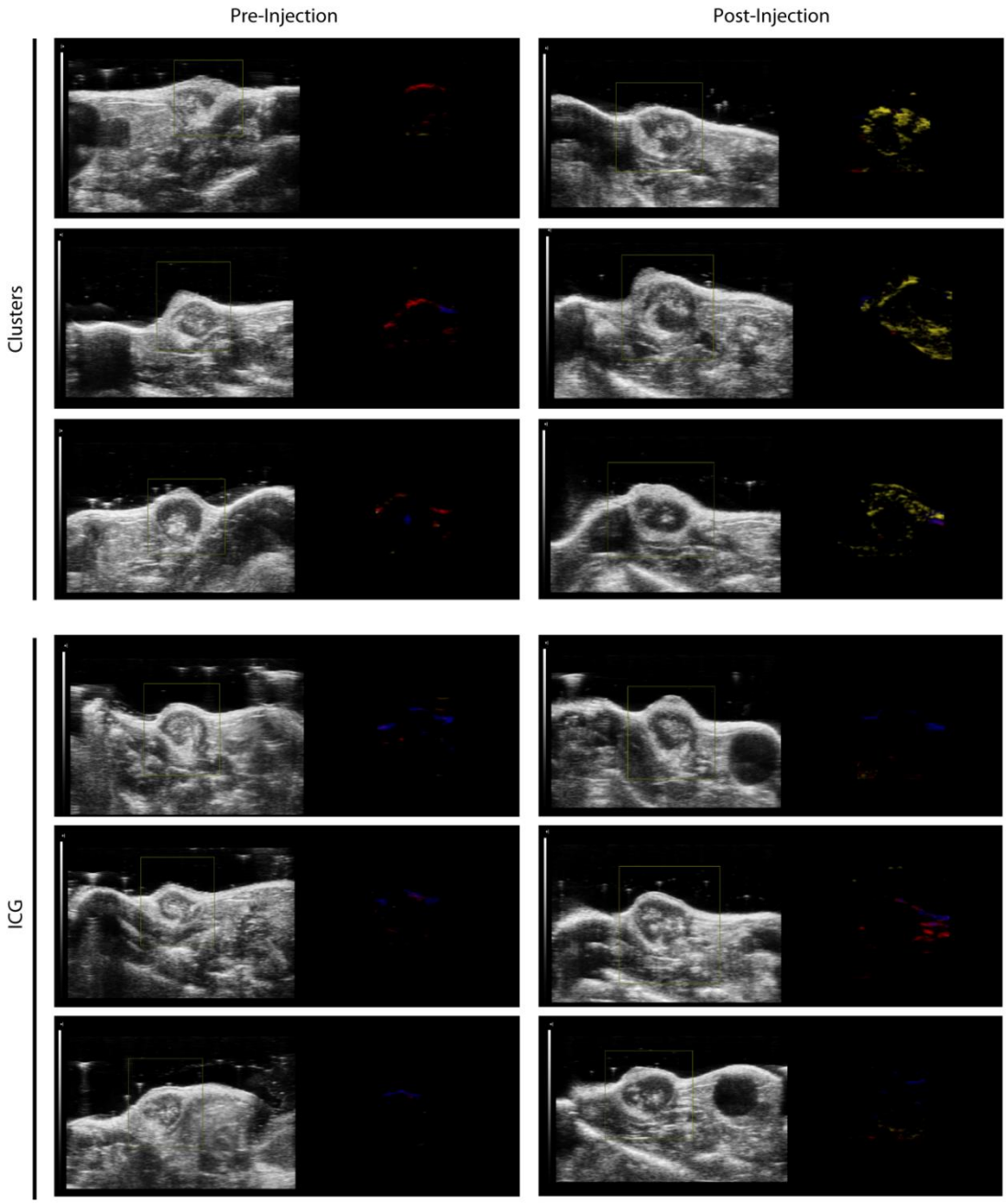

Figure 3.11. Photoacoustic imaging of 4T1 orthotopic mammary tumors in mice receiving either free ICG or ICG-AuNP clusters (20 mg kg^{-1} ICG, 133 mg kg^{-1} Au, I.V.). Images were collected both prior to injection and 18 hours post-injection, with columns matched for individual mice. Within each box, ultrasound images (left; gray) are displayed next to spectrally unmixed photoacoustic images (right; yellow = clusters/ICG, red = oxyhemoglobin, blue = deoxyhemoglobin).

In vivo Heating of ICG-AuNP Clusters

Finally, we evaluated antitumor efficacy in a photothermal therapy model. In these studies, we delivered irradiation subcutaneously using a surgical model. Mice with established 4T1 tumors (50 mm^3) were treated with either saline, free ICG, or ICG-AuNP clusters (20 mg kg^{-1} ICG, I.V.); eighteen hours later, mammary tumors were exposed by skin incision and directly irradiated for 30 minutes (0.7 W cm^{-2}, 1.13 cm^2 laser area). During irradiation, we observed an increase in tumor temperature for all groups (**Figure 3.12A,B**). However, cluster-treated mice demonstrated the most profound heating effect, ultimately rising approximately 13 °C above body temperature (13.4 ± 2.3 °C). In contrast, tumor temperature rose only moderately in saline- and free ICG-treated animals (6.4 ± 0.9 °C and 6.7 ± 0.8 °C, respectively). Indeed, free ICG appeared to improve hyperthermia very modestly at early timepoints – though still less than ICG-AuNP clusters – but the effect was not sustained; this observation coheres well with our in vitro data showing a rapid plateau of heating capacity (**Figure 3.6A,B**).

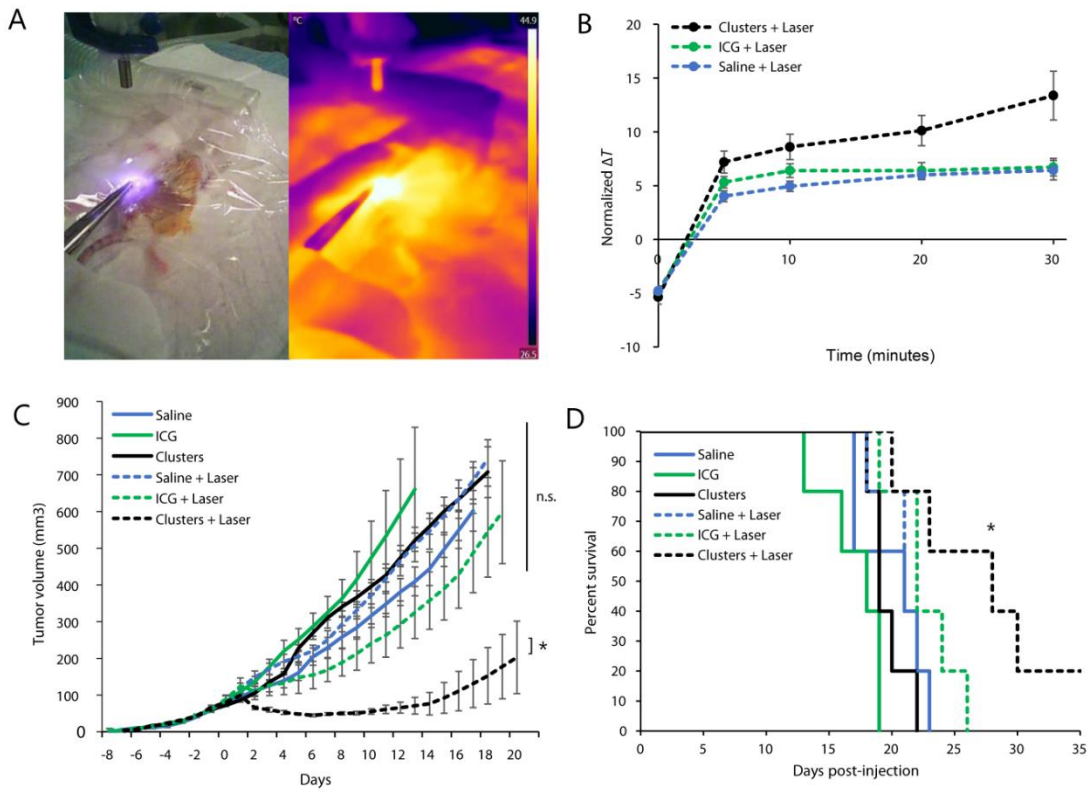

Figure 3.12. Mice bearing 4T1 orthotopic breast tumors were injected with saline, free ICG, or ICG-AuNP clusters (20 mg kg^{-1} ICG, 133 mg kg^{-1} Au, I.V.); eighteen hours later, a subset of mice also received subcutaneous laser irradiation (0.7 W cm^{-2}, 1.13 cm^2 laser area, 30 minutes). *n* = 5 mice per group, for a total of six groups. (A) Representative thermographic image during treatment. (B) Quantification of thermal imaging data over time, expressed as the difference between tumor temperature and animal body temperatures (average temperatures in fixed-size regions of interest). (C) Tumor growth curves, averaged among groups; day -1 = injection, day 0 = laser treatment or no treatment. (D) Kaplan-Meier curve demonstrating animal survival. Data shown ± SEM; * = $p < 0.05$; n.s. = no statistical significance.

Mammalian cell death typically occurs at temperatures > 42-44 °C, though this effect is contingent on duration of heating as well as other factors such as cell type.[48] We observed that cluster-treated tumors surpassed 43 °C within 5 minutes of heating, reaching an ultimate recorded temperature of 52.3 ± 2.3 °C by 30 minutes (**Figure 3.13**). This was a marked improvement over both control groups, which required more than 10

minutes to exceed 42 °C and which attained significantly lower final temperatures (free ICG: 45.6 ± 1.4; saline: 43.6 ± 1.2 °C). It is important to note that tumor hyperthermia was observed using an infrared thermographic camera, which detects surface temperature of tissues but cannot fully characterize the thermal environment within the tumor.

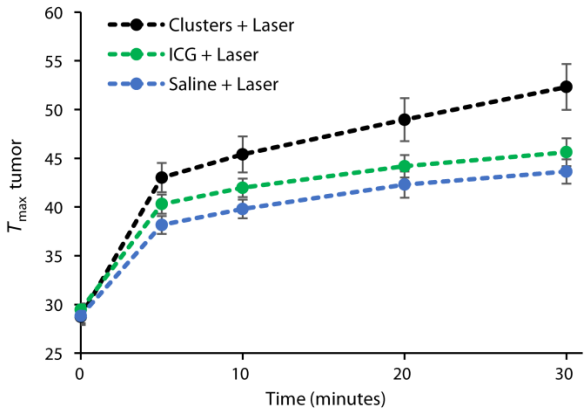

Figure 3.13. Quantification of thermal imaging data from mice bearing 4T1 orthotopic tumors, treated with saline, free ICG, or ICG-AuNP clusters (20 mg kg^{-1} ICG, 133 mg kg^{-1} Au, I.V.), and then treated with subcutaneous laser irradiation (0.7 W cm^{-2}, 1.13 cm^2 laser area, 30 minutes) eighteen hours later. Data show the maximum temperature observed in the tumor for each group. *n* = 5 mice per group, for a total of three groups, ± SEM.

We next tracked long-term tumor growth in these photothermally-treated mice, as well as in control mice receiving drugs or saline alone (**Figure 3.12C**; **Figure 3.14**). We observed statistically significant tumor shrinkage in mice that received the therapeutic combination of ICG-AuNP clusters with laser irradiation. This response was robust: average tumor size regressed below pre-treatment volume within two days of therapy, continued to drop until Day 6, and remained below the initial volume for a total of 11 days. Only one other experimental group displayed regression – those receiving free ICG and laser therapy together – but this decrease was brief (one day) and modest (did

not reach pre-therapy size). ICG-mediated PTT was not significantly more effective than controls at any time. In contrast, PTT with ICG-AuNP clusters showed significant improvement over PTT with ICG ($p < 0.05$, day 6 onward) as well as PTT-alone, clusters-alone, ICG-alone, or no treatment ($p < 0.05$, day 2 onward).

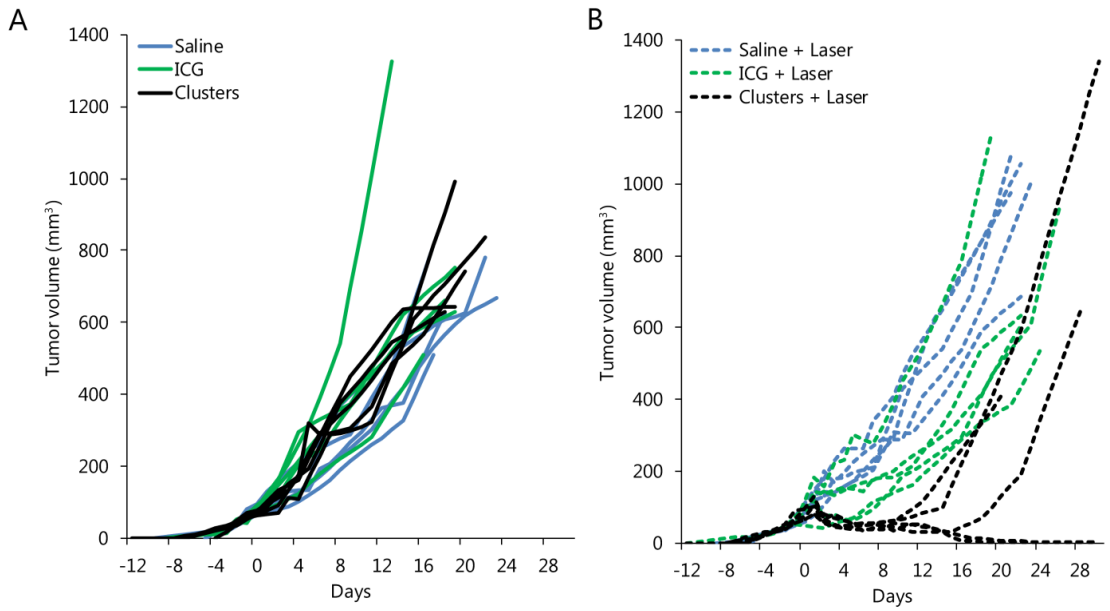

Figure 3.14. Individual tumor growth curves for all 4T1 tumor-bearing mice receiving injections of saline, free ICG, or ICG-AuNP clusters (20 mg kg^{-1} ICG, 133 mg kg^{-1} Au, I.V.). A) Mice receiving drugs alone; day -1 = injection. B) Mice receiving drugs plus laser irradiation (0.7 W cm^{-2}, 1.13 cm^2 laser area, 30 minutes) eighteen hours after injection; day 0 = laser treatment.

When comparing all treatment groups to the control (saline with no PTT), we found a significant improvement in animal survival for mice receiving clusters and laser irradiation ($p = 0.032$); no other group showed statistical significance (**Figure 3.12D**). Notably, two out of five mice that received cluster-mediated PTT displayed complete remission of the primary tumor (**Figure 3.14B**). One of these mice died on Day 22, potentially of a tumor metastasis, which is common for this model[45] and which was

supported by an observation of 15% body weight increase, suggesting ascites; however, the other mouse survived until termination of the study on Day 60, indicating full disease remission.

3.4 Conclusion

We set out to create a nanoformulation incorporating two common and well-characterized materials: indocyanine green, a clinically-approved dye, and gold nanoparticles, which are also utilized in ongoing clinical trials. We found that these two materials formed a stable nanocluster structure – despite the absence of additional binding or solubilization reagents – and demonstrated excellent in vitro and in vivo biological interactions, including low toxicity, effective tumor localization, and good excretion over time. Knowing that both ICG and AuNPs are highly effective in photoacoustic imaging and photothermal therapy, we set out to characterize ICG-AuNP clusters in these modalities. Both in vitro and in vivo data indicated that the nanoparticles are potent and specific imaging reagents, and are highly effective at heat production. We found that mice treated with clusters and laser irradiation – but not those with free ICG and laser – could exhibit severe tumor cytotoxicity in a triple-negative orthotopic breast cancer model; this included 40% complete remission of the primary tumor and 20% complete remission of disease. Altogether, these ICG-AuNP clusters represent a promising new nanomaterial for cancer diagnosis and therapy.

3.5 Experimental Section

Materials: Indocyanine green, gold (III) chloride trihydrate, tetraoctylammonium bromide, 1-dodecanethiol, sodium borohydride, Sepharose® CL-4B, and sodium azide were purchased from Sigma-Aldrich (St. Louis, MO). Poly(ethylene glycol)-*b*-poly(ε-caprolactone) (PEG_{4k}-PCL_{3k}) was purchased from Polymer Source (Quebec, Canada).

Singlet Oxygen Sensor Green Reagent, fetal bovine serum (FBS), Trypsin-EDTA, Dulbecco's Modified Eagle Medium (DMEM), and penicillin-streptomycin solution were purchased from Thermo Fisher Scientific (Gibco; Waltham, MA). MTT assay kit was purchased from Roche Diagnostics GmbH (Mannheim, Germany).

Synthesis of 2-nm hydrophobic gold nanoparticles: Dodecanethiol-coated gold nanoparticles were synthesized according to a protocol modified from Brust et al.,[39] as previously described.[37,38,49] A stock solution of gold (III) chloride trihydrate (1 g mL^{-1}) was centrifuged at 16,000 x *g* for 30 minutes to eliminate seeds, and 306 µL of the purified solution was diluted into 30 mL water to yield a 30 mM solution. In parallel, a 50 mM solution of tetraoctylammonium bromide was prepared by dissolving 2.19 g in 80 mL toluene. These two solutions were combined in an acid-washed flask and stirred vigorously, and 201 µL of 1-dodecanethiol was added. Finally, a 400 mM solution of sodium borohydride was also prepared by dissolving 0.378 g in 25 mL water. This solution was slowly and continuously pipetted into the gold mixture over the course of 15 minutes, and the resultant mixture was allowed to stir for 3 hours. The organic phase was collected and washed as follows: the toluene solution was first diluted in a 6.5-fold excess (v/v) of 95% ethanol, kept at –20 °C overnight, centrifuged to collect the precipitated nanoparticles, and resuspended in a minimal volume of toluene. After a total of two such wash cycles, the nanoparticle solution was transferred into pre-weighed microcentrifuge tubes and the solvent was removed using a centrifugal evaporator (CentriVap, Labconco Corporation, Kansas City, MO).

Synthesis of ICG-AuNP clusters: Dodecanethiol-coated gold nanoparticles were dissolved in toluene at a concentration of 40 mg mL^{-1} (based on dry particle mass).

Meanwhile, a second solution was prepared containing indocyanine green (ICG) dissolved in dimethylformamide (100 mg mL^{-1}); 20 µL of the ICG solution was then diluted into a mixture of dimethylformamide and toluene (30 µL and 60 µL, respectively). The diluted ICG was then combined with the primary gold nanoparticle solution (400 µL for most studies, or 50-500 µL for a subset of studies). The resulting mixture was pipetted into a glass vial containing 4 mL of water, and the sample was sonicated until a homogeneous colloid was observed. To remove organic solvents, the emulsion was allowed to stand overnight to evaporate toluene, then dialyzed in pure water to remove dimethylformamide. For studies requiring the precise determination of bound and unbound ICG, nanoclusters were further purified by passing through a Sepharose® CL-4B column (1.5 x 12 cm), collected as a dark brown band that was visually distinct from green ICG; in all other experiments, including cell and animal functional studies, clusters were not purified by column. Finally, clusters were concentrated using a centrifugal evaporator, then centrifuged at 400 x *g* for 10 minutes to remove large aggregates, and generally stored at a concentration of 3-4 mg mL^{-1} for a period of several weeks.

Synthesis of polymeric-AuNP clusters: As experimental controls, AuNP clusters were encapsulated within a polymeric micelle, according to a protocol modified from Al Zaki et al.[35] Briefly, dodecanethiol-coated gold nanoparticles were dissolved in toluene at a concentration of 17.5 mg mL^{-1} (based on dry particle mass). 200 µL of this solution was combined with 3.5 mg of poly(ethylene glycol)-*b*-poly(ε-caprolactone) (PEG_{4k}-PCL_{3k}) and sonicated thoroughly to combine. The resulting solution was pipetted into a glass vial containing 4 mL of water, and the sample was sonicated until a homogenous colloid was observed. To remove organic solvents, the emulsion was allowed to stand overnight to evaporate toluene. Clusters were centrifuged once at 400 x *g* for 10 minutes to remove

large aggregates, and then the supernatant was centrifuged twice at 3100 x *g* for 30 minutes to sediment desired micelles.

Physiochemical characterization: Nanoparticles (including dodecanethiol-coated gold nanoparticles, ICG-AuNP clusters, and polymeric-AuNP clusters) were characterized by a variety of physiochemical techniques. Gold particles were visualized using transition electron microscopy (Tecnai T12, FEI, Hillsboro, OR) to determine core diameter. Hydrodynamic diameter and zeta potential of clusters were also examined using dynamic and electrophoretic light scattering, respectively (Zetasizer Nano ZS, Malvern Panalytical, Malvern, United Kingdom); all DLS data was expressed by particle number. ICG-AuNP clusters, free ICG, and dodecanethiol-coated AuNPs were also dissolved in water, dimethylformamide, fetal bovine serum, and/or toluene to capture their absorbance spectra (Varian-Cary 100 Bio spectrophotometer, Agilent Technologies, Santa Clara, CA) and fluorescence spectra (FluoroMax-3 spectrofluorimeter, Horiba Jobin Yvon, Edison, NJ).

To determine the composition of ICG-AuNP clusters, each constituent was examined as follows. ICG concentration was determined by dissolving clusters in dimethylformamide (> 95% v/v) and comparing absorbance at λ = 792 nm with a standard curve for ICG. Gold concentration was determined using inductively-coupled plasma optical emission spectroscopy (ICP-OES; Spectro Genesis, Spectro Analytical Instruments, Kieve, Germany). Briefly, aqueous solutions of clusters (20-200 µL) were placed in round-bottomed glass tubes with polytetrafluoroethylene-coated caps. To this was added up to 300 µL of aqua regia (e.g., 75 µL nitric acid plus 225 µL hydrochloric acid), and tubes were capped and allowed to stand at room temperature for several hours. Finally, solutions were diluted up to a standard volume and then

spectrometrically analyzed. ICG and Au concentrations in purified clusters were then analyzed using the following equations:

$$\text{Encapsulation efficiency} = \frac{\text{(ICG mass} \div \text{Au mass) after column purification}}{\text{(ICG mass} \div \text{Au mass) before column purification}} \times 100 \quad (1)$$

$$\text{ICG loading} = \frac{\text{ICG concentration after column purification}}{\text{Au concentration after column purification}} \times 100 \quad (2)$$

In vitro imaging: Varying concentrations of ICG-AuNP clusters, ICG, and/or polymer-AuNP clusters were dissolved in water and then imaged using a phantom. In one study, solutions (50 µl each) were added to a 384-well plate and then examined by fluorescence imaging (IVIS Spectrum In Vivo System, Perkin Elmer, Waltham, MA). IVIS parameters: excitation, 745 nm; emission, 820 nm; lamp level, high; exposure time, 0.5 seconds; binning, (M)8*; f*, *2.*

In a separate study, solutions were placed into polyethylene tubing (0.5-mm diameter) submerged in water at a depth of 1-2 cm, and were examined by photoacoustic imaging (Vevo Lazr, VisualSonics, Toronto, Canada). The LZ250 transducer was utilized (axial resolution, 75 µm; broadband frequency, 13-24 MHz). Images were acquired with the following settings: PA gain 30-40 dB, priority 95%, and distance 12 mm from the transducer. ICG-AuNP clusters and free ICG were examined within a single imaging session at 30 dB, allowing direct comparison of signal intensities.

In vitro heating: Solutions of ICG-AuNP clusters, along with various controls, were treated with laser irradiation to induce heating. One milliliter of prepared solution was added to a 2-mL microcentrifuge tube, and a fiber optic thermometer (Nomad, Qualitrol-

Neoptix, Fairport, NY) was inserted 4 mm below the liquid surface. Solutions were then irradiated with an 808-nm laser (OEM Laser Systems, Midvale, UT) at 1.2 W power (0.1 cm^2 area). Irradiation continued for a period of 10 minutes, during which temperature was recorded every 10 seconds. In a subset of experiments, solutions were first irradiated for 10 minutes as described, then freely allowed to cool to their original pre-irradiation temperature; immediately after reaching this threshold, irradiation was repeated for two additional 10-minute cycles with cooling between. All experiments were performed at room temperature and with ambient light.

In vitro ROS generation: ICG-AuNP clusters and various controls were examined for their ability to generate reactive oxygen species, using the reporter reagent Singlet Oxygen Sensor Green. SOSG-containing solutions (2.5 mL, 10 µM SOSG) were added to a quartz cuvette and mixed continuously by magnetic stirrer for 30 minutes. Aliquots (60 µL) were withdrawn at each of the following timepoints: 0, 1, 5, 10, 20, and 30 minutes. Samples were then diluted 20-fold in water, and fluorescence was read by fluorimeter (ex = 488 nm; em = 523 nm) and normalized to the 0-minute reading. Solutions of ICG-AuNP clusters and free ICG (0.015 mg mL^{-1}) were tested with or without sodium azide (10 mM). Samples were either kept in the dark or were irradiated continuously for 30 minutes (808 nm; 1.2 W power, 0.1 cm^2 area). Irradiated samples of clusters and ICG also had surface temperature monitored using a FLIR ONE thermal imaging camera (FLIR Systems, Wilsonville, OR); based on this data, a subset of samples were heated with equivalent temperature and timing under dark conditions (heat generated by Varian-Cary 100 Bio spectrophotometer, thermal accessory). Sample conditions generating greater than 1.5-fold change in SOSG fluorescence were performed in triplicate; all others were performed as single assays.

Cell culture: Mouse 4T1 breast cancer cells (ATCC, Rockville, MD) were cultured in DMEM supplemented with 10% heat-inactivated FBS and 1% penicillin-streptomycin (100 U mL^{-1} penicillin, 100 µg mL^{-1} streptomycin). Cultures were maintained at 37°C in a humidified incubator with 5% CO_2.

Cell viability by MTT assay: To determine cytotoxicity of ICG-AuNP clusters, 4T1 mouse breast cancer cells were seeded in 96-well plates (white with clear, flat bottom) at a density of approximately 1.0 x 10^4 per well. Cells were allowed to incubate overnight, and then media was carefully removed from individual wells and replaced with fresh media containing nanoclusters or free ICG at various concentrations (*n* = 3 wells per condition). Plates were then incubated for 24 hours. Finally, media was removed and cells were washed with phosphate buffered saline, then given fresh media and subjected to a standard MTT assay. Results were expressed as % Cell Viability by comparing to the average absorbance value (λ = 590) of cells treated with media alone (*n* = 3 wells per plate used).

Nanocluster cytotoxicity was also examined in combination with laser irradiation. In these experiments, to ensure isolation of environmental conditions, cells were plated with two empty wells between them. The following day, plates were removed from incubators and placed on a 37°C warming surface to maintain temperature. Media was exchanged for fresh 37°C media containing nanoclusters or free ICG at various concentrations (*n* = 3 wells per condition). Immediately after addition, wells were irradiated with an 808-nm laser (0.2 W cm^{-2}; 1.13 cm^2 area) for a total of 7 minutes (84 J cm^{-2}). Plates were returned to the incubator for 24 hours, after which they were washed and analyzed by MTT as described. Results were expressed as % Cell Viability by

comparing to the average absorbance value (λ = 590) of cells treated with standard media under dark conditions (*n* = 3 wells per plate used).

Animal and tumor models: Female mice (C57BL/6 or BALB/c), aged approximately 6-10 weeks, were obtained from Charles River Laboratories (Wilmington, MA). All animal studies were conducted with approval by the University of Pennsylvania Institutional Animal Care and Use Committee, in accordance with AAALAC guidelines and accreditation. Mice were fed standard chow *ad libitum* unless otherwise noted.

In a subset of studies, BALB/c mice were inoculated with 4T1 mouse breast cancer cells (2×10^6 cells per mouse, 50-80 µL total volume) injected orthotopically into the fourth abdominal mammary pad. At the time of tumor inoculation, abdominal hair was removed by application of depilatory cream; all tumor-bearing mice were also switched to a low-fluorescence diet (Teklad global 18% rodent diet 2918, Envigo, Madison, WI) to avoid interference with subsequent imaging studies. Tumor size was established by first measuring two axes (length and width) with digital calipers, and then estimating tumor volume using the following equation:

$$\text{Tumor volume} = \frac{\text{Length} \times \text{Width}^2}{2} \quad (3)$$

Biodistribution and toxicity in tissues: C57BL/6 mice were injected I.V. (retro-orbitally) with clusters at a dose of 30 mg Au (approximately 4.5 mg ICG) per kg body weight (*n* = 15 mice total). Blood samples (3-20 µL each) were collected from the tail vein at the following timepoints post-injection: 5 minutes, 15 minutes, 30 minutes, 1 hour, 2 hours, 6 hours, 12 hours, and 24 hours. These samples were collected from a total of three mice

per timepoint, such that all mice received either one or two blood collections, and all groups were randomized with regards to subsequent study arm assignment. Blood samples were pipetted directly into round-bottomed glass tubes and stored at room temperature. Finally, samples were processed and analyzed for gold content using ICP-OES as previously described, using up to 1000 µL of aqua regia (e.g., 250 µL nitric acid plus 750 µL hydrochloric acid). For normalization purposes, blood samples were considered to be 1 µL = 1 mg. Half-life was determined by fitting a double exponential decay curve to the data using MATLAB software (Mathworks, Natick, MA).

These same mice were sacrificed at the following timepoints post-injection (n = 3 per group): 1 day, 3 days, 7 days, 14 days, and 28 days. Urine and feces samples were also collected at these timepoints from lightly-restrained mice, and were pooled from multiple mice within each group. At sacrifice, mice were first anesthetized with isoflurane (3%, 2 L min^{-1} O_2; isoflurane precision vaporizer, VetEquip, Pleasanton, CA), exsanguinated via cardiac puncture, then euthanized by cervical dislocation. The following organs were then extracted (intact whole organs, unless otherwise noted): brain, heart, kidneys, liver (approximately 290 mg of right medial lobe), lung, muscle (gastrocnemius), skin (approximately 80 mg from femoral region with hair removed), spleen. Tissues were rinsed in phosphate-buffered saline after extraction, frozen until ready for analysis, and then examined for gold content using ICP-OES. Briefly, collected tissues were weighed and then transferred into round-bottomed glass tubes with polytetrafluoroethylene-coated caps. To this was added up to 1000 µL of aqua regia (e.g., 250 µL nitric acid plus 750 µL hydrochloric acid). Tubes were lightly capped and allowed to stand at room temperature overnight. Solutions were diluted up to a standard volume, then passed through 0.2 µm filters to remove any indigestible material. Finally,

samples were spectrometrically analyzed. For normalization purposes, urine samples were considered to be 1 µL = 1 mg.

To monitor animal toxicity, three of these mice (those ultimately sacrificed at 28 days) had their body weights periodically recorded. Also, for mice sacrificed between 1 day and 2 weeks, small samples of harvested tissue were analyzed for histology. The following organ samples were collected: kidney (*n* = 3 per timepoint), liver (*n* = 3 per timepoint), and spleen (*n* = 2 per timepoint). Tissue was fixed in formalin for 24-48 hours. Samples were then embedded in paraffin, sectioned, and stained with H&E by the Penn Center for Musculoskeletal Disorders Histology Core (P30-AR069619). Slides were imaged using an EVOS FL Auto Imaging System (Life Technologies) at 20x objective, and tissue was examined for markers of pathology including infiltrating immune cells, abnormal and multiple nuclei, apoptotic or necrotic events, and disruption of tissue architecture.

In a separate study, BALB/c mice were implanted with orthotopic mammary tumors as described (*n* = 5 mice). When tumor size surpassed 50 cm^3, mice were injected I.V. (via tail vein) with clusters at a dose of 20 mg ICG (approximately 133 mg Au) per kg body weight. Eighteen hours after injection, tumor size was recorded again and mice were sacrificed as described. Tumors were extracted intact, frozen until further analysis, and finally examined for gold content using ICO-OES.

In vivo imaging: BALB/c mice were implanted with orthotopic mammary tumors as described. When tumor size surpassed 50 cm^3, mice were anesthetized with isoflurane (1.8 - 3%, 2 L min^{-1} O_2) and imaged by photoacoustic imaging as described. On the same day, mice were injected I.V. (via tail vein) with clusters at a dose of 20 mg ICG (approximately 133 mg Au) per kg body weight; control mice were injected with an

equivalent dose of free ICG (*n* = 3 mice per group, two groups). Eighteen hours after injection, mice were imaged by photoacoustic imaging as described. Spectral unmixing techniques were used to separate the contrast agent signals from background signals (i.e., oxyhemoglobin and deoxyhemoglobin) based on their PA spectra.

In vivo heating: BALB/c mice were implanted with orthotopic mammary tumors as described. When tumor size surpassed 50 cm^3, mice were injected I.V. (via tail vein) with ICG-AuNP clusters at a dose of 20 mg ICG (approximately 133 mg Au) per kg body weight. Control mice were injected with an equivalent dose of free ICG or with 0.9% saline (*n* = 5 mice per group, three groups).

Eighteen hours after injection, mice were subjected to subcutaneous photothermal therapy. Briefly, mice were given preoperative analgesia (0.1 mg kg^{-1} buprenorphine, S.Q.) and anesthetized with isoflurane (1.8 - 3%, 2 L min^{-1} O_2); body temperature was maintained thereafter using a recirculating water pad (Kent Scientific, Torrington, CT). The abdominal skin was sterilized (povidone-iodine and 70% ethanol) and a sterile drape was placed. Next, a curved incision was made medial to the tumor, and hemostat clamps were used to draw back the skin and expose the underside of the tumor. Tumors were irradiated at 808 nm for 30 minutes (0.7 W cm^{-2}; 1.13 cm^2 laser area, which fully covered all tumors; 1260 J cm^{-2}). After the completion of illumination, skin was sutured with nylon and mice were hydrated with subcutaneous saline. For the subsequent 72 hours, mice were monitored at least daily for wound condition and signs of distress, and were given additional buprenorphine (0.1 mg kg^{-1}) for the first 24 hours and as needed.

Immediately before and during the described laser therapy, tumor and abdomen surface temperature were monitored using a FLIR ONE thermal imaging camera (FLIR

Systems, Wilsonville, OR) at the following timepoints: pre-treatment, 5 min, 10 min, 20 min, and 30 min. Infrared images were later analyzed for 1) maximum temperature in the tumor, and 2) temperature averaged over each of two 1.3 cm^2 circular regions of interest, one centered on the tumor and one on an area of the shaved abdomen at least 8 mm away (thus approximating overall animal body temperature).

In addition to three groups of laser-treated mice, an additional three groups of mice (n = 5 mice per group) with size-matched tumors were injected with equivalent doses of either ICG-AuNP clusters, free ICG, or saline. These mice received no additional therapeutic interventions.

Tumor volume was monitored in all six groups and calculated as described, beginning a minimum of five days after tumor cell implantation and continuing until animal death. Criteria for animal sacrifice included any of the following: tumor length surpassed 15 mm; ulceration of the skin surpassed 7.5 mm; or animal gait was considerably impacted. Animals were also monitored for weight change and body conditioning score, changes in eating and elimination patterns, as well as other markers of health and behavior.

Statistical analysis: Tumor growth curves were analyzed by type II ANOVA and pairwise comparisons of tumor growth slopes, calculated using TumGrowth open-access software (https://github.com/kroemerlab),[50] as well as by t-test of daily tumor volume means, calculated using Microsoft Excel (Microsoft Co, Redmont, WA, USA). For survival analysis, log-rank test was performed using MedCalc Software (Medcalc, Mariakerke, Belgium),[51] comparing all groups to saline.

3.6 References

[1] R. Baskar, K. A. Lee, R. Yeo, K.-W. Yeoh, *Int J Med Sci* **2012**, *9*, 193–199.

[2] H. H. W. Chen, M. T. Kuo, *Oncotarget* **2017**, *8*, 62742–62758.

[3] H. Wang, X. Mu, H. He, X.-D. Zhang, *Trends in Pharmacological Sciences* **2018**, *39*, 24–48.

[4] S. P. Power, F. Moloney, M. Twomey, K. James, O. J. O'Connor, M. M. Maher, *World J Radiol* **2016**, *8*, 902–915.

[5] A. M. Pekkanen, M. R. DeWitt, M. N. Rylander, *J Biomed Nanotechnol* **2014**, *10*, 1677–1712.

[6] K. Deng, C. Li, S. Huang, B. Xing, D. Jin, Q. Zeng, Z. Hou, J. Lin, *Small* **2017**, *13*, 1702299.

[7] M. Vats, S. K. Mishra, M. S. Baghini, D. S. Chauhan, R. Srivastava, A. De, *Int J Mol Sci* **2017**, *18*, DOI 10.3390/ijms18050924.

[8] H. Chen, Y. Zhao, *ACS Appl. Mater. Interfaces* **2018**, *10*, 21021–21034.

[9] Y. Liu, P. Bhattarai, Z. Dai, X. Chen, *Chemical Society Reviews* **2019**, *48*, 2053–2108.

[10] J. Song, J. Qu, M. T. Swihart, P. N. Prasad, *Nanomedicine: Nanotechnology, Biology and Medicine* **2016**, *12*, 771–788.

[11] X. Ge, Q. Fu, L. Bai, B. Chen, R. Wang, S. Gao, J. Song, *New J. Chem.* **2019**, *43*, 8835–8851.

[12] J. L. Su, B. Wang, K. E. Wilson, C. L. Bayer, Y.-S. Chen, S. Kim, K. A. Homan, S. Y. Emelianov, *Expert Opin Med Diagn* **2010**, *4*, 497–510.

[13] W. Li, X. Chen, *Nanomedicine (Lond)* **2015**, *10*, 299–320.

[14] C. Moore, J. V. Jokerst, *Theranostics* **2019**, *9*, 1550–1571.

[15] M. Erfanzadeh, Q. Zhu, *Photoacoustics* **2019**, *14*, 1–11.

[16] Q. Fu, R. Zhu, J. Song, H. Yang, X. Chen, *Advanced Materials* **2019**, *31*, 1805875.

[17] J. Dang, H. He, D. Chen, L. Yin, *Biomater. Sci.* **2017**, *5*, 1500–1511.

[18] S.-E. Jin, H.-E. Jin, S.-S. Hong, *Biomed Res Int* **2014**, *2014*, DOI 10.1155/2014/814208.

[19] Z. Sheng, D. Hu, M. Xue, M. He, P. Gong, L. Cai, *Nano-Micro Lett.* **2013**, *5*, 145–150.

[20] T. Nagaya, Y. A. Nakamura, P. L. Choyke, H. Kobayashi, *Front Oncol* **2017**, *7*, DOI 10.3389/fonc.2017.00314.

[21] J. P. Thawani, A. Amirshaghaghi, L. Yan, J. M. Stein, J. Liu, A. Tsourkas, *Small* **2017**, *13*, 1701300.

[22] L. Yan, A. Amirshaghaghi, D. Huang, J. Miller, J. M. Stein, T. M. Busch, Z. Cheng, A. Tsourkas, *Adv Funct Mater* **2018**, *28*, DOI 10.1002/adfm.201707030.

[23] A. Amirshaghaghi, L. Yan, J. Miller, Y. Daniel, J. M. Stein, T. M. Busch, Z. Cheng, A. Tsourkas, *Sci Rep* **2019**, *9*, 2613.

[24] X. Huang, M. A. El-Sayed, *Journal of Advanced Research* **2010**, *1*, 13–28.

[25] D. R. Cooper, D. Bekah, J. L. Nadeau, *Front. Chem.* **2014**, *2*.

[26] H. Cui, D. Hu, J. Zhang, G. Gao, Z. Chen, W. Li, P. Gong, Z. Sheng, L. Cai, *ACS Appl. Mater. Interfaces* **2017**, *9*, 25114–25127.

[27] A. Topete, M. Alatorre-Meda, P. Iglesias, E. M. Villar-Alvarez, S. Barbosa, J. A. Costoya, P. Taboada, V. Mosquera, *ACS Nano* **2014**, *8*, 2725–2738.

[28] T. Luo, X. Qian, Z. Lu, Y. Shi, Z. Yao, X. Chai, Q. Ren, *J Biomed Nanotechnol* **2015**, *11*, 600–612.

[29] C. Zeng, W. Shang, X. Liang, X. Liang, Q. Chen, C. Chi, Y. Du, C. Fang, J. Tian, *ACS Appl. Mater. Interfaces* **2016**, *8*, 29232–29241.

[30] S. Fang, C. Li, J. Lin, H. Zhu, D. Cui, Y. Xu, Z. Li, *Journal of Nanomaterials* **2016**, *2016*, Article ID 182746, 10 pages.

[31] W. Song, Y. Li, Y. Wang, D. Wang, D. He, W. Chen, W. Yin, W. Yang, *Journal of Biomedical Nanotechnology* **2017**, *13*, 1115–1123.

[32] W. S. Kuo, Y. T. Chang, K. C. Cho, K. C. Chiu, C. H. Lien, C. S. Yeh, S. J. Chen, *Biomaterials* **2012**, *33*, 3270–3278.

[33] B. Du, X. Gu, W. Zhao, Z. Liu, D. Li, E. Wang, J. Wang, *J. Mater. Chem. B* **2016**, *4*, 5842–5849.

[34] R. Chen, X. Wang, X. Yao, X. Zheng, J. Wang, X. Jiang, *Biomaterials* **2013**, *34*, 8314–8322.

[35] E. Sadauskas, G. Danscher, M. Stoltenberg, U. Vogel, A. Larsen, H. Wallin, *Nanomedicine* **2009**, *5*, 162–169.

[36] L. Wang, Y.-F. Li, L. Zhou, Y. Liu, L. Meng, K. Zhang, X. Wu, L. Zhang, B. Li, C. Chen, *Anal Bioanal Chem* **2010**, *396*, 1105–1114.

[37] A. Al Zaki, D. Joh, Z. Cheng, A. L. B. De Barros, G. Kao, J. Dorsey, A. Tsourkas, *ACS Nano* **2014**, *8*, 104–112.

[38] A. A. Zaki, J. Z. Hui, E. Higbee, A. Tsourkas, *J Biomed Nanotechnol* **2015**, *11*, 1836–1846.

[39] M. Brust, M. Walker, D. Bethell, D. J. Schiffrin, R. Whyman, *Journal of the Chemical Society, Chemical Communications* **1994**, *0*, 801–802.

[40] V. Amendola, R. Pilot, M. Frasconi, O. M. Maragò, M. A. Iatì, *J. Phys.: Condens. Matter* **2017**, *29*, 203002.

[41] B. Dubertret, M. Calame, A. J. Libchaber, *Nature Biotechnology* **2001**, *19*, 365.

[42] E. Dulkeith, M. Ringler, T. A. Klar, J. Feldmann, A. Muñoz Javier, W. J. Parak, *Nano Lett.* **2005**, *5*, 585–589.

[43] K. D. Chaudhuri, *Z. Physik* **1959**, *154*, 34–42.

[44] J. R. Lakowicz, Ed. , in *Principles of Fluorescence Spectroscopy*, Springer US, Boston, MA, **2006**, pp. 331–351.

[45] M. K. Park, C. H. Lee, H. Lee, *Lab Anim Res* **2018**, *34*, 160–165.

[46] W. Song, Z. Tang, D. Zhang, N. Burton, W. Driessen, X. Chen, *RSC Adv.* **2014**, *5*, 3807–3813.

[47] S. Wilhelm, A. J. Tavares, Q. Dai, S. Ohta, J. Audet, H. F. Dvorak, W. C. W. Chan, *Nature Reviews Materials* **2016**, *1*, 16014.

[48] A. Laszlo, *Cell Prolif* **1992**, *25*, 59–87.

[49] C. McQuade, A. A. Zaki, Y. Desai, M. Vido, T. Sakhuja, Z. Cheng, R. J. Hickey, D. Joh, S.-J. Park, G. Kao, et al., *Small* **2015**, *11*, 834–843.

[50] D. P. Enot, E. Vacchelli, N. Jacquelot, L. Zitvogel, G. Kroemer, *OncoImmunology* **2018**, *7*, e1462431.

[51] F. Schoonjans, A. Zalata, C. E. Depuydt, F. H. Comhaire, *Computer Methods and Programs in Biomedicine* **1995**, *48*, 257–262.

CHAPTER 4: SUMMARY DISCUSSION, FUTURE DIRECTIONS, AND CONCLUDING REMARKS

4.1 Summary Discussion and Future Directions

Biodegradability of clustered gold particles

Gold is a highly popular material in preclinical research, possessing a long history and a well-explored range of formulations and applications; however, this breadth of study has not translated to clinical adoption of gold particles. While many potential explanations exist (e.g., expense of material, concerns of toxicity), it is likely that biodegradation – or the lack thereof – plays a major role. Still, many reports do not include an exploration of their material's long-term clearance capacity. In this thesis, we have considered gold biodistribution to be an indispensable aspect of particle characterization and design. We have formulated our gold nanomaterials using ultrasmall gold particles, which have demonstrated capacity for breakdown within the body and excretion through hepatobiliary and/or renal routes. Specifically, this work has built on our group's previous reported formulations. In these studies, small individual nanoparticles are clustered together within a larger micellar construct. This has the advantages of conferring long circulation (optimizing size, presenting an outer hydrophilic PEG surface), as well as packing multifunctional materials together (gold with iron oxide, iron oxide with dyes), while retaining a facile synthetic process with high volumes of functional cargo (encapsulation of hydrophobic materials within micelles).

This methodology therefore installs many favorable features of nanoparticles while still working towards the goal of biodegradability.

In our previous nanoformulations using 2-nm gold particles and PEG-*b*-PCL, gold showed far better breakdown than would be expected for large solid gold cores. We then improved upon this by decreasing the size of gold particles to 0.9 nm. However, we still observed a fraction of gold that persisted within tissues long-term. Notably, within several tissues – particularly the liver – we detected that particles cleared steadily during early timepoints, but reached a plateau later on. This is an important observation because it demonstrates the overall utility of long-term biodistribution studies to fully capture important interactions, and it also highlights a specific deficiency in our particles' clearance abilities. Based on this observation, we embarked on the current study using environmentally sensitive materials, which we believed would further improve gold elimination. We also chose to pursue the study out to the three-month timepoint, and once again, we noticed distinct long-term changes in degradation. Namely, in a compartment that had not experienced any early decrease in gold (i.e., the spleen), levels began to fall between one and three months after injection. This clearly demonstrates the complexity of nano-bio interactions and the necessity of gathering this extended data when time and materials allow.

During our study, we found that clearance of gold was quite high (86% in liver, 72% in spleen). In order to improve even further, several strategies could be employed. Although rates of cellular internalization were not examined in detail, it is plausible that slow cell uptake contributed to the long-term biopersistence of gold and its "escape" from our pH-mediate clearance mechanism. Therefore, future studies with this particle could include formulation changes that help target it into cellular lysosomes. Opsonization is

known to increase uptake by phagocytic cells (though it is also likely to shorten blood circulation times), so perhaps the use of a less-stealthy material than poly(ethylene glycol) would produce improvements. Alternatively, because liver clearance was overall faster and more extensive than spleen clearance, efforts could be made to shift this biodistribution balance through changes like tuning particle surface chemistry as well as size. Such manipulations could likely be performed easily due to the modular nature of our polymer micelles; different amphiphilic coatings could be tested without changing the AcetalDextran-AuNPs, which already appear to have highly efficient breakdown capabilities.

Importantly, in our analysis of these particles, we did not examine any therapeutic or imaging functions, nor did we look at biodistribution of particles into solid tumors. We consider such an analysis to be highly important and do not necessarily assume that these particles will be as functional as previous formulations, especially considering their less-efficient loading of gold cargos. However, we are hopeful that this material – or other materials inspired by these techniques – could show good therapeutic potential.

Functional applications of clustered gold particles

One of the hallmarks and great advantages of nanomedicine is the ability to combine multiple functional moieties within the same particle. This has been demonstrated in countless published works describing nanoparticle formulations with nearly every imaginable combination of diagnostic and treatment modalities. Such constructs have many benefits, including precise control over relative dosages at target locations and the ability to address complementary clinical goals without repeat intervention. The classic example of this paradigm is a nanoparticle that can traffic into

solid tumors and enable A) imaging of tumor location and morphology, and B) destruction of cancer cells. With this pairing, tumor ablation (through surgery, radiotherapy, etc.) can be pursued more precisely and safely; furthermore, treatment effectiveness can often be predicted and confirmed.

In this work, we have reported a nanoformulation that combined two highly common materials – gold particles and indocyanine green – and explored their efficacy for photoacoustic imaging and photothermal/photodynamic therapy. Our studies did not directly integrate these interventions, largely due to a lack of instrumentation capable of employing photoacoustic imaging data for guidance of optical irradiation. Such technology could plausibly emerge in the future as each technique is studied further and adopted into mainstream clinical practice.

The present work joins a cohort of our group's reported structures (cited throughout) that interchange various functional materials, demonstrating the strong modularity of our nanoparticle cluster formulations. Thus far, cores have been assembled from gold nanoparticles, iron oxide nanoparticles, and iron oxide doped with elements like zinc and manganese; metal particles have been surface-coated with alkanes, sugars, and lipids, and their sizes have ranged from 0.9 to nearly 15 nanometers; and different particles have been encapsulated within the same structure. Additionally, the outer coating has been formed from a variety of amphiphilic molecules, including long block polymers (> 7000 Da) and small molecules (< 600 Da). Imaging applications have included photoacoustic, CT, MR, and fluorescence/optical; therapeutic applications have included photothermal, photodynamic, radiosensitization, and drug delivery. In summary, varying materials can be combined into stable structures that often require little revision of experimental protocols, giving easy access to a broad

range of specific functional applications. Furthermore, due to the relative simplicity of materials and syntheses, these particles may have advantages in clinical development processes including lead-finding and larger-scale manufacturing. Further research by our group will continue to explore a range of materials and applications compatible with these structures, and well as their translatability to the clinic.

4.2 Concluding Remarks

Gold nanoformulations have enormous potential to fulfill unmet clinical needs in oncology. Several ongoing clinical studies have shown great promise for gold's biocompatibility and efficacy in applications such as imaging, drug delivery, and radiosensitization. However, continued research is required to answer fundamental questions about gold nanoparticles' pharmacokinetics, long-term safety, and efficacy for emerging treatment technologies. We are hopeful that this work, and subsequent studies building upon it, will help diversify and improve therapies available to patients.